HYDRODYNAMICS OF PITCHING FOILS: FLEXIBILITY AND GROUND EFFECTS

Rafael Fernandez Prats

Dipòsit Legal: T 979-2015

HYDRODYNAMICS OF PITCHING FOILS: FLEXIBILITY AND GROUND EFFECTS

Rafael Fernández Prats
PhD thesis

UNIVERSITAT ROVIRA I VIRGILI

Thesis supervisor: Prof. Francisco J. Huera Huarte
Department of Mechanical Engineering
Universidad Rovira i Virgili

April 2015

UNIVERSITAT ROVIRA I VIRGILI
HYDRODYNAMICS OF PITCHING FOILS: FLEXIBILITY AND GROUND EFFECTS
Rafael Fernandez Prats
Dipòsit Legal: T 979-2015

Rafael Fernández Prats

HYDRODYNAMICS OF PITCHING FOILS: FLEXIBILITY AND GROUND EFFECTS

UNIVERSITAT ROVIRA I VIRGILI
HYDRODYNAMICS OF PITCHING FOILS: FLEXIBILITY AND GROUND EFFECTS
Rafael Fernandez Prats
Dipòsit Legal: T 979-2015

Department of Mechanical Engineering
Campus Sescelades
Avinguda dels Països Catalans,
26 - 43007 Tarragona, Spain
Tel (34) 977 55 96 02
secmec@urv.cat

I STATE that the present study, entitled "HYDRODYNAMICS OF PITCHING FOILS: FLEXIBILITY AND GROUND EFFECTS", presented by Rafael Fernández Prats for the award of the degree of Doctor of Philosophy, has been carried out under my supervision at the Department of Mechanical Engineering of this university, and that it fulfils all the requirements to be eligible for the International Doctorate Award.

SUPERVISOR:
Prof. Francisco J. Huera Huarte

Tarragona, April 2015

UNIVERSITAT ROVIRA I VIRGILI
HYDRODYNAMICS OF PITCHING FOILS: FLEXIBILITY AND GROUND EFFECTS
Rafael Fernandez Prats
Dipòsit Legal: T 979-2015

UNIVERSITAT ROVIRA I VIRGILI
HYDRODYNAMICS OF PITCHING FOILS: FLEXIBILITY AND GROUND EFFECTS
Rafael Fernandez Prats
Dipòsit Legal: T 979-2015

Dedicado a mis padres y hermanos, Manuela y Domingo.

UNIVERSITAT ROVIRA I VIRGILI
HYDRODYNAMICS OF PITCHING FOILS: FLEXIBILITY AND GROUND EFFECTS
Rafael Fernandez Prats
Dipòsit Legal: T 979-2015

ABSTRACT

The roles of the chordwise flexural stiffness and ground effect in a rectangular plate undergoing in pure pitching have been investigated in this thesis. Digital Particle Image Velocimetry (DPIV), load measurements with a 6-axes balance, measurements of the swimming speed and image acquisition of the kinematics of the foil have been done to study the flow patterns and hydrodynamics forces around the flapping rigid and flexible plates. The presence of the wall enhances the cruising velocity in some cases up to 25% and the thrust by a 45% , for swept angles of 160 and 240 degrees. The physical mechanisms underlying this effect are discussed by studying the vorticity dynamics in the wake of the foil. Hydrodynamic forces and moments allowed the computation of efficiencies, and the wake was quantified using Digital Particle Image Velocimetry. The momentum distribution in the wake of the foil has allowed the physical explanation for the cases with highest thrust production capacity. In terms of flexural stiffness the optimum flexibility has been determined with the semi flexible plate up to 69% of efficiency under a swept angle of 72 degrees for Re = $O(10^4)$ tested in the thesis.

UNIVERSITAT ROVIRA I VIRGILI
HYDRODYNAMICS OF PITCHING FOILS: FLEXIBILITY AND GROUND EFFECTS
Rafael Fernandez Prats
Dipòsit Legal: T 979-2015

INDEXED PUBLICATIONS

1. R. Fernandez-Prats, V. Raspa, B. Thiria, F. J. Huera-Huarte and R. Godoy-Diana, 2015. *Large-amplitude undulatory swimming near a wall*. Bioinspiration & Biomimetics. 10(2015)016003, doi:10.1088/1748-3190/10/1/016003.

2. F. J. Huera-Huarte, R. Fernandez-Prats, *Hydrodynamics of a rigid pitching foil in a uniform current*. Submitted.

3. R. Fernandez-Prats, F. J. Huera-Huarte. *Effect of chordwise flexibility on pitching plate propulsion in a uniform current*. Under preparation.

INDEXED CONFERENCES

1. R. Fernandez-Prats, F.J. Huera-Huarte. *Hydrodynamics Forces and DPIV in Pitching Foils*. (Technical Publication FEDSM2014-21465) Proceedings of ASME 30^{th} International Conference on Fluids Engineering Division Summer Meeting, ASME FEDSM, 2014, Chicago, IL, USA.

CONFERENCES

1. R. Fernandez-Prats, V. Raspa, B. Thiria, F.J. Huera-Huarte and R. Godoy-Diana. *Undulatory swimming close to a wall*. 10^{th} European Fluid Mechanics Conference, EFMC10, 2014, Copenhagen, Denmark.

2. R. Fernandez-Prats, F. J. Huera-Huarte. *Hydrodynamics in the wake of a pitching foil*. (Video Session) 66^{th} American Physical Society - Division of Fluid Dynamics, APS DFD, 2013, Pittsburgh, PA, USA.

3. R. Fernandez-Prats, F. J. Huera-Huarte.*Forces and vorticity in the wake of an oscillating foil*. (Poster Session) 65^{th} American Physical Society - Division of Fluid Dynamics, APS DFD, 2012, San Diego, CA, USA.

SEMINARS & TALKS

1. *Hydrodynamics forces and DPIV in pitching flexible foils* Oral presentation. E. T. S. Ingeniería Industrial. October 2014, Málaga, Spain.

2. *Undulatory swimming with ground effect* 11th Doctoral Day, Oral presentation & Poster session. April 2014, Tarragona, Spain.

3. *Analysis of bio-inspired propulsors with flexibility effects* Oral presentation. Séminaire Café, PMMH, ESPCI. September 2013, Paris, France.

4. *Forces and vorticity in the wake of an oscillating foil* 10th Doctoral Day. Oral presentation. April 2012, Tarragona, Spain.

Todos somos muy ignorantes.
Lo que ocurre es que no todos
ignoramos las mismas cosas.

Albert Einstein,

ACKNOWLEDGEMENTS

I'd like to thank Prof. Francisco Huera, my advisor, for his generous support, which was essential in the completion of this work. Thanks to Fran, who have taught me about life and work and fluid mechanics. I'll always hold myself to the standards I've learned here. To Zafar, whose friendship has made me a better researcher, coffee drinker, worker, serious ... and thanks I've learned a lot from you in these years. Funding from grant Spanish Ministry of Science DPI2009-07104 is gratefully acknowledged.

Agradecimientos para mi familia, la tesis se la dedico a ellos, Manuelas y Domingos. Gracias a todos los compañeros del despacho, laboratorios, comedor, calzotadas, futbol, padel. Agradezco mucho el trato en el Departamento de Ingenieria Mecanica y en el programa de doctorado. Todos habeis hecho que me sienta aqui como en casa y estoy muy agradecido. Gràcies també als meus últims correctors i traductors Warren, Idoia i Xavi.

Je tiens à remercier le soutien dans les laboratoire PMMH grâce à Ramiro, Benjamin et Veronica. Les compañneros français, les Cubains, les Hongrois et les Chiliens ont fait me sentir chez moi. Merci à ces gens de mon séjour à Paris était adorable et maintenant je adore Paris malgré la façon dont il est cher.

UNIVERSITAT ROVIRA I VIRGILI
HYDRODYNAMICS OF PITCHING FOILS: FLEXIBILITY AND GROUND EFFECTS
Rafael Fernandez Prats
Dipòsit Legal: T 979-2015

CONTENTS

LIST OF FIGURES

LIST OF TABLES

ACRONYMS, NOMENCLATURE & SYMBOLS

$DPIV$	Digital Particle Image Velocimetry
$DDPIV$	Defocusing Digital Particle Image Velocimetry
BvK	Bénard-von Kármán
FSI	Fluid structure interactions
MAV	Micro air vehicules
$AUVs$	Autonomous underwater vehicules
LEV	Leading edge vortex
TEV	Trailing edge vortex
POD	Proper Orthogonal Decomposition
St	Strouhal number
Re	Reynolds number
k_G	reduced frequency
AR	Aspect ratio
C_T	Coefficient of Thrust
C_P	Coefficient of Power
p_h	Relation, flexural stiffness vs surrounding fluid
EI	Flexural stiffness
ν	Kinematic viscosity
μ	Dynamic viscosity
ρ	Density of water
c	Foil chord length
L	Swimmer chord length
t	Time

s	Foil span
a	Foil area
ω	Angular velocity
U	Carriage speed
U_c	Cruise velocity
A	Theoretical oscillating amplitude
$A*$	Oscillating amplitude peak to peak
θ	Pitch amplitude
h	Thickness of the panel
f	Oscillating frequency of the foil
T	Period
f_c	Camera frequency
δt	Time between laser pulses
w	Vorticity
R_θ	Rotation matrix
f_0	Natural frequency
$x(t)$	Displacement of the foil
d	Dimensionless distance to the wall
F	Propulsive force, Thrust
F_{xp}	Instantaneous Thrust
$\overline{F_{xp}}$	Average Thrust
F_{yp}	Instantaneous Lift
$\overline{F_{yp}}$	Average Lift
M_{zp}	Instantaneous Torque

$\overline{M_{zp}}$	Average Torque
P	Instantaneous power input to the foil
$\overline{P}$	Average power input to the foil
η	Hydrodynamic efficiency
xyz	Cartesian coordinate systems

1 INTRODUCTION

An extremely interesting field of science is the exploration of the capabilities of nature, called biomimetics. In the first chapter an introduction with examples and applications of biomimetics are described. As well as general concepts, terminology and dimensionless parameters are introduced to improve the clarity of the document. We finish the first chapter with the motivation and objectives of the investigation.

Biomimetics, bioinspirations, biomimicry or bionics is a new scientific discipline that applies biological principles to develop new engineering solutions for medicine, industry, the environment, and many other fields that have previously not been touched by the biological revolution. Too many researchers are focusing in the nature for inspiration and they are looking for solutions to specific problems which have appeared recently. Many of the problems in the world have been resolved in a formidable way by nature for centuries. There many instances where nature has found a very efficient solutions and now scientists have a lot of resources to research new capabilities for exciting future technologies. Generally there are three areas in biology in which technological solutions can be modeled:

- Replicating natural manufacturing methods as in the production of chemical compounds by plants and animals. For example, how are spiders able to spin silk stronger than synthetic substances developed by man with only the input of insects?
- Mimicking mechanisms found in nature. For example, the flippers of the humpback[1] whale are a more efficient wing design than the current model used by the aeronautics industry on airplanes.

1 Frank Fish noticed that the leading edge of humpback whale flippers have tubercles or bumps. After testing, Fish realized that the tubercles on the flipper delay the stall angle by approximately 40%, while increasing lift and decreasing drag. Nowadays Frank Fish is the president of the company WhalePower.

- Imitating organizational principles from the social behavior of organisms like ants, bees, and microorganisms.

1.1 OUTLINE OF THE THESIS

In order to catalog the document, this thesis has been divided into seven chapters:

1. *Chapter one: Introduction*
   The field of biomimetics and the motivation of the research are presented. General concepts, terminology and dimensionless parameters are introduced to be used throughout the thesis.

2. *Chapter two: Literature Review*
   A selection of literature is reported from the fields of flapping foils, fish locomotion, wake topologies and hydrodynamic propulsion with three types of oscillations - pitching, heaving and both. The literature starts with rigid foils and finishes with flexible foils under ground effect. Experimental, theoretical and simulations studies with foils and live fish are commented on.

3. *Chapter three: Effect of the flexibility in flapping propulsion*
   The third chapter describes the experimental set up, apparatus of the mechanical models and the different physical parameters of the experiments. Methods of load measurements and optical measurements of the velocity fields are described. Results and discussion cover the analysis of the rigid foil and different flexibilities of the foils. We present coefficients of thrust and power, efficiencies, averaged of velocity fields and phase averaged vorticity fields are evaluated.

4. *Chapter four: Large-amplitude undulatory swimming near a wall*
   In chapter four the propulsive dynamics of a flexible undulating foil in a self-propelled swimming configuration with ground effect is studied. Measurements of the swimming speed and the propulsive force together with image acquisition of the kinematics of the foil, DPIV and visualization of its wake are computed.

5. *Chapter five: Conclusions*
   Summary of the main results from the work are presented. The findings in this research are established as well as perspectives of new potential avenues to investigate.

6. *Appendices*
   The Appendix contain supplementary detail of Snapshot Proper Orthogonal Decomposition technique used in chapter 4 as an aid to the understanding of the thesis.

7. *References*
   A list of journals, books and PhD documents that are referred to in this thesis.

1.2 GENERAL CONCEPTS

Throughout the thesis different fields in science like mechanical engineering, hydrodynamic, aerodynamic and biology are taken into account. In order to clarify to readers several ambiguities in these kind of fields, in the following subsection you can find the conventions adhered to in the thesis.

1.2.1 *Foil Axes, Forces and Torque*

It is necessary to establish the common words which are used in the thesis to avoid confusion. In figure 1.1 the reference system, axes and the basic size parameters of the foil are defined.

The terms *length* or *chord* and *height* or *span* refer to the horizontal and vertical orientation of the foil. These parameters are very important for the aspect ratio. In reference to the axes, pitching oscillation was produced in the z axis and the foil was moved in the negative x direction by the carriage. Therefore, the loads (forces and torques) can be defined from this figure. In the negative x direction the *thrust* was produced, at both sides of the y direction the $lift$ was produced and *torque* in the z axis.

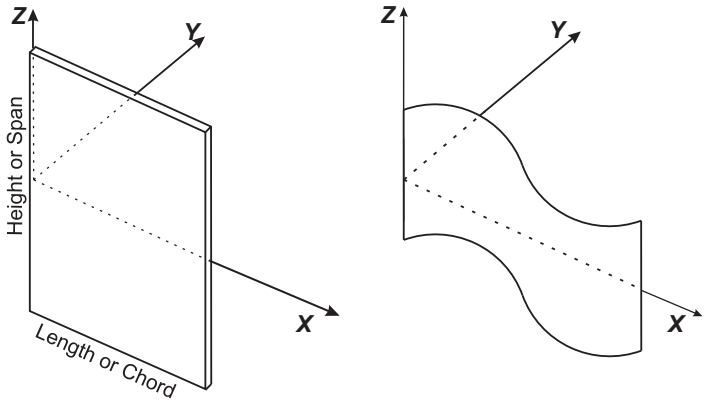

Figure 1.1: Axes and dimensions of the foils.

1.2.2 *Terminology for fins and forces on a swimming fish*

The terminology used in the manuscript to identify the fins and other features of the fish as well as the forces acting on a swimming fish are in figure 1.2:

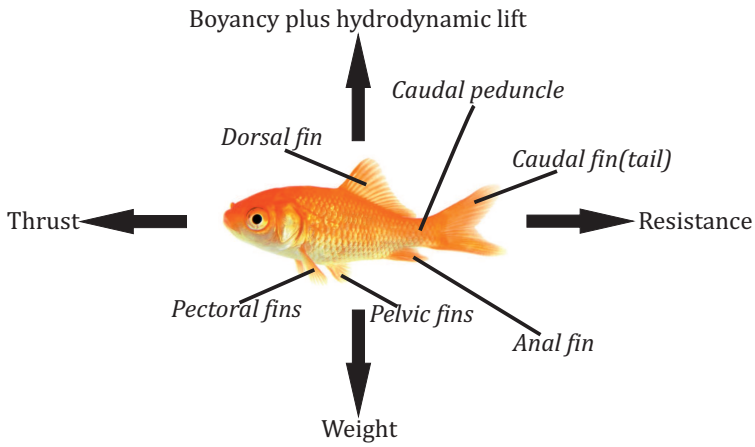

Figure 1.2: Different fins and forces on a swimming fish.

1.2.3 *Movement of the Foil*

In the literature it is common to find different terminologies for the oscillating foil. In this thesis the angular rotation of the foil in the z axis is referred to as *pitch* and linear movement of the foil in the y axis is referred as *heave*.

1.3 DIMENSIONLESS PARAMETERS

To generalize the results from the experiments, it is necessary to enumerate important dimensionless parameters in this field. Dimensionless numbers allow you to compare two different systems by combining the parameters of interest. Therefore, past experiments can be compared with the experiments from this thesis. The dimensionless parameters used in this thesis were:

1. Strouhal number is a dimensionless number describing oscillating flow mechanisms, which combines the flapping frequency, amplitude and forward speed:

$$St = \frac{fA}{U} \tag{1.1}$$

2. Reduced frequency or Garrick frequency is another important parameter governing flapping foil performance. Koochesfahani (1989), describes the number of foil oscillations in a given length:

$$k_G = \frac{\pi f c}{U} \tag{1.2}$$

3. Reynolds number gives a measure of the ratio of inertial forces to viscous forces:

$$Re = \frac{\rho U c}{\mu} \tag{1.3}$$

4. Aspect ratio is the span of a foil divided by its chord. When the foil is not rectangular the square of the span is divided by the wing area:

$$AR = \frac{s}{c} \tag{1.4}$$

5. A thrust coefficient describes how effectively thrust is produced by a propulsive device:

$$C_T = \frac{\overline{F_x}}{\frac{1}{2}\rho U^2 cs} \tag{1.5}$$

6. A power coefficient describes the power required to pitch the foil:

$$C_P = \frac{\overline{P}}{\frac{1}{2}\rho U^3 cs} \tag{1.6}$$

1.4 MOTIVATION & OBJECTIVES

For billions of years, animals have been forced to evolve by nature. Animals well adapted to the environment guarantee the success and survival of their species. Many species developed a multitude of propulsion and maneuvering methods adapted to their environments. Birds, insects and fish flapping their wings/fins at different length scales, leading to a different flow behaviour. The larger the animals, the lower the wings/fins flapping frequency required to propulse them. Fish have evolved not only to swim quickly or efficiently over large distances, but also to fit into different niches in aquatic environments.

The majority of fins have streamlined cross sections, more or less the same aspect ratio range, and oscillate to produce lift/drag-based propulsion.

Most of the aquatic animals are using their fins to swim in water with higher level of efficiency, manoeuvrability and agility than any man-made underwater vehicle. A source for highly effective design for bio-

inspired applications such as AUVs[2] and MAVs[3] is available in nature. However the understanding to develop biological propulsion is still a challenge because there is a lack of knowledge.

The objectives of the thesis are summarised in the following points:

- Build and implement a mechanical model actuator to research flapping propulsion.
- Investigate the unsteady forces of flapping foils by varying the Reynolds, Strouhal, sweep angles and flexural stiffness.
- Establish the role of the flexural stiffness in the propulsive performance.
- Research about the interaction of an undulatory swimming near a wall.
- Relate the swimming speed and efficiency with vortex structure through of DPIV.

2 Autonomous Underwater Vehicle
3 Micro Air Vehicle

UNIVERSITAT ROVIRA I VIRGILI
HYDRODYNAMICS OF PITCHING FOILS: FLEXIBILITY AND GROUND EFFECTS
Rafael Fernandez Prats
Dipòsit Legal: T 979-2015

2

BACKGROUND

The second chapter explains the main points of the literature reviews of the thesis; aerodynamics of thrust production, flapping at low Reynolds, dimensionless number in aquatic locomotion and the fish locomotion. The background of the field is divided into rigid and flexible foils propulsion, where descriptions and details of important findings of numerous investigations with oscillating kinematic of pitch, heave and both motions. Reviews on undulatory swimming with the presence of a boundary are presented to finish the literature of the thesis. The chapter ends with a list of engineering application systems such as autonomous underwater vehicles, where the flapping propulsion system has been implemented.

2.1 AERODYNAMICS OF THRUST PRODUCTION

Early research in flapping foils was done on the assumption of quasi-steady aerodynamics. Under this assumption, the forces are obtained from the instantaneous angle of attack as in a static wing and you do not take into account the previous motion. Later it was shown that the assumption of quasi-steady aerodynamics is sufficient at higher Reynolds numbers, in the order 10^5 or more. However this assumption is insufficient at low Reynolds number like 10^4 or below (Wang), this area still lacks knowledge. Ellington et al. (1996) explained "Supposedly someone did a back of the envelope calculation, taking the weight of a bumblebee and its wing area into account, and worked out that if it only flies at a couple of metres per seconds, the wings wouldn't produce enough lift to hold the bee up,". Therefore, the unsteady effects like vortex dynamics are very important and have to be taken into account at low Reynolds numbers.

Before the 21st century, many studies were done about wake of airfoils and wake of bluff bodies. von Kármán and Burgers (1935) found out under certain conditions of flow speed and viscosity, a bluff body placed in a moving flow of fluid will leave a pattern in its wake known as Bénard-von Kármán (BvK) as in fig.2.1a. Where the upper row of eddies rotate clockwise and the lower row anti-clockwise (for flow from left to right). This wake produces drag and the time averaged velocity profile from this wake is in fig.2.1b. The eddies are carried downstream from the body until their kinetic energy is dissipated by the viscosity of the fluid.

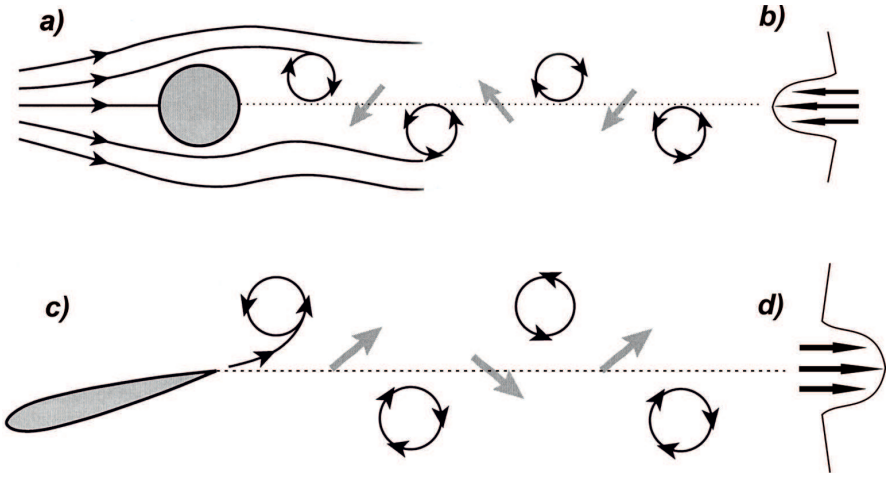

Figure 2.1: a) Von Kármán street and b) velocity profile. c) Reversed von Kármán street and d) velocity profile.

In the case of flapping foils, these wakes are reversed because foils produce thrust by inducing a jet flow in the opposite direction. These wakes are called as Reverse von Kármán street (fig.2.1c) and the time averaged velocity profile is a jet (fig.2.1d), which indicates production of thrust, rather than drag. Early research with theoretical analyses (von Kármán and Burgers (1935); Garrick (1937)) as well as experimental studies (Katzmayr (1922); Koochesfahani (1989)) showed an improvement of thrust at certain combinations of oscillation frequency and amplitude.

A variety of wakes can be formed by oscillating a cylinder laterally in the free stream as shown by Williamson and Roshko (1988). The wakes behind the oscillating cylinders include Bénard-von Kármán-type wake, in which two vortices of opposite sign are shed per oscillation period (2S)[1] and a wake in which two pairs of vortices are shed per oscillation period (2P)[2]. Bratt (1953) visualized 2S and Koochesfahani (1986) visualized 2S and 2P wakes behind a foil performing pitching oscillating in a free stream. Godoy-Diana et al. (2008) characterized the transition from the Bénard-von Kármán wake to the reversed vortex street and the symmetry breaking of the reverse Bénard-von Kármán pattern. The reverse BvK wake plays an important role in flapping locomotion (Lighthill (1969); Sfakiotakis et al. (1999); Triantafyllou et al. (2000)); also, more complex wakes were shown by Schnipper et al. (2009) like 2P+2S, 4P, 4P+2S, 6P+2S or 8P as you can see in the figure2.2.

1 2S-type wake or Bénard-von Kármán with two single vortices.
2 2P-type wake, two pairs of vortices and each of them pairs with an opposite-sign vortex.

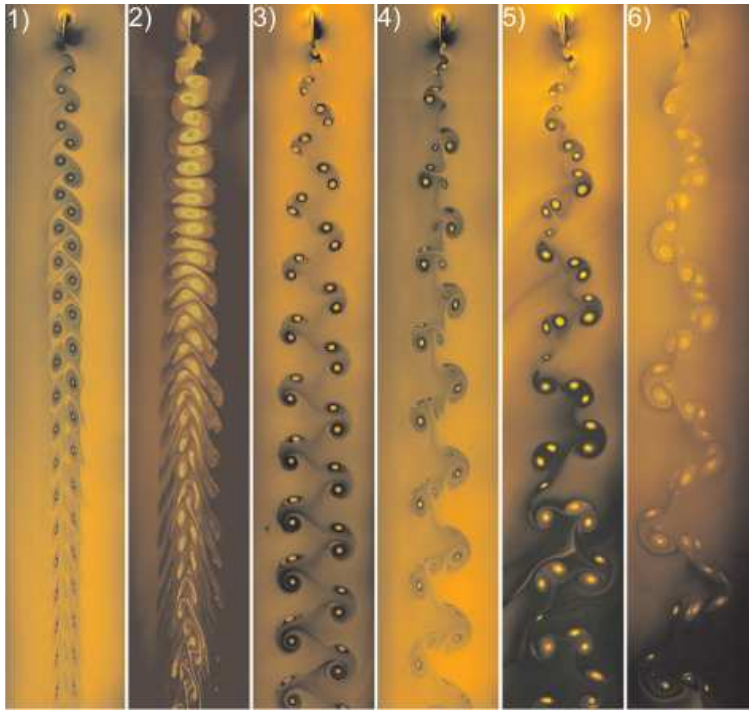

Figure 2.2: 1) BvK, 2) reverse BvK, 3)2P, 4)2P+2S, 5)4P, 6)4P+2S. Adapted from Schnipper et al. (2009).

2.1.1 *Types of Instability*

The flow past an oscillating fin can be classified as an unstable steady flow and it is divided into two categories:

- Convective instability: the body causes a perturbation that is then carried downstream by the wake.
- Absolute instability: the perturbation is developed close to a body that caused it, and is not carried away in the wake.

An example of convective instability is a reverse BvK because the trailing and leading edge of the foil can produce eddies which are carried downstream by the wake.

2.2 FLAPPING AT LOW RE

Re number is defined as the ratio of inertial forces to viscous forces and can classify different flight regimes, natural phenomena and technology in function of the velocity as you can see in figure 2.3. Birds, fish, batteries and sperms belong to different regimens, from $Re > 1$ until $Re < 10^5$. Within of this range of Re, hydrodynamic and aerodynamic forces in the foils are dominated by the pressure and the viscous effects are concentrated in the boundary layer surrounding the body. While the flapping is executed the viscous layer is shed to form coherent structures as vortices, where the propulsion of the animal is generated.

Depending on the fluid, the mechanisms of the propulsion forces are different. On the one hand, birds should generate continuous lift force while they are flying to overcome their weight. They manage a complex kinematic to optimize their flights and take the advantage of LEV[3] to generate extra lift. On the other hand, aquatic propulsion does not need to generate lift. Generally fish have a swim bladder to control their buoyancy, and thus stay at the water depth without having to waste energy in swimming. The most important force in aquatic propulsion is thrust, water is 1000 times denser than air, optimization of drag reduction is a must.

3 LEV is generated from the balance between the pressure gradient, the centrifugal force and the Coriolis force in the momentum equation. It is effectiveness in promoting lift is correlated with a flyers's sizes. Numerous issues related to the interplay among wing structures (including its anisotropic deformability), flapping kinematics, large vortex structures, and Reynolds number remain unresolved (Shyy and Liu, 2007).

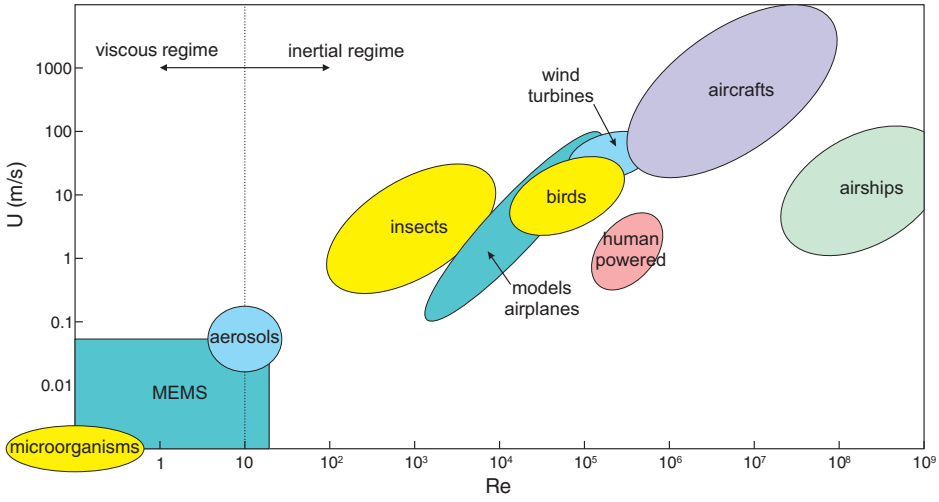

Figure 2.3: Different flight regimes, natural phenomena and technology in function of the Reynolds number and velocity. Adapted from Lissaman (1983).

2.3 DIMENSIONLESS NUMBERS IN AQUATIC LOCOMOTION

Many researchers (Lighthill (1969); Maxworthy (1981); Ellington (1984)) have tried to find out about, using experimental and theoretical method the main frequency selection nature in aquatic animals, birds and insects. In the early 1990s it was proposed that Strouhal number be used as the non-dimensional parameter governing wake patterns and in a range of $0.25 \leq St \leq 0.35$ thrust production is maximized. Triantafyllou et al. (1993) presented their discovery of an optimal range of St, and how it can be predicted using a two-dimensional linear stability analysis in the wake of a pitching foil. The resulting wake formation was a staggered array of vortices in the opposite direction of the classic Bénard-von Kármán street. They experimentally measured the propulsive efficiency of an airfoil undergoing combined pitching and heaving motion to simulate the "carangiform" tail motion employed by aquatic animals. Finally they determined that St is of particular relevance to the efficiency of fin being used for oscillatory propulsion. Fish, sharks and cetaceans operate at peak efficiency at a St of 0.25 to 0.35 within a Reynolds number range 10^4 to 10^6. Taylor et al. (2003) compiled St (fig. 2.4) resulting from cruise

swimming or flying, of more than 40 species, showing ranges previously indicated by Triantafyllou et al. (1993). Focusing only on swimming animals Eloy (2012) grouped 53 different species to present the consistency of the St in a slightly larger range.

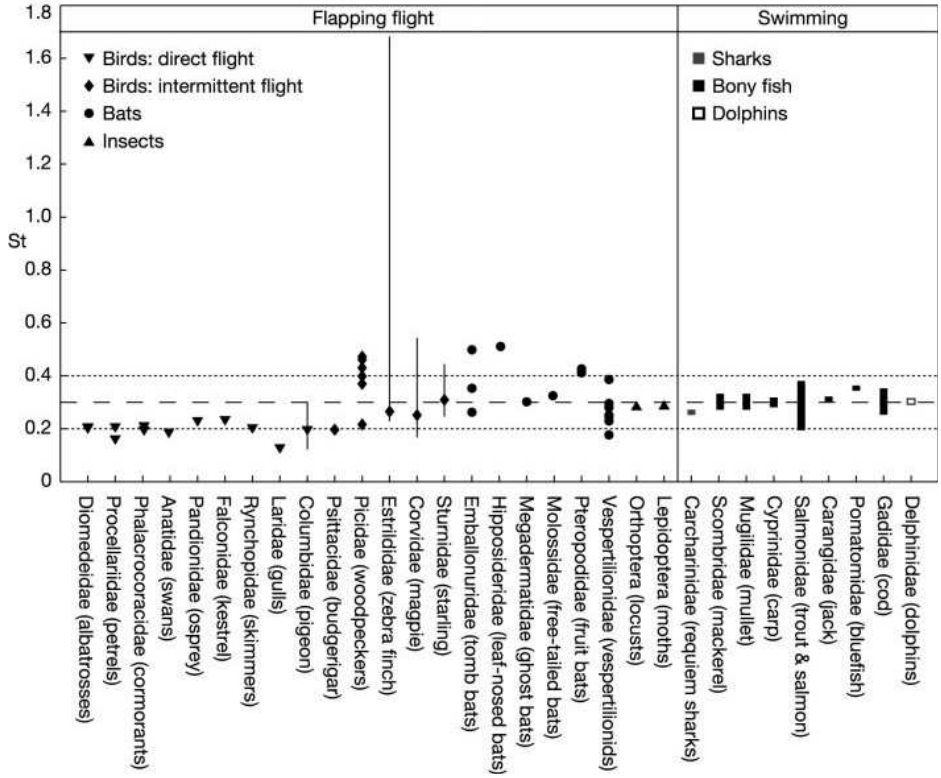

Figure 2.4: Strouhal number for 42 species. Dotted lines mark the range $0.2 < St < 0.4$, in which propulsive efficiency usually peaks. Adapted from Taylor et al. (2003).

Recently, Gazzola et al. (2014) emphasized that St captures only one length scale as A∼L, and St does not take into account the varying fluid environments characterized by ν. They presented a new dimensionless swimming number as:

$$Sw = \frac{\omega A L}{\nu} \tag{2.1}$$

This number scales the aquatic locomotion with animals from a few millimeters to 30 metres, across a wide array of biological taxa, from over 1000 measurements on fish, amphibians, larvae, reptiles and mammals. Sw captures the two length scales associated with the tail amplitude (A) and the body size (L), the fluid environments (ν), input kinematics (ω) and output velocity (U). They proposed a scaling as a power law $Re - Sw^{\alpha}$, with α=4/3 for laminar flow and α=1 for turbulent flows. This scale computed good agreement with measurements (over 1000 species, see fig.2.5) and simulations (two and three-dimensional DNS[4]).

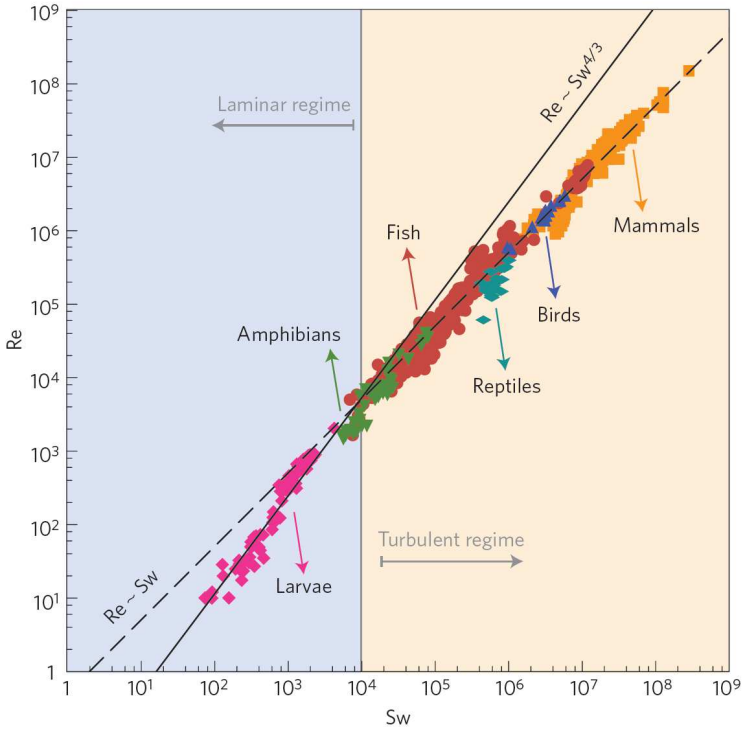

Figure 2.5: Scaling aquatic locomotion, species measurements. Adapted from Gazzola et al. (2014).

4 Direct numerical simulation

2.4 FISH SWIMMING LOCOMOTION

The fish locomotion involves the transfer of the momentum from the body to the surrounding water (and vice versa).

2.4.1 *Tyes of Locomotion*

Fish locomotion has been classified into two generic categories on the basis of the movements's temporal features:

- *Periodic (or steady) swimming*: these fish have cyclic movements and they are able to cover large distances.
- *Transient (or unsteady) swimming*: these fish are more agile and they are able to perform escape maneuvers and turns to avoid predators.

Most fish achieve thrust by bending their bodies into a backward-moving propulsive wave that extends to their caudal fins, defined as body or/and caudal fin (BFC) locomotion. Other fish have developed different type swimming locomotion using their median and pectoral fins, which is classified as median and/or paired fin (MPF) locomotion, all of these kinds of locomotion are shown in fig. 2.6.

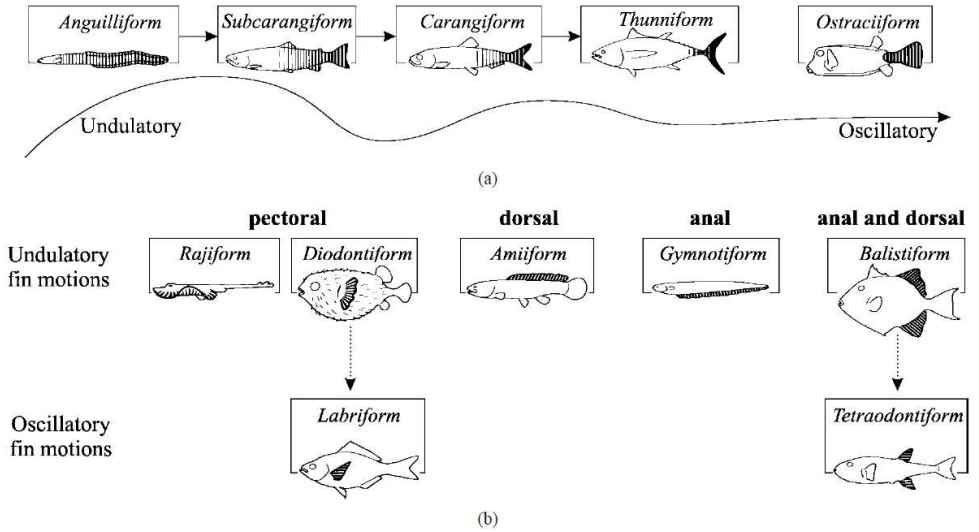

Figure 2.6: Swimming modes associated with a) BCF propulsion and b) MPF propulsion. Shaded areas contribute to thrust generation. Adapted from Lindsey (1978).

In the Anguilliform locomotion all the thrust is originated from the contraction of body musculature. Sinusoidal undulations of the body with a series of successive S-shaped curves seem to be the basic or primitive mode of swimming in vertebrates. Because so much of the body participates, there are increased drag forces, making this a relatively inefficient mode of locomotion. However, most fish do not swim this way, they rely on a much smaller part of the body which is the caudal fin.

In the evolutionary process of fish, there has been a gradual change from the undulation type of locomotion toward the caudal fin type of propulsion (fig.2.7).

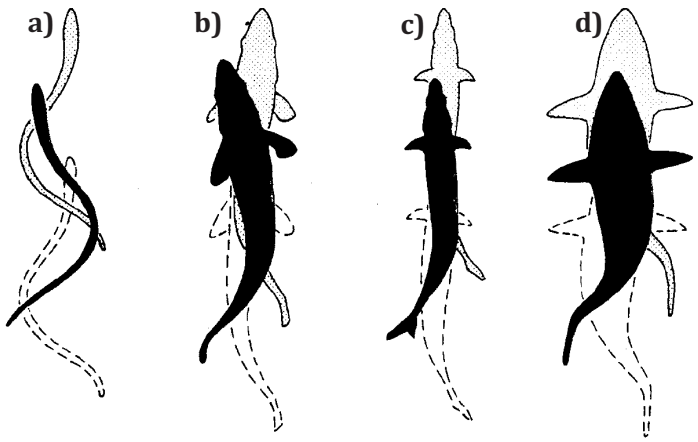

Figure 2.7: Gradation of swimming modes from primitive to derived, a) anguilliform, b) subcarangiform, c) carangiform and d) thunniform. There are a superimposed silhouettes on successive positions. Adapted from Lindsey (1978).

In caudal fin locomotion it is possible to combine maneuverability and high speed. In this group there are four subcategories known as subcarangiform, carangiform, thunniform and ostraciiform. This thesis is focused on the thunniform subcategory because of it is considered a culminating point of the evolution of swimming designs to travel. Teleost fish, sharks and marine mammals are able to maintain high cruising speeds to be maintained for long periods. Thunniform locomotion is caudal locomotion developed to the extreme. Burst swimming speeds of greater than 20 meters per second have been recorded in certain fish that employ thunniform locomotion. In thunniform swimmers, very little of the body musculature is involved in providing forward progress. 90% of the thrust is produced by the oscillation of the caudal fin and the rest by a narrow caudal peduncle. The caudal fin is stiff and high with a crescent-moon shape often referred to as lunate. Thus, the design of thunniform swimmers is optimized for high-speeds in calm water and is not well-suited to other actions such rapid acceleration, turbulent water or turning maneuvers.

2.4.2 *Wakes behind fish*

Many investigations have been carried out to unveil the complexities of fish locomotion. The patterns that a swimming fish leaves behind, reveal certain important structures. Most wake studies started with the development the new technologies and methods like Digital Particle Image Velocimetry (DPIV).

Pairs of rings

Drucker and Lauder (2002) studied and quantified the locomotor forces and the coherent structures of bluegill sunfish (*Lepomis macrochirus*), using the technique of DPIV to visualize the water flow in the wake of the fish. These fish use their pectoral fins for low speed locomotion and at higher speed the use their caudal fin. At low speed, vorticity is shed by each fin during the downstroke and stroke reversal creating a roughly symmetrical vortex of near-uniform circulation with a central jet of high velocity flow. At high speed, additional vorticity appears on the upstroke, indicating the production of linked pairs of rings by each fin. These pattern of vortices are in figure 2.8.

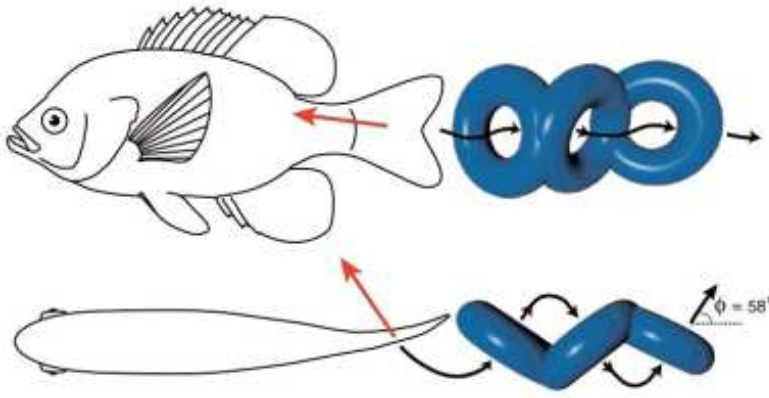

Figure 2.8: Pattern of vortex wake of a sunfish. Adapted from Wilga and Lauder (2004).

Ring-within-a-ring

More complex wakes are formed in the wake of the dogfish shark. Wilga and Lauder (2004) found, while researching wakes with DPIV, that the shark's tail generates a ring-within-a-ring vortex structure, in contrast to the single rings shed by symmetrical fish tails. The branched-ring vortex is generated by the inclined angle of the tail's trailing edge and by its motion at an angle to the horizontal body axis; the vortex directs water backwards and downwards, which may increase manoeuvrability of the sharks. In figure 2.9 you can see the centres of vorticity. The counter rotating center vortex produces jet *A*, and jet *B* is produced as a result of flow induced by the central tip vortex. Jets *A* and *B* are directed, on average, at 35 degrees to the freestream flow, before combining to produce a single broad jet *C*.

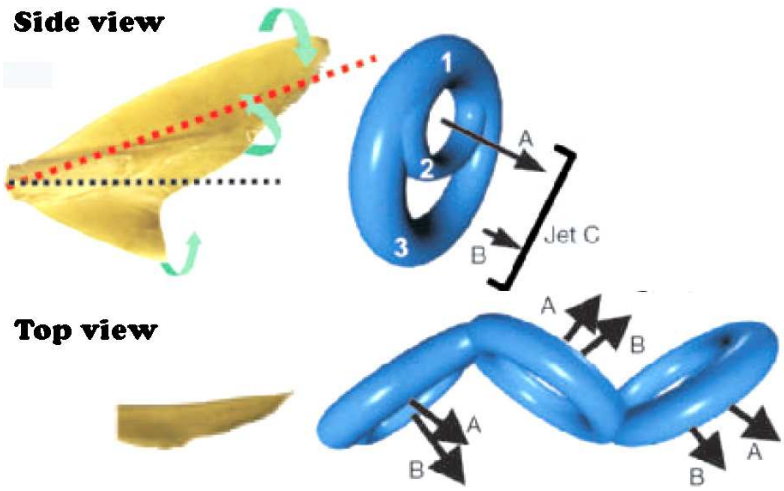

Figure 2.9: Shark vortex wake. Adapted from Wilga and Lauder (2004).

2.5 REVIEW OF INVESTIGATIONS IN FLAPPING PROPULSION

The investigations referenced in this section have been divided in two groups, rigid and flexible foils. Each group has three subgroups pitch,

heave and both. To carry out these investigations, the researchers have used plates, airfoils mostly of the $NACA$ 0012[5] type.

2.5.1 *Investigations with rigid foil propulsion*

PITCHING WITH RIGID FOIL: From our knowledge, the first research of thrust for an oscillating rigid airfoil was carried out by Knoller (1909) and Betz (1912), they were some of the first to explain the mechanism of thrust generation for such flapping foils. In the middle of 1930s a theoretical explanation about the different patterns of a large-scale drag wake and a thrust wake was given by von Kármán and Burgers (1935). Following these studies, theoretical models by Garrick (1937) were done under oscillating foils in inviscid flow. Koochesfahani (1989) visualized the vortical flow patterns in the wake of a $NACA$ 0012 airfoil pitching at small amplitudes. He showed how it is possible to modify the wake by varying the amplitude, frequency and shape of the oscillation waveform. More recently flow visualization of a pitching foil with an $AR = 0.54$ in a free stream with a $St = 0.34$ was investigated by Buchholz and Smits (2006). Buchholz proposed a vortex skeleton model for the wake formation as you can see in fig. 2.10. Buchholz and Smits (2008) investigated wake structures and thrust performance of a rigid low aspect ratio pitching panel for Re=$0(10^4)$. Thrust coefficient was found to depend primarily on the St and the AR, propulsion efficiency was sensitive for $AR < 0.83$. They measured peak efficiencies between 9%-21%. In the wake structures they visualized the reverse BvK when operated at or near peak efficiency. Dong et al. (2005) and Guglielmini (2004) carried out numerical work coinciding with previous experimental studies. Godoy-Diana et al. (2008) studied with a rigid pitching foil, the transition of the BvK to the reverse BvK which is produced because of the actual drag-thrust transition. Measurements of the unsteady pressure distributions were compared with time averaged thrust performance

5 The National Advisory Committee for Aeronautics $NACA$ of the USA devised the four digit airfoil series to simplify and standardise airfoil design.

and wake visualizations in a pitching panel by Green and Smits (2008). AR and the amplitude of the pitching affected the pressure distribution on the plate as well as the thrust and the vorticity. Green et al. (2011) used DPIV and LCS[6] to investigate the unsteady three-dimensional wake produced by a trapezoidal pitching panel. Green et al. (2011) observed the reverse BvK in the mid span and vortices realigned with strong interactions near the spanwise edges of the wakes.

In general the wake structures generated with pitching foils (Koochesfahani; Buchholz and Smits; Green and Smits) resemble the wake structures observed behind swimming fish discussed in the previous section (Drucker and Lauder; Wilga and Lauder). Therefore, these similar structures reveal that the counter rotating vortices (reverse BvK) are fundamental structures in flapping propulsion.

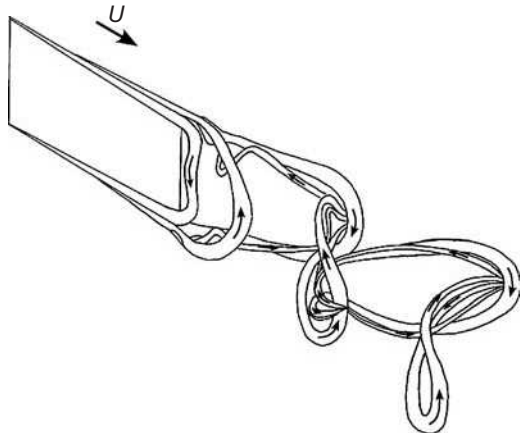

Figure 2.10: Three-dimensional vortex skeleton model proposed by Buchholz and Smits (2006).

HEAVING WITH RIGID FOIL: There are not to many studies with a rigid heaving airfoil in the literature. Lai and Platzer (1999) studied the change from drag producing wake flows to thrust producing jet flows using dye visualization. Their LDV[7] measurement revealed

6 Lagrangian coherent structure
7 Laser Doppler Velocimetry

the importance of the dimensionless heave velocity ($2\pi fA/U$) because the streamwise was maximum as soon as the dimensionless heave velocity exceeded 0.25. Vandenberghe et al. (2004) investigated the dynamics of the wing, flapping up and down (heaving) and free to move horizontally. The wings started to move forward as a critical frequency was exceeded (*flapping flight*), where a symmetry-breaking bifurcation from a pure flapping state with no horizontal motion. They visualized common patterns such as reverse *BvK* and Re based on the flapping frequency characterized by the bifurcation. Alben and Shelley (2005) studied numerically the dynamics of a body heaving up and down within a viscous fluid and free to move horizontally. They showed how the locomotion can be transduced from the simple oscillations of a body through an interaction with its fluid environment. Prangemeier et al. (2010) manipulated the trailing edge plunging motion to compare the effect so-called *quick pitch* with a pure sinusoidal plunge motion. The investigation with *quick pitch* summarized that the TEV circulation can be reduced by more than 60% and facilitate an earlier flow reattachment at the bottom of the stroke.

PITCHING AND HEAVING WITH RIGID FOIL: Experiments with simultaneous heaving and pitching motions increase the complexity of the model; however it is able to mimic better not only the oscillation motion of the caudal fin (pitch), but also the motion of the caudal peduncle (heave). It is common to impose a sinusoidal motion to each degree of freedom (pitch and heave). This combination generates two extra parameters in the foil trajectory like *phase offset* and *angle of attack profile*, as well as a new avenue to investigate so-called *active vorticity control*. Phase offset is defined by the phase between pitch and heave. Anderson et al. (1998) found the phase offset a key parameter in the interaction between LEV and TEV and the maximum efficiency reported in his experiments was as high as 87% under conditions of the optimal wake formation (reverse *BvK*). Read et al. (2003) established a phase angle of 90 degrees to produce efficient and high thrust, which is widely

used today. Effect of four specific angle of attack profiles was investigated by Hover et al. (2004). These profiles were: (i) simple harmonic motion in both heave and pitch motion, (ii) a square wave, (iii) a symmetric sawtooth wave, and (iv) a cosine function. The cosine angle of attack achieved improvement in the sense of high thrust values with reasonable efficiency. However, the highest thrust coefficients were generally found in the sawtooth profile. Reverse *BvK* wake was visualized in all the profiles.

Active vorticity control falls within flow control, which increased attention within a variety of applications. There are two major categories: passive control, in which flow control is achieved by altering the geometry of the flow; and activate control, in which a time-dependent force is applied to the flow. Active vorticity control is a method that some fish use to extract energy from their own LEV or capture energy from environmental vortices (Liao et al., 2003). This effect was studied experimentally with simultaneous heaving and pitching motions by Gopalkrishnan et al. (1994) and Anderson (1996). Varying St, pitch amplitude and heave/pitch phase angle Ellenrieder et al. (2003) showed interesting three-dimensional structures using dye flow visualization at Re=164. Numerical results published by Blondeaux et al. (2005) were compared with the flow visualizations of Ellenrieder et al. (2003) with good agreements. Blondeaux et al. (2005) investigated the dynamics of the vortex rings by varying the St. Relatively small values of St showed a weak interaction between adjacent rings and they are mainly convected downstream by the current. However, large values of St developed a strong interaction among adjacent rings where a reconnection phenomena takes place.

2.5.2 *Investigations with flexible foil propulsion*

Despite the important role of flexibility in the wings or fins of animals, the stiffness of the animals wings/fins when they are flying/swimming is still unclear (Maxworthy (1981) and Triantafyllou et al. (2000)).

Tables 2.1, 2.2 and 2.3 provides a compilation of works with flexible foil propulsion:

Table 2.1: Works of chordwise flexibility I.

Authors	Model-Kinematic	Re	St-k_G	Structural information
Heathcote and Gursul	Airfoil	$(0.8-2.1)\times10^4$	-	$E=205GPa$, ρ_s=7800kg/m^3
	Heave		-	h_s=$(38-5)\times10^{-5}m$
Ishihara et al.	Dipteran wing	2×10^2	0.054	$E=6.1GPa$
	Pitch/Heave			$G_w=(0.8-15.4)gcm^2/s^2rad$
Vanella et al.	Beam	$(0.75-10)\times10^2$	–	Frequency ratio:
	Pitch/Heave			$1/2, 1/3, 1/4, 1/6$
Yamamoto et al.	Airfoils	10^4-10^5	–	Elasticity of flexible
	Pich/Heave			part: $3.3-40mm/N$
Prempraneerach et al.	Airfoils	4×10^4	$0.1-0.45$	Rubber
	Pich/Heave			$E=3.2-50.6GPa$
Tang et al.	Plate	$(0.1-9)\times10^3$	1.4	$E=205GPa$, ρ_s=7850kg/m^3
	Heave			h_s=$(38-5)\times10^{-5}m$
Chandar and Damodaran	Airfoil	$(0.001-4.5)\times10^4$	-	-
	Heave			
Pederzani and H.	Airfoils	5×10^2	0.45	Membrane of Latex
	Heave			ρ_s=$0.5-1kg/m^3$
Chaithanya and Venkatraman	Plate	Inviscid	-	-
	Pitch/Heave			

Table 2.2: Works of chordwise flexibility II.

Authors	Model-Kinematic	Re	St-k_G	Structural information
Gulcat	Airfoil	$(1-100)\times10^3$	$0.5-1.5$	Prescribed camber
	Heave			
Miao and Ho	Airfoils	$(1-100)\times10^3$	$1-6$	Prescribed wing deformation
	Heave			
Toomey and Eldredge	Two elliptical	$(1-72)\times10^2$	-	Linear spring-damper model
	sections connected		-	$k=0.0068kgm^2/s^2$
	Pich/Heave		-	$r=0.0039kgm^2/s$
Heathcote and Gursul	Airfoils	$(0.75-2.1)\times10^4$	$0.17-0.4$	$E=205GPa$, ρ_s=$7800kg/m^3$
Heathcote and Gursul	Heave			h_s=$(38-5)\times10^{-5}m$
Michelin and Llewellyn Smith	Plate	Inviscid	$0.08-0.8$	Euler Bernoulli equation
	Heave			$\prod_1=10^{-2}-10^2$
Du and Sun; Du and Sun	Insect wing	$(2-40)\times10^2$	-	Prescribed wing deformation
	Pitch/Flap			
Miller and Peskin	Beam	10	-	EI=$6.9\times10^{-7}-1.1\times10^{-5}$ N/m^2
	Clap/Fly			

Table 2.3: Works of chordwise flexibility III.

Authors	Model-Kinematic	*Re*	*St*-k_G	Structural information
Zhao et al.	Fruitfly impulsive Pitch/Flap	2×10^3	-	EI_c=$4.39 \times 10^{-6} - 8.23 \times 10^{-4}$ nm^2
Bergmann and Iollo	Airfoil BCF/Jellyfish	$10^3 - 10^4$	-	Prescribed body deformation
Zhang et al.	Plate Heave	$(1 - 15) \times 10^2$	$0.1 - 0.5$	Lumped-torsional-flexibility model
Wen and Lauder	Plate Heave	$(2 - 6) \times 10^4$	$0.32 - 0.46$	EI=$9.9 \times 10^{-4} - 3.3 \times 10^{-5}$ Nm^2
Barannyk et al.	Plate Pitch/Heave	44×10^3	$0.1 - 0.46$	PDMS, 3 ratio of rigidity 100%, 50%, 15%
Kim and Gharib	Plate Translating	2×10^3	-	Policarbonate $E = 2.4GPA$ ρ_s=$1.2g/m^3$ $p_h = 0.4$
Kim et al.	Inverted flag self-excited	$33 - 170 \times 10^3$	-	Policarbonate $E = 2.4GPA$ ρ_s=$1.2g/m^3$
Hu et al.	Two Wing Fly	$1 - 10 \times 10^4$		Wood/Nylon/Latex

PITCHING WITH FLEXIBLE FOIL: Ahlborn et al. (1997) explored the importance of the flexibility for propulsive force of fast-start swimming with good agreements of experiments and theoretical predictions. Kemp et al. (2003) compared the propulsion of conventional propeller versus flexible fin and they reported that flexible foils have the ability to store energy and release it to the water out of phase with the driving torque. In a collaboration between Nekton Research with a Florida Atlantic University, they reported that rigid foils produce more thrust but need more torque than flexible foils Hobson et al. (2002, 2003). They carried out many experiments in the field of flexible foil propulsion for Nekton Research[8]. Their progress was commercially applied, thus it remains unpublished.

Kobayashi et al. (2006) developed a novel propulsion mechanism using dynamic variable-effective-length springs (see fig.2.11a). The elasticity of the foil was not constant and varied according to the different tasks. The effective length of a plate spring is changed by adjusting the length of the rigid plate that supports the plate spring. Another propulsion mechanism was developed by the same research group using a variable stiffness foil with torsional rectangular plates (see fig. 2.11b). They evaluated the behaviour of the variable stiffness in terms of thrust and flow fields surrounding the foil. Results revealed optimal stiffness combination values for each combination of frequency and amplitudes. These investigations reflect new mechanisms to research with active stiffness control and offer beneficial performance.

8 Private company in Duke University.

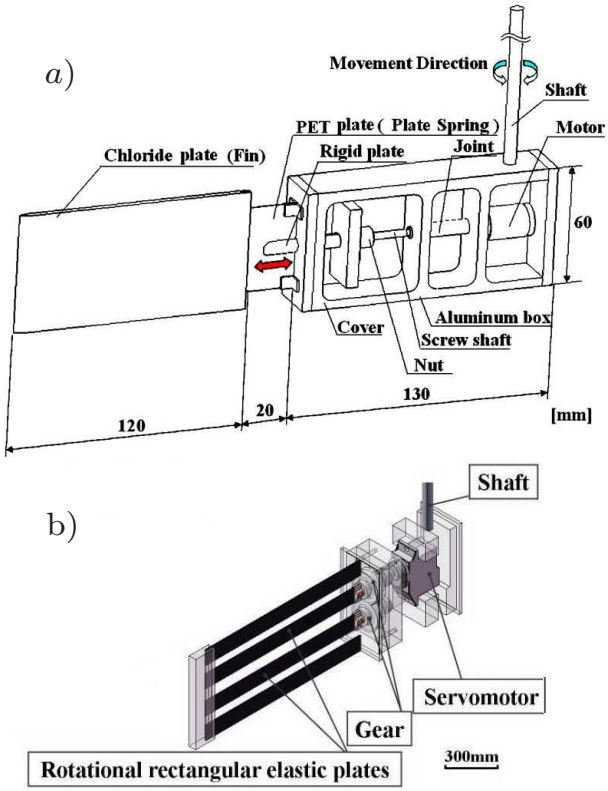

Figure 2.11: a) Foil with variable-effective-length spring b) mechanism of rotational rectangular elastic plates.Adapted from Kobayashi et al. (2006)

Alben (2008) presented a numerical study of the propulsive force generated by a flexible body pitched periodically at the leading edge in the small-amplitude regime. The thrust power generated by the body obtained a series of resonant peaks with respect to rigidity, which were determined. The highest of these peaks was detected when the body flexed upwards at the trailing edge, in an approximately 1/4 wavelength mode of deflection.

The advantages on propulsion of a biomimetic foil mimicking the flexural stiffness profile of a Pumpkinseed Sunfish (*Lepomis gibbosus*) versus a standard NACA0012 were researched by Riggs et al.

(2010). The superior performance of the biomimetic foil established a more optimal choice for maximising the thrust.

HEAVING WITH FLEXIBLE FOIL: Heathcote and Gursul studied chordwise flexibility on flapping foils at zero freestream velocity (Heathcote and Gursul, 2004) and spanwise flexibility on flapping foils at low Reynolds (Heathcote and Gursul, 2007a,b). In these three investigations, they carried out experiments with more than 6 different flexural stiffness and clarified important findings in order to maximize the propulsion and efficiency. The phase angle between the induced pitch and the heave oscillation was found to be an important factor in the efficient generation of thrust. Chordwise flexibility in pure heave motion is beneficial for low Reynolds numbers. A certain grade of flexibility was found to increase both thrust coefficient and propulsive efficiency. However, too much flexibility was found to be detrimental. In a numerical study, Pederzani and H. (2006) contributed showing that the density of the airfoils is a key parameter in determining efficiency and power. They described that heavier airfoils are shown to produce less output power and require proportionately less input power.

During simulations performed using the commercial code Fluent 6.1, Miao and Ho (2006) reported the formation and evolution of a pair of LEV along the flexible foil. The thrust wake structure was generated when the flexure amplitude of the airfoil was less than 0.5 of the chord length and a 0.3 enhancement in the propulsive efficiency was observed to a St of 0.255.

Potential flow theory with prescribed camber deformation by Gulcat (2009), computed that the periodically changing camber developed an increase in the averaged propulsive force. The oscillatory pure camber not only provided extra propulsive force for high Reynolds numbers and high amplitudes, but also prevented the flow separation by reducing the effective angle of attack. Tang et al. (2007) reported similar flow fields within the range of the flexibility considered. However, noticeable differences in lift and thrust forces generation were computed by the passive pitching

motion of the flexible airfoil. Wen and Lauder (2013) studied the kinematic, power consumption and wake flow patterns of 4 flexible foils with 2 different lengths at a variety of axial oscillation amplitudes. They identified a "critically-oscillated" amplitude of axial motion at which the cyclic oscillations in axial locomotor force were greatly reduced throughout the flapping cycle.

PITCHING AND HEAVING WITH FLEXIBLE FOIL: Yamamoto et al. (1995) studied an oscillatory propulsion control system with different flexibilities of fins as a vehicle actuator in ship models. Fins with seven flexibilities were tested, the fin with 15% rigidity obtained the best efficiency up to 31%. Prempraneerach et al. (2003) explained, a properly selected chordwise flexibility can develop an enhancement up to a 36%, compared to the efficiency of a rigid foil. They performed propulsive analysis with seven chordwise flexibilities and introduced a new non-dimensional flexibility parameter.

Aerodynamic forces on flapping wings were studied by Zhao et al. (2009b). They analysed 16 flexural stiffness, summarizing that the aerodynamic forces can be controlled by altering the trailing edge flexibility of a flapping wing and thereby controlling the magnitude of the LEV. Barannyk et al. (2012) investigated the thrust force and the hydromechanical efficiencies. Propulsive efficiencies up to 80% were achieved by varying the St, the depth of submergence and the chordwise flexibility.

Toomey and Eldredge (2008) analyzed numerically and experimentally with good agreement the fluid dynamic of a flapping wing with low order of flexibility. The problem discussed, consisted of a two-dimensional two-component wing structure connected by a single hinge with a damped torsion spring. The lift force and wing deflection were both found to be controlled by the wing rotation. The rotation phase lead shifted the instant of peak detection and notably increased the mean lift. Vanella et al. (2009) found numerically that the best performance for a flexible wing is generated when the wing is excited by a non-linear resonance at $1/3$ of the

natural frequency. Efficiencies between the flexible wings versus the rigid ones at a Re of 75, 250 and 1000 were 28%, 23% and 21% respectively. Chaithanya and Venkatraman (2008) investigated numerically the propulsive characteristics of a chordwise flexible foil in a potential flow. A beneficial force component along the forward velocity direction was computed by the deformed foil. Lower flexural stiffness obtained more thrust with less effort than high flexural stiffness. They summarized, for high values of propulsive efficiencies and thrust coefficients, the foil should be light and flexible.

2.6 UNDULATORY SWIMMING NEAR A WALL

Biolocomotion in fluids is in many cases influenced by the presence of a boundary. A well known observation is the case of bird flight near a surface, where the animal can glide with a fixed wing configuration for long distances without loss of altitude Withers and Timko (1977); Blake (1983). This so-called *ground effect*, which is also of importance in the aerodynamics of aircraft Staufenbiel and Schlichting (1988) and cars Katz (2006), can account in some cases such as the gliding flight of pelicans for induced drag savings of up to 50% Hainsworth (1988). The physical mechanisms governing the dynamics of the ground effect in such cases where the lifting surface is steady have been extensively studied (see e.g. Cui and Zhang (2010) for a short general review or Rayner (1991) for an in-depth discussion applied to animal flight). The most often cited mechanisms are related to the reduction of downwash in presence of a substrate. In particular, the fact that induced drag is reduced because wing-tip vortices are inhibited by the presence of the boundary, as well as the enhanced pressure between the lifting surface and the substrate. Moreover, it has been shown that the ground effect acts to increase not only the lift in steady flight but also the thrust and propulsive efficiency in oscillating modes Tanida (2001); Quinn et al. (2014b)

In the case of fish, some species such as batoids swim very close to the substrate, making ground effects an unavoidable element of their locomotor strategy Blevins and Lauder (2013). The main kinematic trait of

the pectoral fin of batoids is the production of a backward-propagating wave Blevins and Lauder (2012); Rosenberger (2001), and the physics of the interaction of such an undulating flexible body with a close boundary are likely to be if not completely different, at least significantly modified with respect to their steady counterparts cited above. These issues have only very recently been started to be addressed, for instance using heaving flexible panels Quinn et al. (2014b) where the ground effect was shown to provide notable hydrodynamic benefits in the form of enhanced thrust peaks during the heaving oscillation cycle. In the same manner as Quinn et al. (2014b), the experimental setup used in the present study joins the recent flourishing literature on robotic models using elasticity to mimic fish-like swimming kinematics through a passive mechanism Alben et al. (2012); Ramananarivo et al. (2013); Dewey et al. (2013); Raspa et al. (2014).

Working with a flexible foil forced by a pitching oscillation at one extremity and allowed to self-propel freely along a rectilinear trajectory, we focus in the present paper on the effect of swimming near a solid boundary. We examine in particular the cases excited by large amplitude pitching oscillations of the head of the swimmer, which develop large deformations of the flexible body, a regime that has not been explored up to now. Although we focus here in the cruising regimes of our artificial swimmer, the dynamics of this type of large amplitude undulation influenced by a boundary are certainly a crucial issue for natural or bio-inspired systems on a broader spectrum of swimming regimes, such as the fast-start of fish near a wall Eaton and Emberley (1991); Mirjany et al. (2011). We show that the presence of the wall produces an enhancement of the swimming performance in the large amplitude undulation cases, mainly through a favourable redistribution of momentum in the wake. This effect in terms of cruising velocity can give en enhancement of up to 25% and defines an optimal position of the swimmer trajectory parallel to the wall at around 0.4 times the characteristic size of the foil used in the present experiments.

2.7 APPLICATIONS TO PROPULSION

Engineering systems such as AUVs have been under development since the decade of the 1960s. They are widely used in oceanographic research, marine structures inspection, hydrographic profiling, sea floor cartography, water quality examination, etc. Their propulsion system is crucial for their performance and autonomy, therefore efficiency is a must. In the last decades, one of the ways sought by researchers in order to optimise propulsion systems, is through the science of biomimetics, which consists of studying nature's solutions for design inspiration. Nature is characterised by a wide diversity of swimming functions. Swimming modes can be found for specialised behaviours such as prey capturing, overcoming high currents, cruising long distances, etc. These specialisations are the result of evolution.

This section describes examples of AUVs, where the biomimetic propulsion have been applied to date.

Robotuna

In order to develop a better system of propulsion for AUVs, the *Robotuna* project started at MIT[9] in 1993. Thunniform mode is considered a culminating point of the evolution of swimming designs and tuna was selected as model for its speed (74 km/h) and its acceleration. They wanted to find out, how a fish can reach such speeds. As you can see in figure 2.12, *Robotuna* is suspended by a mast, which is used to pass the cables which connect the robot to the controllers. It is managing in real time eight vertebrae and a system of cables which is used to control tendons and muscles.

9 Massachusetts Institute of Technology

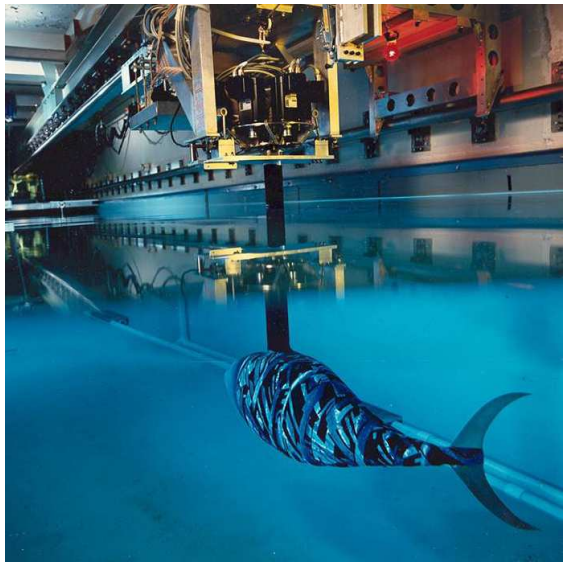

Figure 2.12: Robotuna, (Photo: Michael Triantafyllou, Massachusetts Institute of Technology).

RoboPike

Another example of a robotic fish designed at MIT was *RoboPike*. The researchers were very interested in the fulgurating accelerations of this fish. Unlike *Robotuna*, *RoboPike* can swim freely and is not sustained by a system of pulleys. *RoboPike* is controlled by a computer which interprets the orders and returns the signals appropriate to each engine. *RoboPike* equips an exosquelette in the shape of spring with spiral and can swim rather well with 81 cm of length.

Proteus

Proteus, as the penguin boat is dubbed, uses rigid flippers instead of propellers. The flippers create less turbulence than propellers, so more of their energy goes into pushing the boat forward. The new propulsion system achieved up to 87% efficiency and the average efficiency of existing ships is at or below about 70%. In spite of this efficiency, the cost, actuation and technical complexity have prevented the application of the penguin propulsors into ships.

Fish Robot at the National Maritime Research Institute

NMRI[10] in Japan studies the optimization of swimming methods and develops intelligent marine robots. They have developed more than 10 Fish Robots (series PF and series PPF) with a view to apply, in the future, the capacities of fish to our ships and submarines. The PPF-08i (see fig.2.13) was designed under the following concepts: (1) simple structure, (2) small size, (3) high turning performance, (4) controlled by a microcomputer and (5) a basic model of the group robots. The weight is over 50 gr and needed a swimming float. The maximum speed is about 0.12 m/s, and the minimum turning diameter is about 200 mm. They are considered to perform well for a fish still wearing a life ring.

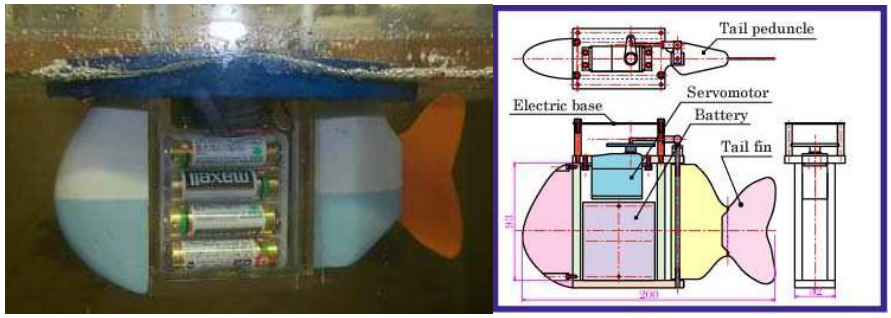

Figure 2.13: Model Fish Robot, PPF-08i.

Subsea Glider with Fin Ray Effect

Evologics[11] showed a surprising biomechanical effect of ray's fins. The biomimetic design (see fig.2.14) under patent manages shape-adaptive wing profiles and flow control devices. The robot is equipped with high-technology sensors and can mimic some propulsion modes such as:

- Active life-like wing propulsion and level gliding - provide fast and efficient motions with extraordinary maneuverability.

10 National Maritime Research Institute
11 spin-off of the Technical University Berlin

- Semi-passive buoyancy-driven gliding with 3D shape adjustments maintaining the maneuverability - energy efficient vertical scanning and long distance travelling.
- Hydro-jet propulsion - precise control of the flight trajectory maintaining accurate flight levels without body oscillations - suitable for precise sonar measurements, sea-floor mapping and add-on speed requirements.

Figure 2.14: Subsea Glider with Fin Ray Effect.

Jessiko

Jessiko is an autonomous robot fish (fig.2.15) developed by French start-up Robotswim. Jessiko is one of the smallest robot fish in the world (22cm/150g). The Jessiko project was launched in 2005 and the current version is a blend of patented technologies. Five versions of prototypes have been developed (V0 to V5). The industrial version (V5) started in 2012 and incorporates: (1) flexible flapping caudal fin provokes a velocity above 0.2 m/s (2) buoyancy dorsal fin to move up and down (3) relative position with homing chip (4) front fin to orient the trajectory upward or downward and/or reverse motion (5) optical reflection to detect walls and objects (6) two microcontrollers to follow trajectories and react to the environment (7) two lateral fins to get stability and balance (8) autonomy for hours.

Figure 2.15: Jessiko from Robotswim.

3

FLAPPING PROPULSION WITH RIGID AND FLEXIBLE FOILS

The third chapter of the manuscript is focused on the experimental systems and techniques used throughout the thesis as well as the results of rigid and flexible foils. This chapter starts with the experimental setup "towing tank", completed in the *Fluid Mechanics Laboratory* of the *Department of Mechanical Engineering* at the *Rovira i Virgili* University. Initial results are presented as a technical publication with the tittle of *"Hydrodynamics Forces and DPIV in Pitching Foils"* under reference of FEDSM2014-21465 (Proceedings of ASME 30th International Conference on Fluids Engineering Division Summer Meeting, ASME FEDSM, 2014, Chicago, IL, USA). After the initial results two papers are presented. The first one has been submitted as a publication with the tittle of *"Hydrodynamics of a rigid pitching foil in a uniform current"*. The chapter ends with the second one, which analyzed the effect of the flexibility in flapping propulsion, this work is under preparation.

3.1 EXPERIMENTAL SYSTEM AND TECHNIQUES, TOWING TANK

3.1.1 *Flow facility - towing tank*

Most of the experiments were conducted in a towing tank in the *Fluid Mechanics Laboratory* of the *Department of Mechanical Engineering* at the *Rovira i Virgili* University.

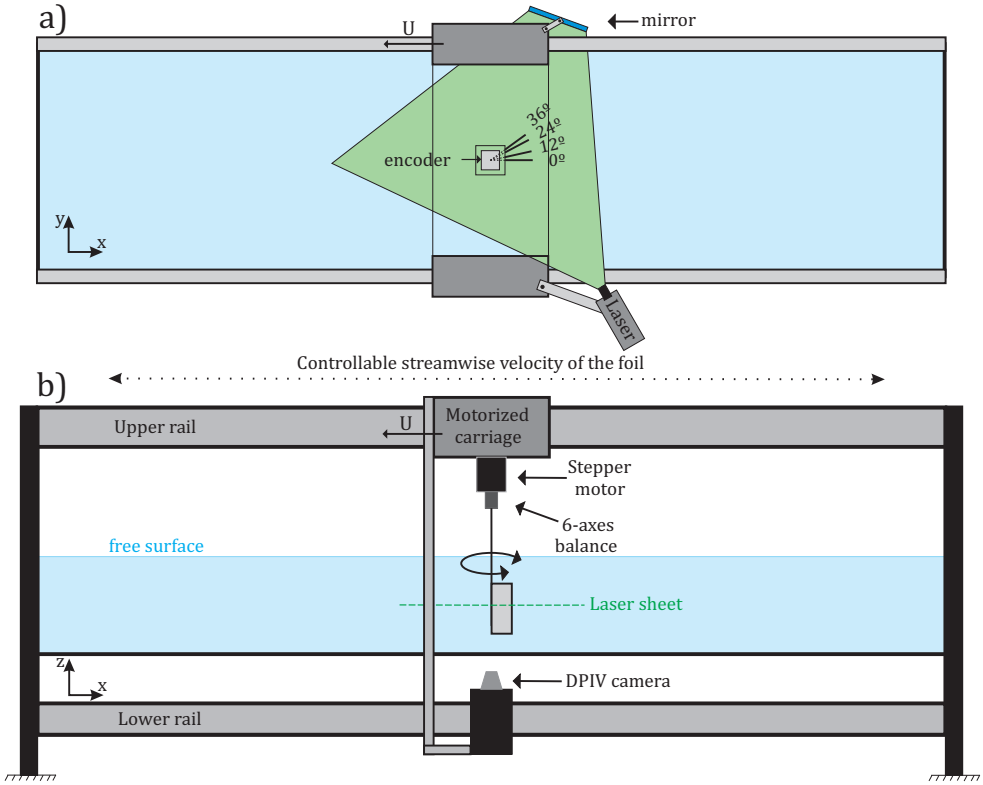

Figure 3.1: a) Experimental set up top view. b) Side view of the experimental set up.

The towing tank is 2 m long with a square section of dimensions 0.6 $\times$ 0.6 m^2 (fig. 3.1). It is equipped with a towing carriage that can move along a two-rail system (fig. 3.1b). The towing carriage is driven by a geared electric motor (motorized carriage) that could be controlled in order to produce the desired towing speeds (U). A rotary potentiometer (accuracy of $\approx$ 1mm) installed in the shaft of the electric motor, allowed closed loop control of the position of the carriage (figure 3.1).

A towing tank is a useful facility in hydrodynamic research to study the effects of water moving past objects. Many techniques can be applied in this facility such as optical measurement, flow visualizations or measurements based on doppler effect[1]. In figures 3.2 and 3.3, you can

1 flow visualizations are used to make the flow patterns visible, providing a brilliant observation of the complex flows. Optical techniques like DPIV and DDPIV are used to

find examples of flow visualization and DPIV, which have been done in the towing tank.

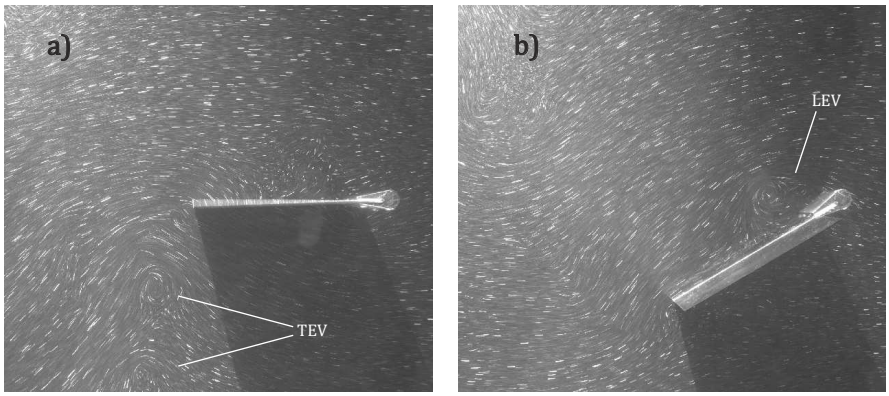

Figure 3.2: Flow visualizations with long exposure, a) trailing edge vortex and b) leading edge vortex.

At the beginning of the research, velocities of carriage of the towing tank was calibrated using DPIV. In order to test the reliability of the facilities, more than 12 velocity profiles of the motorized carriage (from 3 to 50cm/s) were compared with the velocity fields obtained with DPIV, resulting in a small dispersion in the velocity of less than 0.2 cm/s. Two trials with U_1=20cm/s and U_2=40cm/s are shown in figure3.3 indicating a good agreement between the velocity profile from the motorized carriage with the optical measurements from DPIV, which show uniform fields.

obtain instantaneous two-dimensional or three-dimensional velocity fields. Measurements based on doppler effect like LDA provides velocity at an exact spatial point.

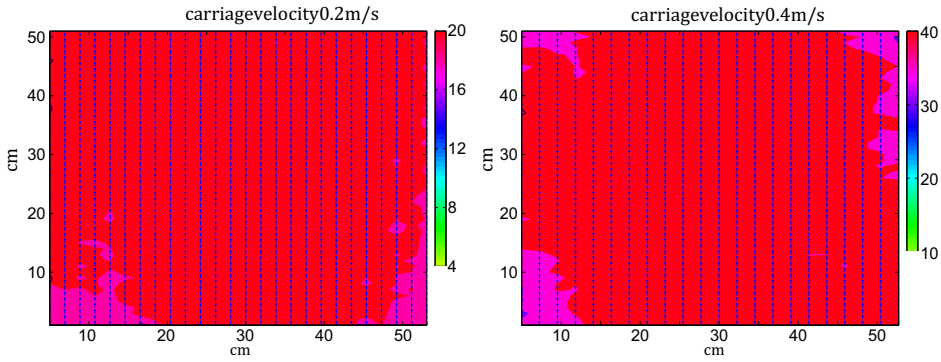

Figure 3.3: Velocity trials to compare carriage velocity with DPIV velocity, a) 0.2m/s b) 0.4m/s.

3.1.2 *Apparatus - towing tank*

The apparatus was set up on the towing carriage and consisted of a series of devices (fig.3.4), where the flapping oscillation was created and all the forces, moments and motions were measured.

At the bottom of the apparatus the different foils were installed. The mean vertical position of the foils was 15 cm below the water surface and 15 cm above the floor of the tank. The foils were made from a stainless steel (E=210 GPa) sheet, 120 mm in length (chord - c) and 200 mm in height (span - s). The aspect ratio (s/c) was 1.67, chosen high enough to avoid strong three-dimensional effects as commented by Buchholz and Smits (2008). The foil was clamped to a stainless steel shaft of external diameter 8 mm, by means of a specially designed coupling. The coupling was streamlined and also made of stainless steel. See figure 3.4 for details.

The dynamic flapping motion was achieved using a stepper motor controlled by computer software that permitted the setting of different pitch profiles. This motor had an encoder embedded in it, which was used to measure the angular position of the shaft. The encoder provided a resolution of 1000 number of pulses per revolution. The upper end of the shaft was coupled to a six-axes load cell, that allowed the measure-

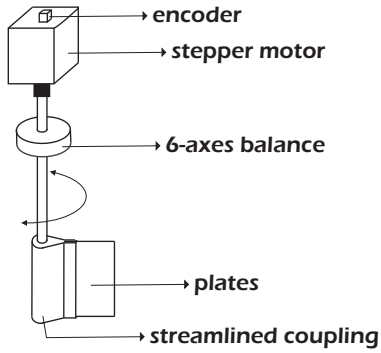

Figure 3.4: Different elements of the apparatus.

ment of hydrodynamic forces and moments (F_x, F_y, F_z, M_x, M_y and M_z). Technical specifications of the six-axis load cell were:

- F_x and F_y: Standard measurement range (N): ± 100. Digital resolution (N): 0.013
- M_z: Standard measurement range (Nm): ± 12. Digital resolution (Nm): 0.0015

We tested the six-axes load cell with the objective of checking the accuracy of its calibration. Figure 3.5 shows the measurements performed.

3.1.3 *Kinematics - towing tank*

The experiments were conducted with a simple sinusoidal harmonics equation:

$$\theta(t) = \theta_0 \, sin \, (2\pi f t), \tag{3.1}$$

where f is the flapping frequency of the oscillation and θ_0 is the swept angle of the pitch motion.

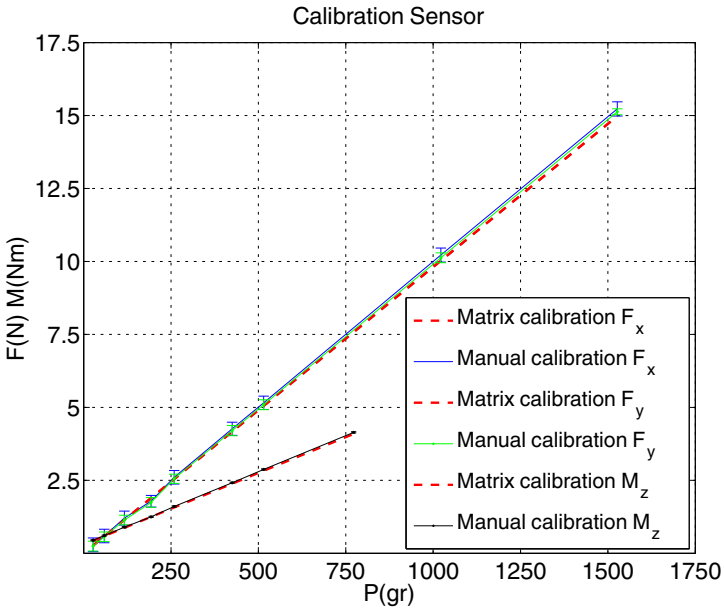

Figure 3.5: Calibration sensor F_x, F_y and M_z.

3.1.4 *The physical parameters - towing tank*

The parameter space explored in the towing tank was 660 experimental cases summarised in table 3.1. Strouhal number (St) was defined as $\frac{fA}{U}$ (A is the peak to peak excursion of the trailing edge). Reynolds numbers ($\frac{Uc}{\nu}$) up to 9250 were achieved during the experiments. U is the towing speed of the carriage, varied in the range from 4 to 8 cm/s and ν is the kinematic viscosity of the fluid.

- Strouhal number. $St = \frac{fA}{U}$=$[0.1 - 0.9]$ where A is the wake width (often approximated by peak to peak excursion of the trailing edge, which is the convention used here), f is cyclic frequency in Hertz.

- Swept angles. θ_0=[24 °, 56 °, 72 °]

- Reynolds number: $R_c = \frac{Uc}{\nu}$, towing speed U=[0.04-0.08] m/s, ν = is the kinematic viscosity of the water at laboratory temperature

and c is the chord.

- Aspect ratio. Span=200 mm. Chord=120 mm AR=1.67

- Rigidity and flexural stiffness is defined by p_h. Four flexural stiffness were studied, r rigid, $s-r$ semi-rigid, $s-f$ semi-flexible and f flexible.

Table 3.1: Parameters of the experiment.

Parameters				cases
Span	s	200	mm	-
Chord	c	120	mm	-
Aspect ratio	s/c	1.67	-	-
Flapping frequency	f	0.2 - 1.2	Hz	-
theoretical Amplitude	A	4.7, 10.8, 13.5	cm	
Towing speeds	U	5.5 - 7.7	cm s^{-1}	-
Swept angles	θ_0	24, 56, 72	degrees	3
Reynolds numbers	Re	6600 - 9250		5
Strouhal numbers	St	0.1 - 0.9		11
Plates		$r, s-r, s-f, f$		4
Trials				660

3.1.5 *Deformable plate and stiffness - towing tank*

To analyze the effect of stiffness on hydrodynamic forces, different values of flexural stiffness EI were investigated, where E is Young's modulus and I is the second moment of area. Values of EI varied widely from the range of rigid until very flexible, as you can see in the table 3.2. All the plates had a constant chord and span, c = 12 cm and s = 20 cm

respectively and the flexural stiffness was varied with the thickness of the foils.

Note that the foils were flexible only at the chordwise direction and not on the spanwise direction due to streamlined coupling which allowed a very rigid link at the leading edge of the plates (see fig.3.4). Therefore, it was assumed one-dimensional deformation of a beam type where the Poisson ratio can be neglected at the flexural stiffness ($EI = Eh^3/12$), the same simplification was reported by Kim and Gharib (2011b). A non-dimensional parameter was defined to characterize the problem for the dynamical interaction of the deformable foils with the surrounding fluid.

$$p_h = \frac{EI}{\rho U^2 c^3} \tag{3.2}$$

Table 3.2: Different flexibilities.

model name	h (mm)	EI (N/m^2)	p_h
rigid (r)	0.4	1.12	214.26
			174.76
			148.79
			132.28
			109.32
semi-rigid ($s-r$)	0.15	5.9e-2	11.30
			9.22
			7.85
			6.87
			5.76
semi-flexible ($s-f$)	0.1	1.75e-2	3.35
			2.73
			2.32
			2.07
			1.71
flexible (f)	0.075	7.4e-3	1.41
			1.15
			0.98
			0.87
			0.72

3.1.6 *Hydrodynamic coefficients - towing tank*

All the forces and moments applied to the plate were acquired with the multi-axis load cell with a sampled at a frequency of 5 kHz. A low-pass filter was used to remove the ambient electrical noise after the acquisition. Forces and moments were rotated from the pitch reference system into the carriage reference system. Forces $\overline{F}$ and moments $\overline{M}$ can be rotated by multiplying by the pitch rotation matrix $\overline{R_\theta}$:

$$\overline{R_\theta} = \begin{vmatrix} cos\theta & -sin\theta & 0 \\ sin\theta & cos\theta & 0 \\ 0 & 0 & 1 \end{vmatrix} \tag{3.3}$$

$$\overline{F_p} = [F_{xp} F_{yp} F_{zp}] = \overline{R_\theta F} \tag{3.4}$$

$$\overline{M_p} = [M_{xp} M_{yp} M_{zp}] = \overline{R_\theta M} \tag{3.5}$$

The force F_{xp} is the thrust (or drag) on the foil. Average value of $F_{xp}(t)$ is $\overline{F_{xp}}$ and is given by the following equation:

$$\overline{F_{xp}} = \frac{1}{nT} \int_0^{nT} F_{xp}(t)\, dt, \tag{3.6}$$

The mean thrust coefficient is defined as follows:

$$C_T = \frac{\overline{F_{xp}}}{\frac{1}{2}\rho U^2 cs} \tag{3.7}$$

The input power coefficient is given by:

$$C_P = \frac{\overline{P}}{\frac{1}{2}\rho U^3 cs} \tag{3.8}$$

where the average input power per cycle $\overline{P}$ can be obtained by:

$$\overline{P} = \frac{1}{nT} \int_0^{nT} M_{zp}(t)\theta'(t)\, dt \tag{3.9}$$

where T, n and ρ are the period of the oscillatory motion, number of the oscillating periods and the density of the fluid, respectively. Then, the Froude hydrodynamic propulsive efficiency is defined as a ratio of the useful power to the input power, and can be calculated as:

$$\eta = \frac{C_T}{C_P} = \frac{\overline{F_{xp}} U}{\overline{P}} \tag{3.10}$$

3.1.7 *Quantitative flow imaging, DPIV - towing tank*

In order to investigate flow patterns around the oscillating foil, digital particle image velocimetry (DPIV) was performed to obtain two dimensional velocity fields for selected planes. The water in the tank was seeded with Hollow Glass Spheres of 10 μm in diameter. Particles were illuminated with a Continuous Wave 3 Watt Diode-Pumped Solid State green laser (532 nm), that produced a planar laser sheet. The light scattered by the tracer particles was captured by a CMOS sensor based digital camera with 4.0 MPixel (2048 x 2048) resolution. The camera was equipped with optics of focal length 20 mm. It was placed below the towing tank directed upwards, mounted on the towing carriage and moving solidary with the apparatus. The field of view covered more than 300 mm in the streamwise direction and 150 mm in the transverse one ($2.5c \times 1.25c$). The Cartesian system of reference defined has its origin in the axis of the shaft at the mid span of the foil, with x along the streamwise direction, y transversely and z coincident with that of the shaft. Details of the set-up are depicted in figure 3.1.

A trigger signal was generated using a data acquisition system controlled from a computer. This signal was used to initiate the towing carriage motion, the flapping motion, the DPIV camera acquisition and the data acquisition system (6-axes load cell, encoder, potentiometer and camera strobe). The data acquisition system sampled 9 channels at 5 kHz. The strobe output of the camera was recorded so the time series of each signal could be related to the DPIV imaging. A total of 1600 images were recorded during each experiment at a rate of 224 frames per second. The exposure time of the CMOS sensor was configured at 1.2 ms, after a trial and error process. This system allowed us to obtain flow interrogations every 4.46 ms.

Image processing was done with an in-house DPIV code. Before the velocity fields were computed, the shape of the foil in each image was removed by applying a mask. Two dimensional velocity fields were computed by applying a Fast Fourier Transform (FFT) based multipass window-deformation cross-correlation technique (Willert and Gharib (1991)). The algorithm evaluated the images in two steps, first with an interro-

gation area of 64 x 64 pixels and later with an area of 32 x 32 pixels and a 50% overlap. Spurious vectors were removed and substituted by averaging around their position.

3.1.8 *System diagram - towing tank*

The system diagram is a scheme that represents the actors outside a system that interact with that system (fig.3.6). The system diagram shows in entirely its inputs and outputs from/to devices or external factors.

This system diagram is grounded in a process which is able to do synchronization experiments between variable loads and DPIV.

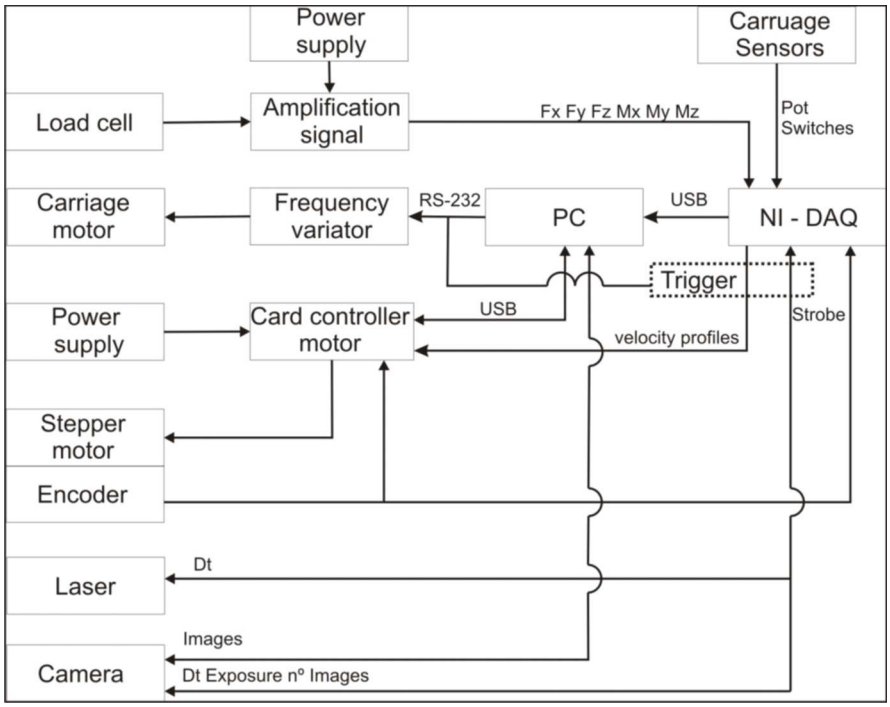

Figure 3.6: System diagram of the experiment.

3.2 INITIAL RESULTS IN THE TOWING TANK

The initial results in this section were presented as a technical publication with the tittle of *"Hydrodynamics Forces and DPIV in Pitching Foils"* under reference of FEDSM2014-21465. Proceedings of ASME 30th International Conference on Fluids Engineering Division Summer Meeting, ASME FEDSM, 2014, Chicago, IL, USA. Abstract, introduction and experimental setup of this technical publication have been omitted because these parts have been already explained that the previous sections and chapters more extensively. In this way this section will be focused in the results of the manuscript[2].

3.2.1 *Quantitative Flow Imaging results*

Figure 3.7 shows phase averaged dimensionless vorticity fields at four different locations along the length of the foil. Vorticity has been non-dimensionalised with the chord and the towing speed ($w_z c/U$). The dimensionless distance between each DPIV plane along the span is $0.15s$ and they cover the lower half of the foil. The figures 3.7 shown the results of experiments conducted with a Strouhal number of 0.2 and Reynolds number of 16200.

2 It should be mentioned that the some preliminary experiments were carried out with higher towing speed than the towing speed reported in the section 3.1.4. Thus higher Reynolds numbers are presented in this section.

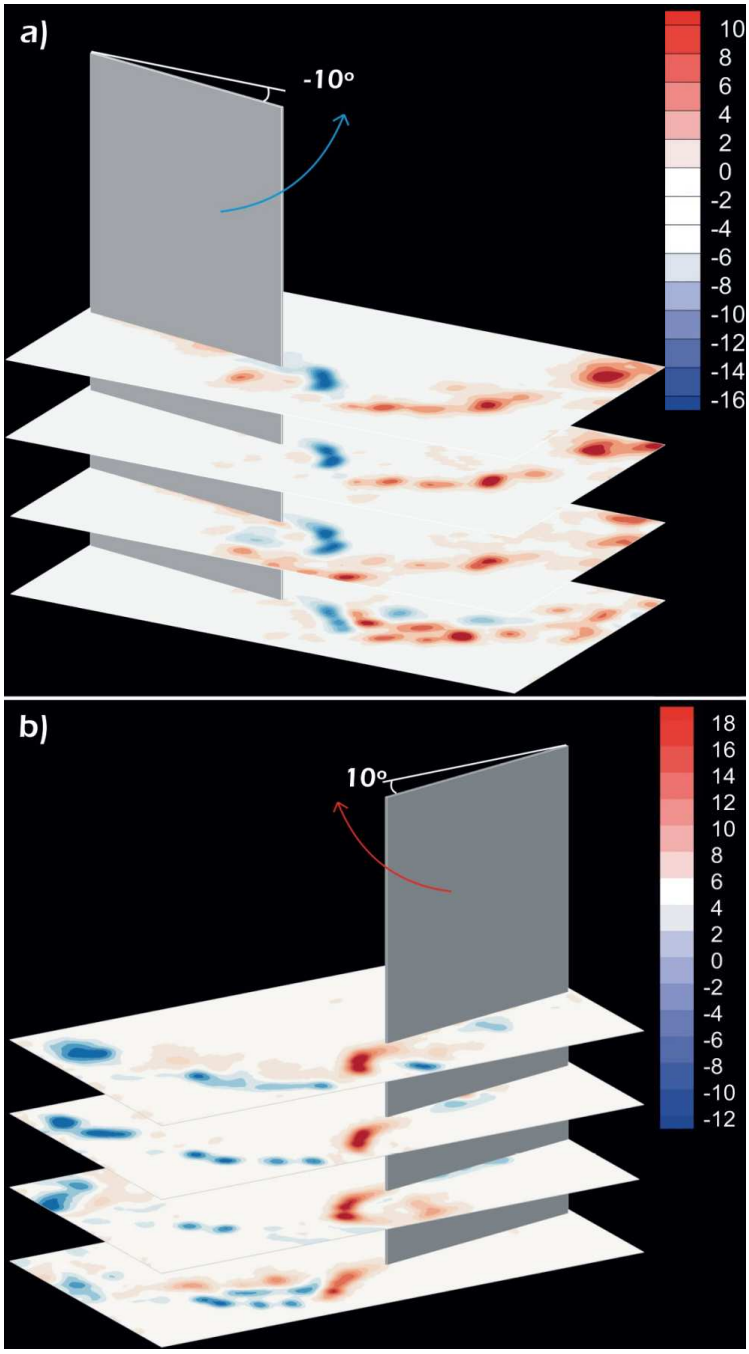

Figure 3.7: DPIV planes along the length of the foil for experiments with St=0.2 and Re=16200. a) θ=−10° upstroke b) θ=10° downstroke.

Fig. 3.7 show a symmetric position of the foil at 10 and -10 degrees, during the upstroke and the downstroke parts of the pitch cycle. The upper three planes show highly correlated vortex shedding from the trailing edge, whilst the lower planes denote the effect of the leading edge vortices. In figure 3.8, the same arrangement of plots is presented, but now for cases with a Strouhal number of 0.38 and a Reynolds number of 16200. The phase averaging in this case was done at 20 and -20 degrees. Vortex strength is considerably higher and two vortices are shed at the trailing edge instead of the single one in figure 3.7. Again, the upper three planes show highly correlated vortices in the trailing edge, whilst the lower planes denote the effect of the leading edge.

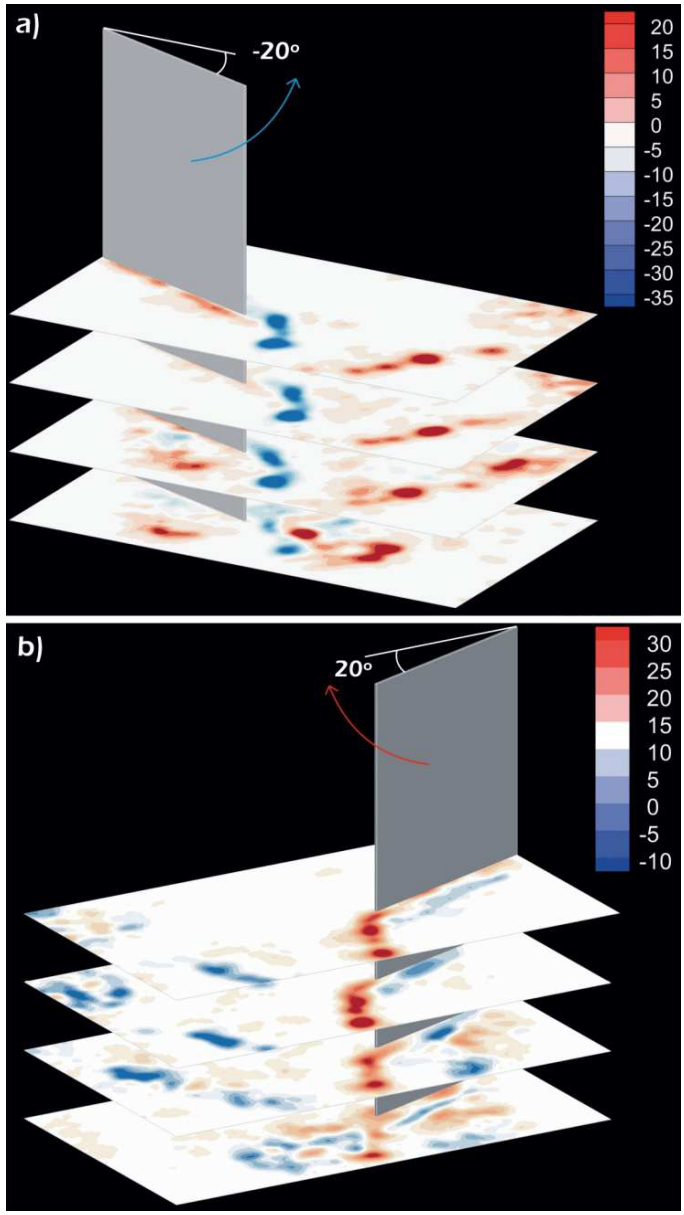

Figure 3.8: DPIV planes along the length of the foil for experiments with St=0.38 and Re=16200. a) θ=-20° upstroke b) θ=20° downstroke.

Long exposure images were also taken during the experiments. Figure3.9 confirm the observations made with the DPIV. In each snapshot, vortices are identified with dotted circumferences. Red is used for anti-clockwise vorticity and blue for clockwise. Depending on the Strouhal number, the number of vortices shed at each side of the wake is one or two, indicating the appearance of the reverse Bénar d-von Kármán wake, as found in Anderson et al. (1998); Buchholz and Smits (2008); Godoy-Diana et al. (2008); Schnipper et al. (2009). In figure 3.10 the DPIV results of velocity fields are plotted together with streamlines and vorticity for the same case as in figures 3.8 and 3.9 (c and d).

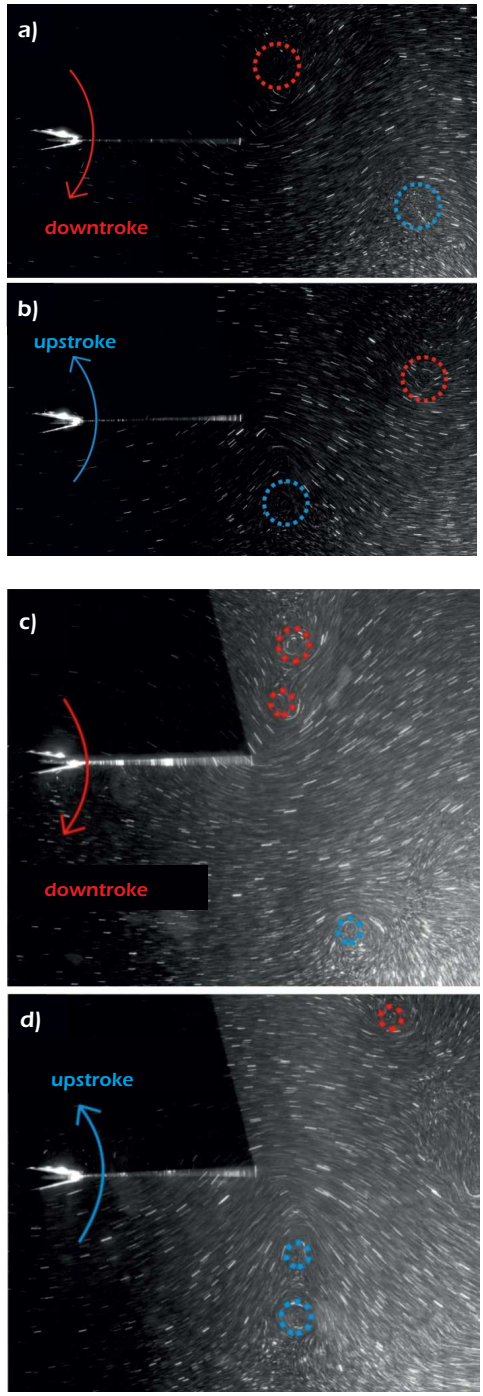

Figure 3.9: Flow visualization showing two vortices for cycle (2S) for a case with St=0.26 and Re=16200, a) downstroke b) upstroke. Four vortices for cycle (2P) for a case with St=0.38 and Re=16200, c) downstroke d) upstroke.

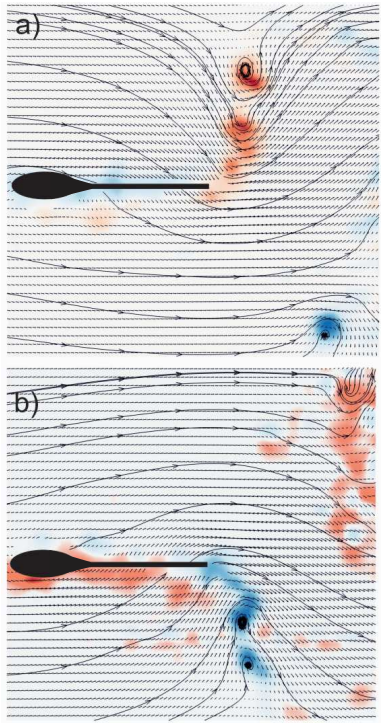

Figure 3.10: Vorticity fields, streamlines and velocity vectors a) downstroke, b) upstroke, both cases for St=0.38 and Re=16200.

3.2.2 *Results: Rigid vs. Flexible Foil*

The ratio of the bending forces on the foil to the inertial forces of the fluid can be expressed in dimensionless form with the expression,

$$p_h = \frac{EI}{\rho_f U^2 s^3}, \tag{3.11}$$

In our study, p_h was 71.4 for the rigid foil with the largest thickness, and 1.5 for the flexible one. Figures 3.11 and 3.12 show summarized results for comparison of the wake for the rigid and the flexible foil cases, respectively. Each figure is for a different experiment with a differently rigid foil. Each figure shows 4 instantaneous vorticity fields in dimensionless form.

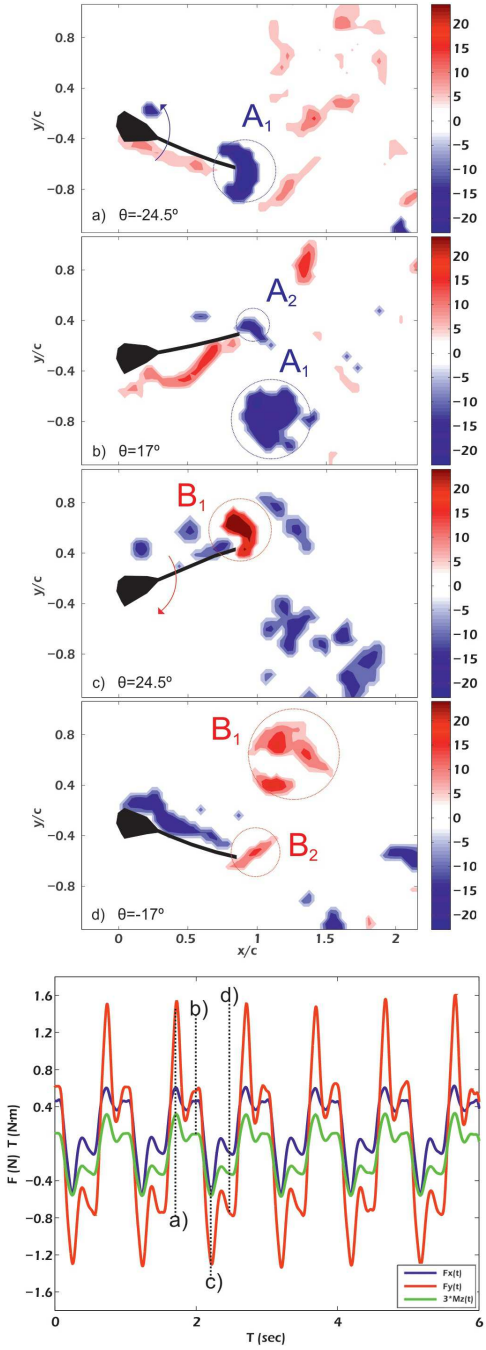

Figure 3.11: St=0.9, Re=14000, a) $\theta = -24.5^\circ$ b) $\theta = 17^\circ$ c) $\theta = 24.5^\circ$ d) $\theta = -17^\circ$.

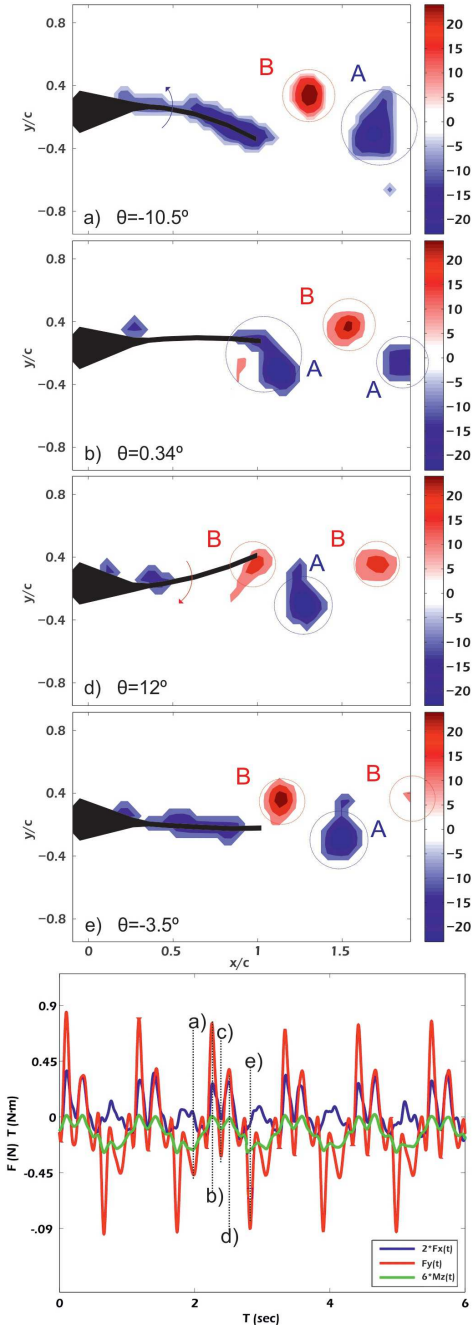

Figure 3.12: St=0.5, Re=9244, a) $\theta = -10.5\,^\circ$ b) $\theta = 0.34\,^\circ$ c) $\theta = 12.5\,^\circ$ d) $\theta = -3.5\,^\circ$.

The snapshots in the plots have been selected to explain the structures in the wake as well as the loads associated to those. The DPIV planes in each plot are located at the mid span of the foil and the plot at the bottom of each figure shows the time series of the hydrodynamic loads acting on the foil: Forces $F_x(t)$ and $F_y(t)$ and the pitching moment $M_z(t)$.

In figure 3.11 with the results of the rigid foil, $M_z(t)$ appears multiplied by a factor of 3 for clearness. $F_x(t)$ represents the net force in the direction of the thrust and $F_y(t)$ represents the net force in the transverse direction. $M_z(t)$ is the net moment about the pitch axis. From the vorticity fields in figure 3.11, there are two vortices denoted as A_1 and B_1 that correspond to instants a) and c). In addition there are two secondary vortices denoted with A_2 and B_2 at times b) and d). Vorticity fields corresponding to a) and c) are almost symmetric and related to the peaks of the loads. Instant a) is for the maximum and c) for the minimum loads. These instants in time can be clearly associated to the shedding of vortices A_1 and B_1. Notice that in the load plot, the only non symmetrical signal is F_x, indicating that the net force in the x direction has a mean value. This value gives us the mean net force in the direction of thrust. The load signals have secondary peaks of smaller value which can be related to the secondary vortices A_2 and B_2, therefore indicating the shedding of two pairs of vortices per cycle.

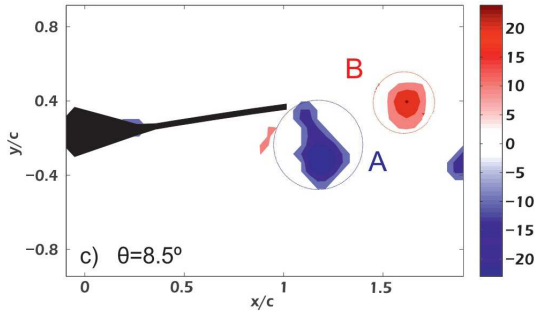

Figure 3.13: St=0.5, Re=9244, c) $\theta = 12\,^{\circ}$.

In figure 3.12 results are presented for the flexible foil. In this case F_x has been multiplied by 2 and M_z by 6 again for the sake of clarity. By looking the vorticity fields obvious differences appear in the wake. In

this case only a single vortex is shed at each side of the wake, yielding to vortices A and B. Even though the wake appears to be more organised than in the previous case, loads are considerably more complicated. As one of the vortices is being shed from the trailing edge, loads experience a series of consecutive peaks. Instant a) is for vorticity generation along the chord in the upstroke. Then at instant b) vortex A is about to be shed showing a loading peak. At instant c) the loading falls down as vortex A is already downstream the trailing edge. The vorticity plot corresponding to instant c) appears in a separated figure 3.13. Finally at instant d) we have the starting of the downstroke.

3.2.3 *Conclusion*

The propulsion characteristics of flapping foils in pitch motion, has been investigated experimentally. Two different flexural stiffness, and a wide range of Reynolds and Strouhal numbers have been used for the purpose. The flow dynamics in the wake have been studied by using DPIV and flow visualization, and those have been related to loading measurements synchronously. The manuscript presents preliminary results of a large study being now conducted with this fully working experimental system.

For the cases shown in this manuscript, evident differences in the flow structures in the wake of the foils have been observed. For the combinations of the Strouhal and Reynolds numbers shown here, we have observed two different kinds of wake, one consisting of two pairs of vortices per cycle, and another with two single vortices per cycle. The temporal evolution of each vortex forming in the wake can be linked to specific events in the the loading signals.

3.3 HYDRODYNAMICS OF A RIGID PITCHING FOIL

The results in this section have been submitted as publication with the tittle of *"Hydrodynamics of a rigid pitching foil in a uniform current"*.

3.3.1 *abstract*

Experiments have been carried out with a rigid pitching foil towed in a still water tank, allowing to simulate a wide variety of situations in which a bio-inspired robotic system or a live fish would be involved.

The study reveals what are the best kinematics in terms of efficiency and thrust production for a simplified system such as the one presented here. Hydrodynamic forces and moments allowed the computation of efficiencies, and the wake was quantified using Digital Particle Image Velocimetry. The momentum distribution in the wake of the foil has allowed the physical explanation for the cases with highest thrust production capacity.

3.3.2 *Introduction*

Engineering systems such as Autonomous Underwater Vehicle (AUVs) have been under development since the decade of the sixties. They are widely used in oceanographic research, marine structures inspection, water quality inspection, etc. Their propulsion system is crucial for their performance and autonomy, therefore efficiency is a must. In the last decades, one of the ways sought by researchers in order to optimise propulsion systems, is through the science of biomimetics, which consists in studying nature's solutions for design inspiration. Nature is characterised by a wide diversity of swimming functions. Swimming modes can be found for specialised behaviours such as prey capturing, overcoming high currents, long cruising distances, etc. This specialisation is the result of evolution.

In the early 90s Triantafyllou et al. (1993) proposed the use of the Strouhal number (St), defined as the ratio between the tip speed of the foil to the free stream velocity, as an important dimensionless parameter to characterise thrust production achieved by flapping foils. He found that when in the range from 0.25 to 0.35, propulsion was maximised. At similar Strouhal numbers Anderson et al. (1998), in an experiment with an airfoil undergoing pitch and heave motions, showed efficiencies up to 87% at a Reynolds number (Re) of 40000. Hover et al. (2004) conducted experiments with a foil in pitch and heave motion to study propulsion, depending on the angle of attack profile used, finding efficiencies over 60% when the profile was sinusoidal. Read et al. (2003) with the same set-up in the towing tank studied effective ways of manoeuvring, they established the phase angle of 90 degrees between pitch and heave to produce the best thrust performance, which is widely used today.

Buchholz and Smits (2008) performed flow visualizations at Strouhal number near the expected for optimal propulsion, computing efficiencies and visualising the wake with Digital Particle Image Velocimetry (DPIV), using rigid low aspect ratio pitching foils. They found peaks of efficiency up to 21% and reported the appearance of three distinct three-dimensional wakes. Green et al. (2011) used DPIV and flow visualization at different locations along a trapezoidal pitching panel, and also computed Lagrangian Coherent Structures (LCS), in order to investigate the three-dimensional wake formation process.

Taylor et al. (2003) compiled Strouhal numbers resulting from cruise swimming or flying, of more than 40 species, showing ranges previously indicated by Triantafyllou et al. (1993). Focusing only in swimming animals, Eloy (2012) grouped 53 different species to discuss the consistency of the Strouhal number in a slightly larger range. Experiments with live fish have revealed structures not reported before in simplified experiments, as those were though to isolate factors such as form, flexibility, flow control mechanisms, etc. very common in nature. For example, in Drucker and Lauder (1999), the authors quantify locomotor forces with DPIV and estimate the momentum transferred to the wake. They were also able to visualise a roughly symmetrical wake made of vortex rings with a central jet of high velocity after the downstroke or upstroke. In

Drucker and Lauder (2000) the authors compared the performance of two labriform swimmers at different range of speeds, also quatifying their wakes using DPIV. They discuss how the momentum transfer in the wake is greatly affected by the ratio lateral to downstream force generated by the fish. Wilga and Lauder (2004) revealed ring-within-a-ring vortex (dual vortices) structure when studying the wake of a shark.

Other authors have focused on the relationship between vortex formation timing and thrust generation in drag-based paddling propulsion systems (Kim and Gharib, 2011a), after studying vortex formation timings in translating plates (Kim and Gharib, 2011b), using Defocusing Digital Particle Velocimetry (DDPIV). They propose vortex formation timing as the key parameter to understand flapping propulsion.

In the current work we use a simplified robotic model made of a rectangular rigid foil in which pitch can be controlled. The experiment is thought to study the effect of the pitch kinematics imposed to the foil, on this canonical swimmer when affected by a uniform current. The set-up allows to simulate a wide variety of situations by combining flow speed and the foil kinematics. Hydrodynamic loads acting on the system have been acquired synchronously with DPIV interrogations in the wake of the foil, allowing the computation of propulsion and power coefficients, besides efficiency. Those can be easily linked to the DPIV vorticity and velocity fields in the wake of the robotic system.

3.3.3 *Experimental methods*

3.3.3.1 *Towing tank set-up*

Experiments were conducted in a towing tank 2 m long with a square section of dimensions 0.6×0.6 m^2. The water tank was equipped with a towing carriage that can move along a two-rail system (fig. 3.20a). The towing carriage was driven by a geared electric motor that could be controlled in order to produce the desired towing speeds (U). A rotary potentiometer installed in the shaft of the motor, allowed closed loop control of position (figure 3.20a).

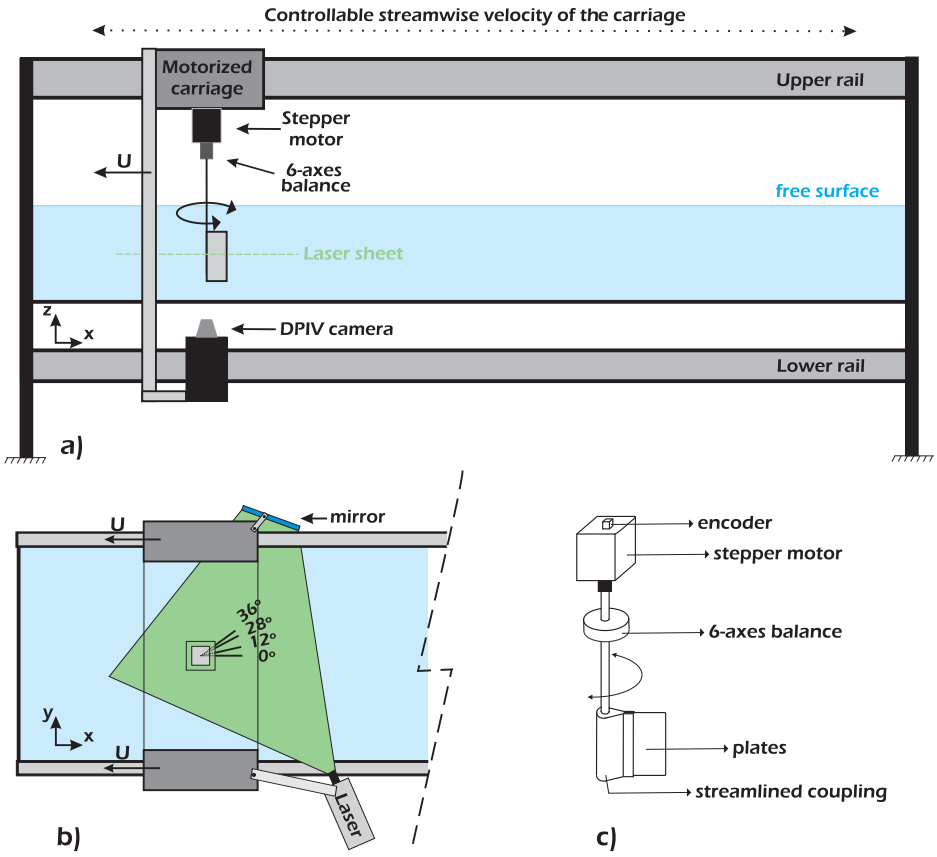

Figure 3.14: a) Side view of the experimental set up. b) Top view of the experimental set up. c) Apparatus.

The foil was made of a stainless steel (E=210 GPa) sheet 0.4 mm thick, 120 mm wide (chord - c) and 200 mm high (span - s). This large thickness was chosen to avoid any foil deformation during the experiments, so it can be considered infinitely rigid. The aspect ratio (s/c) was 1.67, chosen high enough to avoid strong three-dimensional effects (Buchholz and Smits, 2008). The foil was clamped to a stainless shaft of external diameter 8 mm, by means of a specially designed coupling. The coupling was streamlined and also made of stainless steel. See figure 3.20c) for details.

The upper end of the shaft was coupled to a six-axis load cell, that allowed the measurement of hydrodynamic forces and moments. The pitch flapping motion was achieved using a stepper motor controlled from a computer software that permitted setting different pitch profiles. The motor had an encoder embedded on it, which was used to measure the angular position of the shaft. The described apparatus was installed on the towing carriage, with the shaft and the foil penetrating the water free surface of the water tank. The foil ended up being at 150 mm from both the free surface and the floor of the tank. All signals coming out the load cell, the potentiometer and the encoder were sampled at a frequency of 5 kHz. An schematic of the experimental set-up appears in figure 3.20.

Sinusoidal pitch was imposed to the system to generate the flapping kinematics described by equation,

$$\theta(t) = \theta_0 \sin(2\pi f t) \tag{3.12}$$

where f is the flapping frequency and θ_0 is half the swept angle. The apparatus was towed at different towing speeds along the still water tank, whilst flapping. Hence, the parameter space consisted of variations of f, θ_0 and U. Reynolds numbers ($\frac{Uc}{\nu}$) in the range from 6600 to 9250 were achieved during the experiments, varying the velocity U in the range 5.5 to 7.7 cm/s, in increments of approximately 0.5 cm/s. ν in the previous expression is the kinematic viscosity of the water at laboratory temperature. The Strouhal number (St) is defined as $\frac{fA}{U}$, where A is the peak to peak excursion of the trailing edge. A total of 165 experimental cases, each including DPIV and load measurements, were performed for this work after varying U, θ_0 and f. They appear summarised in table 3.3.

3.3.3.2 *Digital Particle Image Velocimetry (DPIV) set-up*

In order to investigate flow patterns around the oscillating foil, digital particle image velocimetry (DPIV) was performed to obtain two dimensional velocity fields for selected planes. The water in the tank was seeded with Hollow Glass Spheres of 10 μm in diameter. Particles were

Table 3.3: Parameters of the experiment

Parameters			
Span	s	200	mm
Chord	c	120	mm
Aspect ratio	s/c	1.67	-
Flapping frequency	f	0.2 - 1.2	Hz
Amplitude	A	4.7, 10.8, 13.5	cm
Swept angles	$2\theta_0$	24, 56, 72	degrees
Towing speeds	U	5.5 - 7.7	cm s^{-1}
Reynolds numbers	Re	6600 - 9250	-
Strouhal numbers	St	0.1 - 0.9	-

illuminated with a Continuous Wave 3 Watt Diode-Pumped Solid State green laser (532 nm), that produced a planar laser sheet. The light scattered by the tracer particles were captured by a CMOS sensor based digital camera with 4.0 MPixel (2048 x 2048) of resolution. It was equipped with optics of focal length 20 mm. The camera was placed below the towing tank imaging upwards, mounted on the towing carriage and moving solidary with the apparatus. The field of view covered more than 300 mm in the streamwise direction and more than 240 mm in the transverse one ($2.5c \times 2c$). Due to the lower intensity of the laser sheet illumination and the shadows introduced by the model, the DPIV processing was only applied to the region that covered the near wake and the last 12.5% of the foil's length ($1.625c \times 2c$). The Cartesian system of reference defined has its origin in the axis of the shaft at the mid span of the foil, with x along the streamwise direction, y transversely and z coincident with the of the shaft. All DPIV interrogations were made at a horizontal plane (xy) located at the middle of the foil height (z=0). Details of the set-up are depicted in fig. 3.20.

A trigger signal was generated using a data acquisition system controlled from a computer. This signal was used to initiate the towing carriage motion, the flapping motion, the DPIV camera acquisition and

the data acquisition system (6-axis load cell, encoder, potentiometer and camera strobe). As already said in the previous system, the data acquisition system sampled all 9 channels at 5 kHz. The strobe output of the camera was recorded so the time series of each signal could be related to the DPIV imaging. A total of 1600 images were recorded during each experiment at a rate of 224 frames per second. The exposure time of the CMOS sensor was configured at 1.2 ms, after a trial en error process. This system allowed us to obtain flow interrogations every 4.46 ms.

Image processing was made with an in-house DPIV code. Before the velocity fields were computed, the shape of the foil in each image was removed by applying a mask. Two dimensional velocity fields were computed by applying a Fast Fourier Transform (FFT) based multipass window-deformation cross-correlation technique (Willert and Gharib (1991)). The algorithm evaluated the images in two steps, first with an interrogation area of 64 x 64 pixels and later on with 32 x 32 and a 50% overlap. Spurious vectors were removed and substituted by averaging around their position.

3.3.4 *Results of Hydrodynamics of a rigid pitching foil*

Figure 3.15 shows the coefficients and the efficiency obtained for each experiment performed as a function of Strouhal number. Symbols are used for different *Re*. Solid blue symbols are used for the 24 degree swept angle cases, solid red symbols for the 56 degree and finally the solid green symbol is used for the 72 degree experiments.

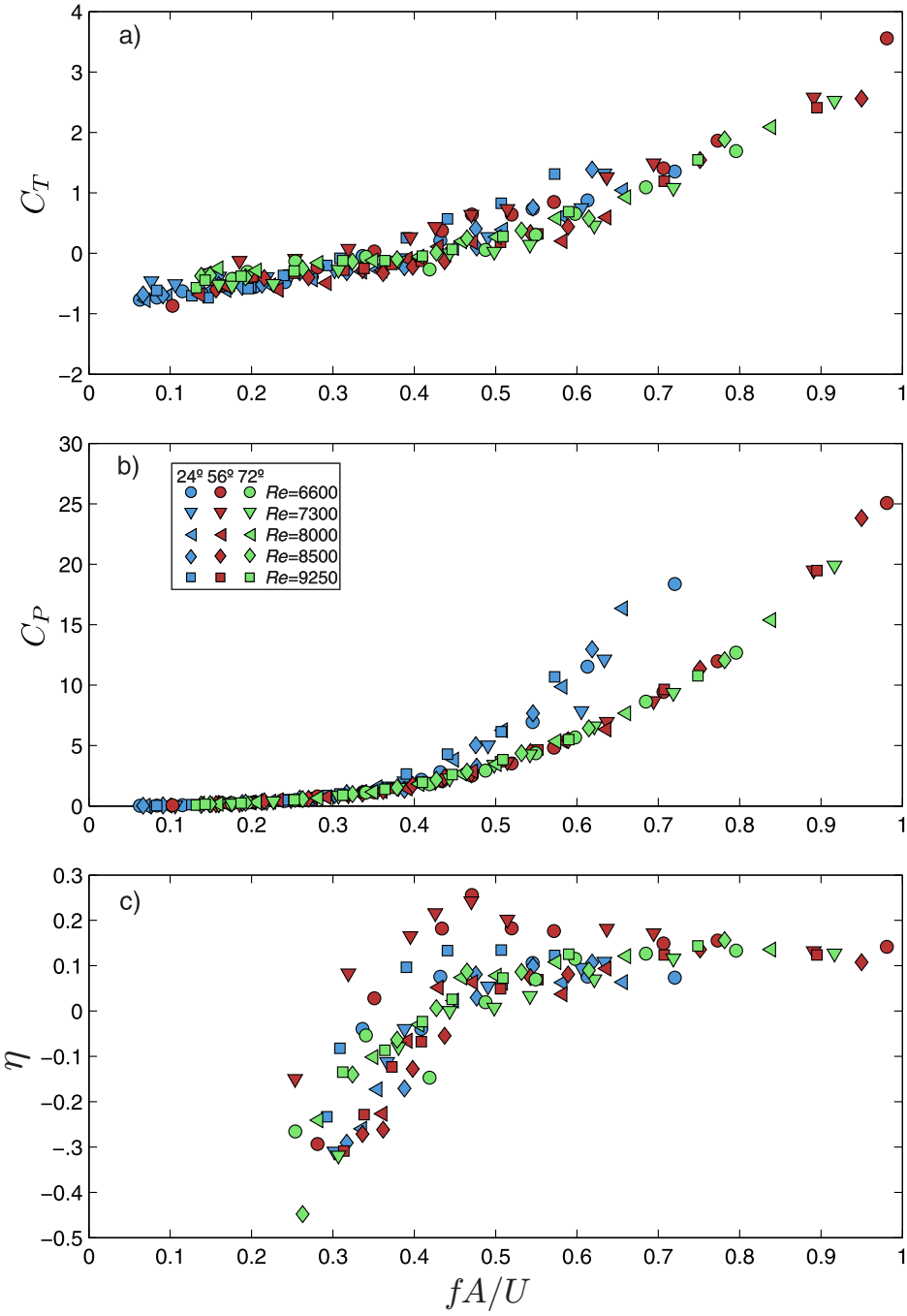

Figure 3.15: Thrust coefficient (C_T), power coefficient (C_P) and hydrodynamic efficiency (η) as a function of fA/U. Symbols are used for each different Reynolds number (Re) and colours are used for swept angle ($2\theta_0$).

In figure 3.15, C_T increased monotonically with St for all Re and θ_0 (figure 3.15a). The larger the swept angle, the smaller the rate of increase of the net thrust coefficient with Strouhal number, especially in the range $0.38 < St < 0.7$. A region with negative C_T was observed for St0.35, meaning that the foil was generating insufficient thrust to overcome the total drag. In the C_P plot (figure 3.15b), a clear quadratic trend is observed with two distinct branches to which all the points collapse independently of Re, one for the two largest θ_0 with less power consumption, and another for the smallest one with the largest power requirement.

In figure 3.15c, negative values of efficiency are observed for negative values of C_T. Values smaller than -0.5 have been omitted in the plot. The maximum efficiency reached 25%, and it was observed for cases with $2\theta_0$ = 56 at the two smallest Re, for $0.4 < St < 0.6$. For $St >$0.6 the efficiency goes to values slightly under 15%. In the case with the largest $2\theta_0$ (72), the trend is increasingly exponential independently of Re, with values tending also to approximately 15% when $St >$0.6. For the smallest angle, the local maximum appears in the range $0.4 < St < 0.6$, with values of efficiency near 13%.

Very high values of efficiency up to 87% have been reported in studies with devices implementing much more complex kinematics, such as combinations of pitch and heave (Anderson et al., 1998; Hover et al., 2004; Read et al., 2003). However, it was not the purpose of the work presented here to reach such high efficiencies but to simplify the system as mush as possible, in order to isolate the number of parameters affecting the problem. The same philosophy was applied to other works such as Green and Smits (2008) and Buchholz and Smits (2008), in which the authors reported experimental research showing the thrust performance of rigid pitching panels, with values of efficiency close to the ones presented here. In the first, the focus is given to the investigation of three-dimensional effects by varying aspect ratio of the panel, and in the second, the authors extended the work by including a detailed study showing efficiency trends similar to the ones presented in this work. Their research was carried out with panels of different aspect ratio, ranging from 0.54 to 2.38 and again the focus is given to three-

dimensional effects. They concluded (Buchholz and Smits, 2008) that over a certain range of aspect ratios, the efficiency was not strongly affected by three-dimensional effects, that only happened when the panel had an aspect ratio well under 1.

The main figure in this section illustrates in dimensionless form, how the different parameters in the experiment (θ_0, f, U) affect efficiency, and therefore how the energy input to the system in terms of torque and angular speed, ends up being thrust.

3.3.5 *Wake dynamics*

The structures in the wake of the flapping system have been investigated using DPIV. Four cases have been chosen in between all those available, in order to study specific situations observed in figure 3.15. These cases appear in table 3.4, where the main parameters associated to them are specified.

Table 3.4: Cases of study

	$2\theta_0$	St	Re	C_T	C_P	η
case 1	24 °	0.65	8000	1.04	16.3	6.5%
case 2	72 °	0.84	8000	2.1	15.4	13.6%
case 3	24 °	0.45	8000	0.09	3.83	2.3%
case 4	56 °	0.47	6600	0.64	2.51	25%

Cases 1 and 2 have similar C_P, but clearly different C_T and η, with values falling in a different branch of figure 3.15b. Cases 3 and 4 have been chosen with similar Strouhal number, with values of C_P, each located again in a different branch, yielding very different thrusts and efficiencies. Case 4 is the case with the highest efficiency in between all data set. The results in figures 3.16 to 3.18 are all based on DPIV measurements obtained in these four cases. In figure 3.16, the averaged magnitude of the velocity field in dimensionless form, $V^*(x,y) = \frac{\overline{V}(x,y)}{U}$ is presented.

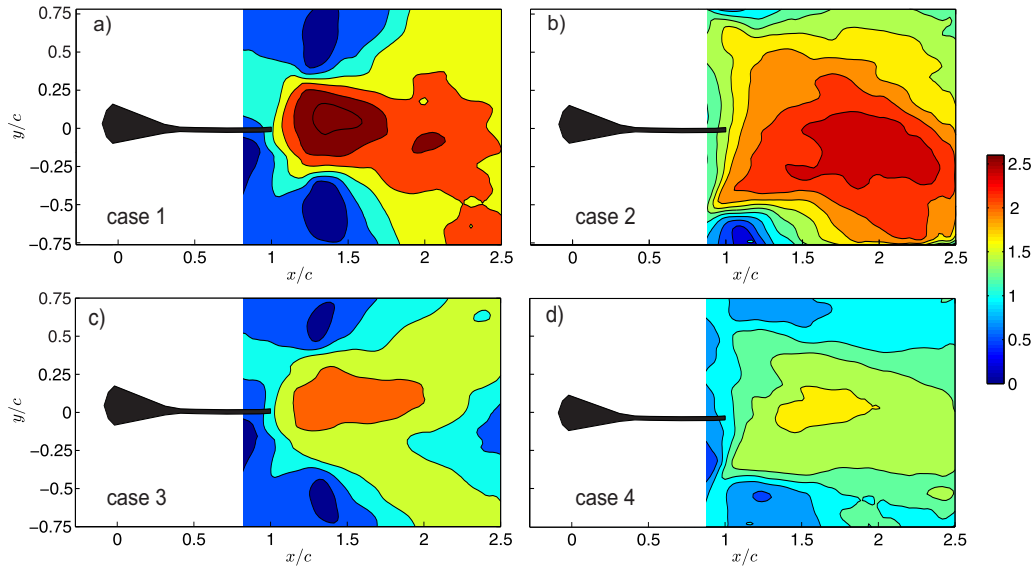

Figure 3.16: Dimensionless mean of the magnitude of the velocity field ($\frac{\overline{V}(x,y)}{U}$) for cases 1 to 4.

As figure 3.16 shows, regions with high velocities for case 1, with values $>2U$ were concentrated at the tip of the trailing edge around an area with x/c between 1 and 2 and y/c between -0.25 and 0.25. On the other hand, for case 2 in figure 3.16b, the area is much larger and goes in x/c from 1 to 2.5 and in y/c from -0.5 to 0.5. In cases 3 and 4, the velocity contours show similar patterns as those seen in cases 1 and 2. Velocities are smaller in cases 3 and 4, due to the fact that the flapping configurations in those cases implied less energy input to the system, as indicated by a smaller C_P (table 3.4).

The colour maps in figures 3.17 and 3.18 show dimensionless vorticity fields, $w_z^* = \frac{w_z c}{U}$. Clockwise vorticity appears in red and counter-clockwise in blue. Each column of plots in the figures, is for one case of the four different studied. Each row is the result of phase averaging the vorticity field at a different angular position of the foil, completing a full flapping cycle.

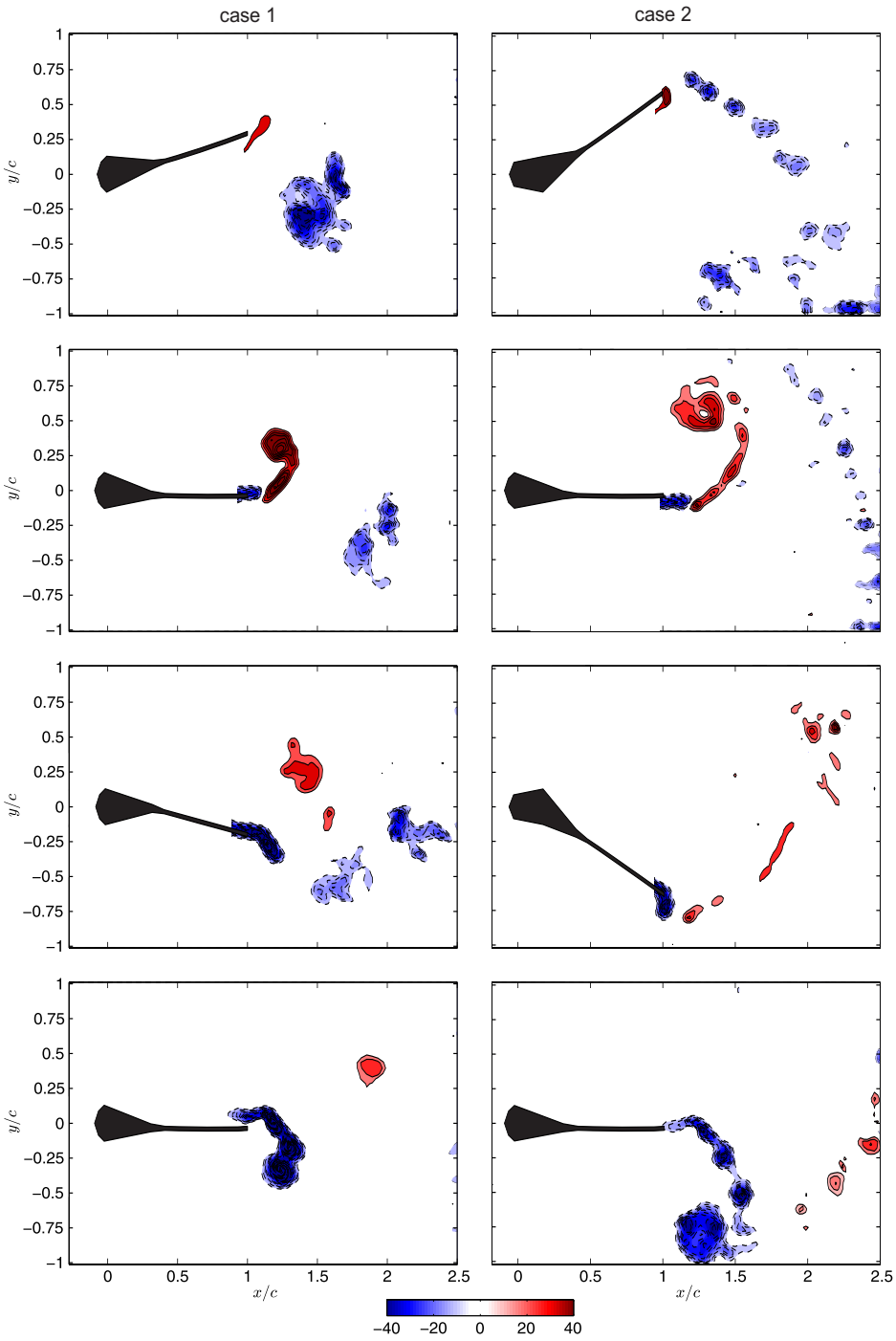

Figure 3.17: Phase averaged vorticity fields at four different foil angular positions, for case 1 in the left column and for case 2 in the right one.

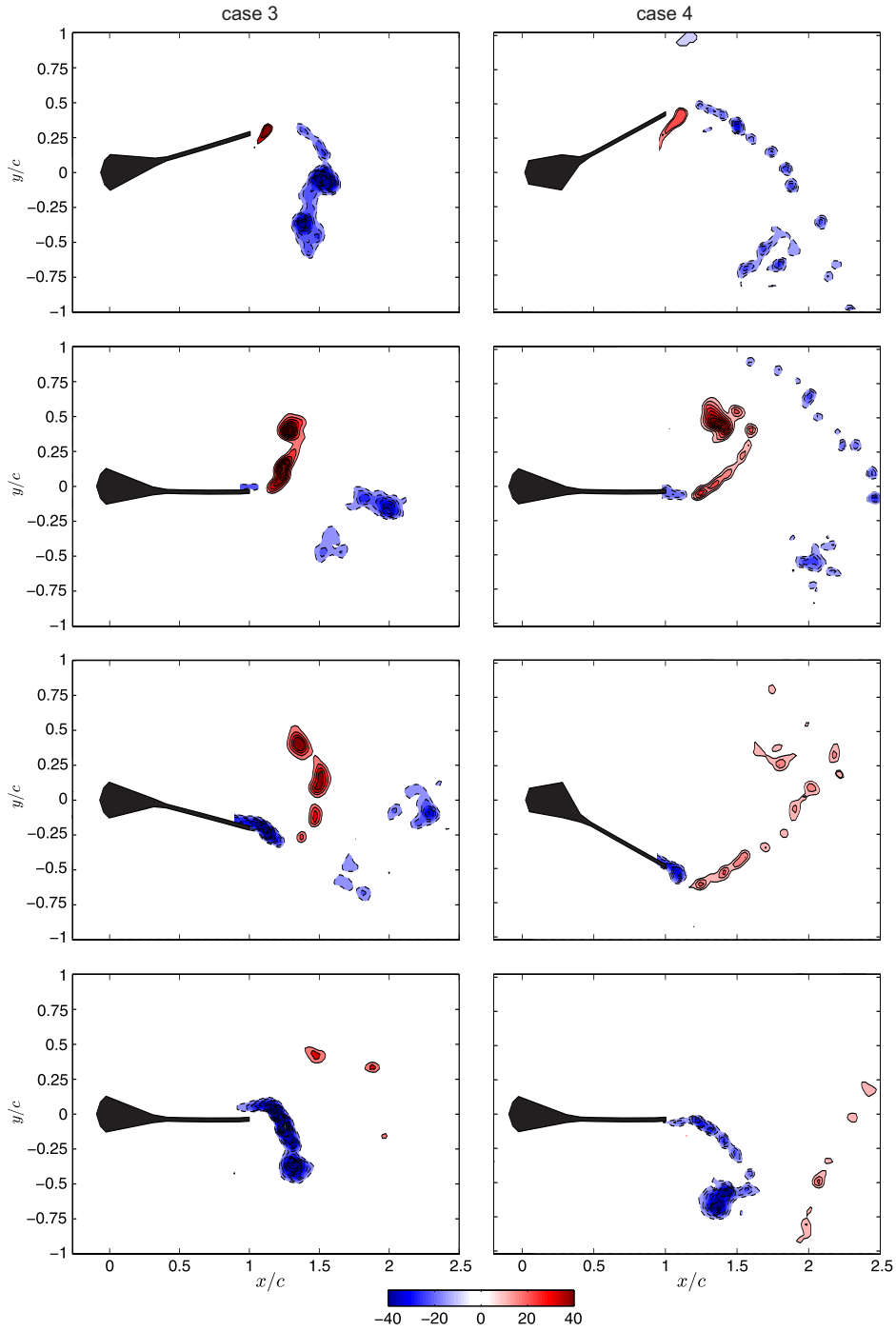

Figure 3.18: Phase averaged vorticity fields at four different foil angular positions, for case 3 in the left column and for case 4 in the right one.

The wake in case 1, left column of figure 3.17, consisted of a classical reversed von Kármán street with two vortices of opposite sign shed per flapping cycle. In case 2, right column of figure 3.17, the wake is remarkably different as the two main vortices appear combined with a row of shear layer vortices that resemble those typical in Kelvin-Helmholtz instabilities. Cases 3 and 4 in figure 3.18, again show very similar wake dynamics with clear shear layer instabilities for the largest swept angle.

3.3.6 *Discussion*

Thinking of bio-mechanical applications such as a fish or a robotic swimmer in a uniform current, the set-up presented here is able to simulate situations in which the swimmer, overcomes the fluid drag generating a forward motion (against the flow), balances the fluid drag being stationary or is not able to generate enough thrust so it moves backwards (with the flow). That corresponds to the different values of thrust seen in figure 3.15, resulting of the relationship between the in-line flapping force generated in the direction of the flow, the skin friction drag, the bluff body type form drag and the three-dimensional vortex-induced drag. The effect of the motion of the swimmer enlarging the skin friction drag, as a result of reduction of the size of the boundary layer, was discussed by Lighthill (1970) and very recently by Ehrenstein et al. (2014). Form drag is directly related to the foil's trailing edge kinematics that yield a certain projected swept area in the plane perpendicular to the propulsion direction. Recent work by Raspa et al. (2014) has shown how skin and form drag cannot account for the total drag experienced by an elastic swimmer in still fluid, as there is a major contribution of drag induced by the vortices generated at the ends of the foil, which indeed do not depend on the aspect ratio of the swimmer. This is in accordance with the study by Buchholz and Smits (2008), as previously commented in section 3.4.2.

Cases 1 and 2 in the present work show two situations in which the power input to the system was almost the same. Surprisingly, in case 2 the amount of thrust observed is twice as large that produced in case 1 (table 3.4), even though all three forms of drag should be larger in case 2.

Because of the capacity of the system to produce thrust when flapping with large amplitude, the net force is way larger in case 2, and therefore the efficiency too. The DPIV measurements provide a way to explain this phenomenon from the wake dynamics point of view. Figures 3.16a) and 3.16b) show a very different type of structure in the wake of the foil. In case 1, the jet-like structure that appears, has a clear inclination respect to the propulsion direction (in the positive and negative parts of the y/c axis), that yields a streamwise momentum flux reduction, meaning less thrust. In case 2, maximum values of averaged velocity are similar but cover a larger area in the wake and the inclined jet structure is not evident any more. The vorticity maps in figures 3.17 show the same condition. In the left column of the figure, with case 1, the streamwise momentum flux can be inferred by thinking of the direction perpendicular to the line that joins the centre of the two vortices shed per cycle in the wake, and how it has a clear inclination respect to the propulsion direction. The greater the angle the smaller the thrust the foil will be able to generate as a reaction force. In the right column of figure 3.17, with case 2, the tip or starting vortex is not coherent and small vorticity structures appear in the shear layer as in Kelvin-Helmholtz instabilities. This type of shear layer structures have been reported by previous authors either experimentally (Anderson et al., 1998; Buchholz and Smits, 2008; Godoy-Diana et al., 2008; Huai-Te Yu and Morrison, 2012a) or numerically Lewin and Haj-Hariri (2003); Bergmann and Iollo (2010); Zhang et al. (2010), and ended up producing a momentum flux better aligned to the propulsion direction. The same explanation applies to cases 3 and 4 in figures 3.16c), 3.16d) and 3.18, being case 4 the one with the highest efficiency as pointed out in table 3.4.

Dong et al. (2006), in their numerical experiments with a low aspect ratio foil, explained the lack of thrust seen in some of their cases, with the similar arguments, based on the directionality of the momentum structures in the wake. In Fernández-Prats et al. (2015), this effect was very evident in their experiments with an elastic undulatory swimmer near a wall, concluding that the reason for enhanced thrust at certain distances to the wall, was clearly due to the better alignment of the momentum flux to the propulsive direction, imposed by the wall. In a recent work

by Huera-Huarte and Gharib (2014), the authors show how by controlling actively the tip of a fin, the near wake can be modified in order to enhance thrust, by imposing momentum transfers better aligned to the thrust direction.

The cases in table 3.4, were chosen because they describe very well the two main types of vortex dynamics observed in the present experiments. A qualitative description of the dynamics observed, appears in figure 3.19. The plot in 3.19a) shows a generic case in which only part of the momentum is aligned to the thrust direction, whilst in the right hand side plot, this totally changes.

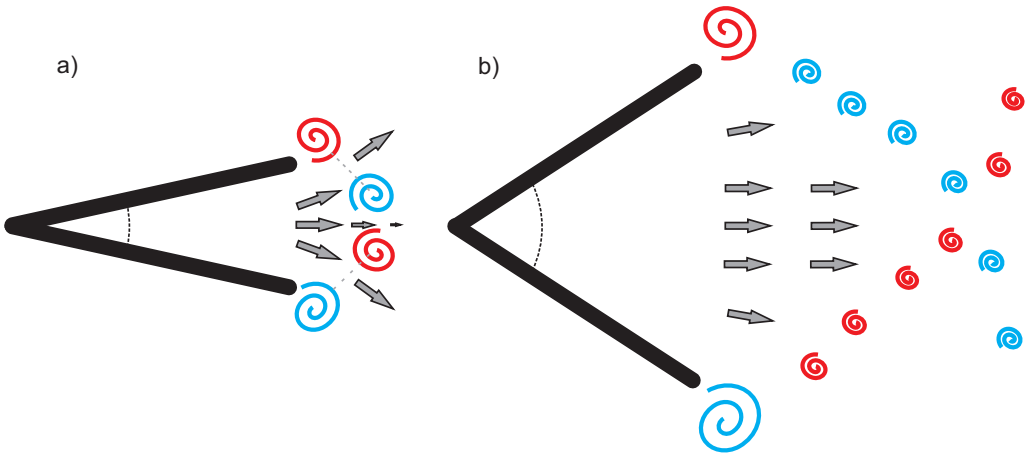

Figure 3.19: Qualitative representation of vortex structures in the wake of the rigid pitching foil.

3.4 EFFECT OF CHORDWISE FLEXIBILITY ON PITCHING PLATE PROPULSION

The results in this section are under preparation with the objective of submit it as a publication with the tittle of *"Effect of chordwise flexibility on pitching plate propulsion in a uniform current"*.

3.4.1 *abstract*

The role of the chordwise flexural stiffness in a rectangular foil undergoing pure pitching has been investigated. Digital Particle image velocimetry (DPIV) and load measurement with a 6-axes balance have been done to study the flow patterns and hydrodynamic forces around the flapping flexible foils. We have found a transition of thrust generation in the $semi-flexible$ foil with θ_0= 72 $^\circ$ for all the Re studied between 0.4 $\leq$St$\leq$ 0.65, this range is close to the range previously dictated by Triantafyllou et al. (1993) to maximize the thrust by a flapping foil. As a result the optimum flexural stiffness has been determined with the $semi-flexible$ foil with up to 69% efficiency for $Re = O(10^4)$ tested in the investigation.

3.4.2 *Introduction*

Animals have evolved various swimming and flying techniques involving flapping their wings or fins as a method of propulsion. They have developed for millennia the ability to optimize their motion with high efficiency in water or air. Aquatic animals features such as high velocities, sharp turning maneuvers, rapid acceleration, turbulence control, escape maneuvers, drag reduction... fit perfectly with the design for autonomous underwater vehicles ($AUVs$). The diversity of AUV applications is increasing in a wide range of military and civil fields, which are divided into four areas; land management, commercial, earth science and homeland security. For these reasons the attention on flapping propulsion at low Reynolds numbers ($\approx 10^4$) has increased recently.

The development of high propulsive performance in nature has brought about extensive research in these fields using theoretical and numerical techniques.

The first research on thrust for an oscillating rigid airfoil was carried out by Knoller (1909) and Betz (1912). In the middle of 1930s a theoretical explanation was given about the different patterns of a large-scale drag wake and a thrust wake, von Kármán and Burgers (1935). Following these studies, theoretical models by Garrick (1937), Lighthill (1975), Wu (1971a) and Chopra (1976) under oscillating foils in inviscid flow were done. An important advance was achieved by Triantafyllou et al. (1993), where the range of propulsive efficiency between $0.25 \leq \mathrm{St} \leq 0.45$ was found using a two-dimensional linear stability analysis on the wake of a pitching foil. More recently studies have been investigating numerically with an unsteady panel method (Cebeci et al., 2005) and Navier-Stokes simulations (Tuncer and Platzer, 1996; Wu and Sun, 2004).

Experimental studies have focused on finding out high efficiencies (Anderson et al., 1998; Schouveilera et al., 2005), the effect of the oscillating modes (Read et al., 2003; Hover et al., 2004), aspect ratios (Jones et al., 2002), different patterns in the wake (Koochesfahani, 1989; Buchholz and Smits, 2006, 2008; Schnipper et al., 2009; Green et al., 2011; Fernandez-Prats and Huera-Huarte, 2014) and flapping under ground effect (Blevins and Lauder, 2013; Quinn et al., 2014a; Fernández-Prats et al., 2015) with a rigid airfoil/foils.

The beginning of the theoretical investigations with a flexible propulsor started with the use of the linear theory by Wu (1971b) or inviscid theory (Katz and Weihs, 1978, 1979; Bose, 1995; Liu and Bose, 1997; Ramamurti et al., 1999). It was found that flexible propulsors (low levels of deformation) were achieving better efficiencies compared to a rigid propulsor with a small penalty to the thrust. In addition to the investigation of efficiencies of flexible propulsor (Miao and Ho, 2006), more recently, deformable passive bodies have been analysed using the incompressible Navier-Stokes equations (Bergmann and Iollo, 2010) and the multiblock lattice Boltzmann method (Zhang et al., 2010).

Despite the important role of flexibility in the wings or fins (Triantafyllou et al., 2000) of animals, the stiffness of insect wings when they are

flying is still unclear (Maxworthy, 1981). A few studies have quantified the deformation of the biological structures involved in locomotion. In the case of air the shape, flapping, flexion and the flexural stiffness has been studied with the scaling and the influence of wing venation as well as the spatial distribution and dynamic bending by Combes and Daniel (2001, 2003a,b). In the case of water, there is not yet available a suite of data for flexible propulsor (Lauder et al., 2006). Yamamoto et al. (1995) studied an oscillatory propulsion control system with different flexibilities of fins as a vehicle actuator in ship models. Fins with seven flexibilities were tested, the fin with 15% rigidity obtained the best efficiency of up to 31%. The effect of chordwise flexibility undergoing pitching, heaving and both motions has been studied experimentally by Prempraneerach et al. (2003), Heathcote and Gursul (2007a), Zhao et al. (2009b) and Barannyk et al. (2012). Prempraneerach et al. (2003) found a 36% increase in efficiency compared to a rigid foil, with a small loss in thrust. Heathcote and Gursul (2007a) ascertained benefits in the efficiency and noticed the strength of vortices is slightly larger for the flexible foil compared to the rigid one and substantial differences in the Re. Forces in flapping wings were studied by Zhao et al. (2009b) finding aerodynamic forces can be controlled by altering the trailing edge flexibility of a flapping wing and thereby controlling the magnitude of the leading edge vorticity. Varying the amplitude (peak to peak) Barannyk et al. (2012) obtained peak efficiency at 80% fixing the oscillation frequency at the values of St numbers corresponding to a maximum efficiency previously calculated.

In the current work, we study the role of foils with different flexural stiffness in flapping swimming undergoing of pure pitching. The study is approached from purely physical consideration, mimicking, in a simple way, different flexibilities of the caudal fin of a fish. Experimental measurements of thrust, power consumption, efficiency and time-resolved velocity flow fields are analysed. The next section describes the experimental methods, followed by a discussion of the results and the investigation finishes with the conclusions. Hydrodynamic forces at different flexural stiffness are evaluated to define high efficiencies to produce drag-based propulsion. At the end of the paper we discuss results

of PIV measurements associated with each flexural stiffness in order to reveal proper features of a wake with higher efficiencies.

3.4.3 *Methods*

3.4.4 *Experimental set-up*

Hydrodynamic forces on flapping foils were measured on a mechanical model (fig. 3.20c). Experiments were carried out by towing the model in a still water tank, 2 *m* long with a square cross-section of 0.6×0.6 m^2. The experimental setup is described in detail in Huera-Huarte and Fernandez-Prats (2015). An electric AC motor with a gear box (1:10) was used to move the carriage along a two rail system (fig.4.1). A potentiometer installed in the shaft of the motor, allowed closed loop control of the position of the towing carriage.

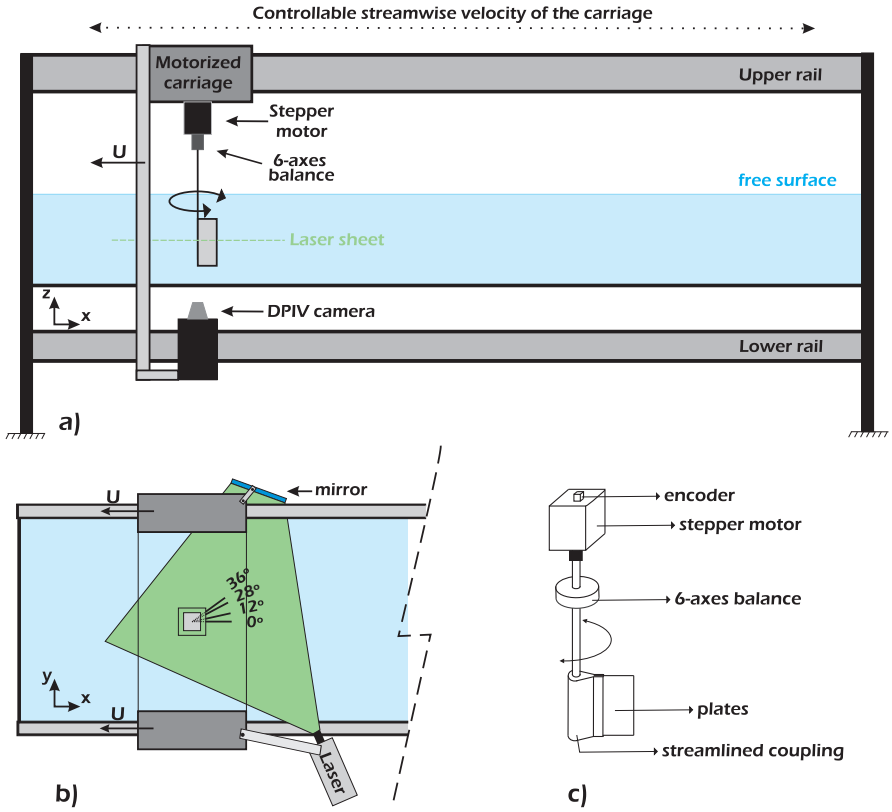

Figure 3.20: a) Side view of the experimental set up, b) top view. c) Apparatus of the mechanical model.

The flapping model was set up on the carriage of the towing tank attached to a 6-axes balance. The pitch motion imposed to the flapping device was produced by a stepper motor and consisted of a sinusoidal motion that can be approximated by equation,

$$\theta(t) = \theta_0 sin\ (2\pi f t), \tag{3.13}$$

where f is the flapping frequency and θ_0 is half of the swept angle of the pitch motion. The angular position of the flapping foil motion was measured using a digital encoder. Hydrodynamic forces and moments were measured with a 6-axes balance coupled to the main shaft of the system (fig. 4.1c). Foils were clamped to the shaft with a streamlined

coupling allowing only chordwise deformation. The system was set in a way that the foils ended up 15 *cm* below the water free surface and 15 *cm* above the bottom of the tank. The foil was made of a stainless steel sheet (E=210 GPa), 120 mm wide (chord - c) and 200 mm high (span - s) with an aspect ratio (s/c) of 1.67. The Strouhal number (St) is defined as $\frac{fA}{U}$, where A is the peak to peak excursion of the trailing edge and U is the towing speed. Reynolds numbers ($\frac{Uc}{\nu}$) up to 9250 were achieved during the experiments. In the previous expression ν is the kinematic viscosity of the fluid. The main parameters of the experiment are summarized in table 3.5.

Table 3.5: Parameters of the experiment.

Parameters			
Span	s	200	mm
Chord	c	120	mm
Aspect ratio	s/c	1.67	-
Flapping frequency	f	0.2 - 1.2	Hz
Amplitude	A	4.7, 10.8, 13.5	cm
Towing speeds	U	5.5 - 7.7	cm s^{-1}
Swept angles	$2\theta_0$	24, 56, 72	degrees
Reynolds numbers	Re	6600 - 9250	
Strouhal numbers	St	0.1 - 0.9	

In order to analyze the effect of the stiffness on the hydrodynamic forces, three different values of flexural stiffness EI were investigated (E is Young's modulus and I is the second moment of area). Values of EI varied widely from semi-rigid to very flexible, as detailed in table 3.6. An infinitely rigid foil was studied by Huera-Huarte and Fernandez-Prats (2015). The 3 foil models tested here are named as $semi-rigid$, $semi-flexible$ and $flexible$ from now on.

Table 3.6: Different flexural stiffness.

model name	h (mm)	EI (N/m^2)
semi-rigid ($s-r$)	0.15	5.9e-2
semi-flexible ($s-f$)	0.1	1.75e-2
flexible (f)	0.075	7.4e-3

As table 3.6 the flexural stiffness was varied by modifying the thickness of the foils as given by the expression $EI = Eh^3/12$.

3.4.4.1 *Quantitative flow imaging*

To study flow patterns generated by the pitching foils, digital particle image velocimetry (DPIV) was employed in order to obtain planar velocity flow fields around the model. The water in the tank was seeded with hollow glass spheres of 10 μm in diameter. A continuous wave 3 W Diode-Pumped Solid State green laser (532 nm), produced a planar light sheet that illuminated the tracer particles. Light scattered by the tracer particles was imaged by using a digital camera (equipped with optics of focal length 20 mm) based on a CMOS sensor of 4.0 MPixel (2048 x 2048). The camera was attached to the carriage on its lower rail pointing upwards, covering a field of view of 255 mm in the streamwise direction and 240 in the transverse one ($2.1c \times 2c$) approximately. The laser sheet was set up in order to illuminate the mid point of the foil in the spanwise direction (details in fig.4.1). A total of 1600 images were acquired during each experiment at a rate of 224 images per second with an exposure of 1.2 ms. Dynamic masking was used to identify the position of the foil in each frame. Two dimensional velocity fields were computed by applying a Fast Fourier Transform (FFT) based multi-pass window-deformation technique (Willert and Gharib (1991)). The algorithm evaluated the images after two iterations. Initially, the interrogation area was set to 64 x 64 and subsequently a 32 x 32 pixel window with 50% overlap was used.

3.4.5 *Results and discussion*

3.4.5.1 *Kinematics of the foils*

The deformed shape of the foils was obtained by pre-procesing the DPIV. This pre-procesing step allowed also dynamic masking for the DPIV computations, as already explained in section 3.4.4.1. Figure 3.21 shows the trajectories of the trailing edge of the foil in the xy plane, for 9 experiments with different Reynolds number, flexural stiffness and Strouhal number. Dashed lines represent the amplitudes of a rigid foil would have with the three swept angle. Each color in figure indicates the same swept angle, Reynolds and Strouhal number the only difference is the flexural stiffness of the foils. Depending on the flexural stiffness each foil shows differences in the trajectories and amplitudes. Amplitudes tend to decrease as the flexural stiffness is reduced. In the semi-rigid case the trajectory of the tip is parablolic, but as the flexural stiffness is lowered, the tip starts moving in a figure 3.21c of 8 shape.

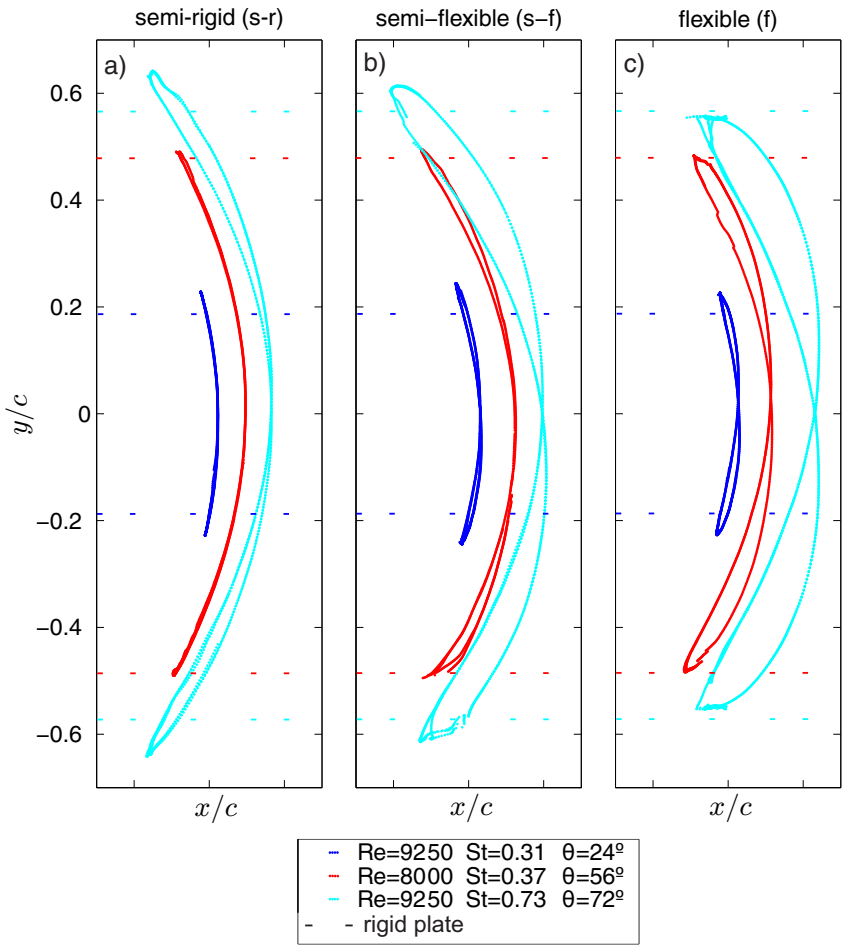

Figure 3.21: Trailing edge trajectories of the foil. a) semi-rigid foil $s-r$, b) semi-flexible foil $s-f$, c) flexible foil f.

3.4.5.2 *Hydrodynamic coefficients*

Forces and moments acting on the foil were measured with the multi-axis load cell by sampling at a frequency of 5 kHz. The force (F_x) measured in the streamwise direction is the instantaneous net force in the direction of thrust (from now on thrust) on the foil. Time-averaged values of $F_x(t)$ are designed as $\overline{F_x}$ and are given by equation,

$$\overline{F_x} = \frac{1}{nT}\int_0^{nT} F_x(t)\,dt, \tag{3.14}$$

the mean thrust coefficient is defined as,

$$C_T = \frac{\overline{F_x}}{\frac{1}{2}\rho U^2 cs} \tag{3.15}$$

and the input power coefficient is given by,

$$C_P = \frac{\overline{P}}{\frac{1}{2}\rho U^3 cs} \tag{3.16}$$

where $\overline{P}$ is the time-averaged input power per cycle, computed as follows,

$$\overline{P} = \frac{1}{nT}\int_0^{nT} M_z(t)\theta'(t)\,dt \tag{3.17}$$

In the equations T, n and ρ are the period of the oscillatory motion, the number of the cycles used for the calculation and the density of the fluid, respectively. Therefore, the hydrodynamic propulsive efficiency is defined as the ratio of the thrust coefficient to the input power, calculated as,

$$\eta = \frac{C_T}{C_P} = \frac{\overline{F}_x U}{\overline{P}} \tag{3.18}$$

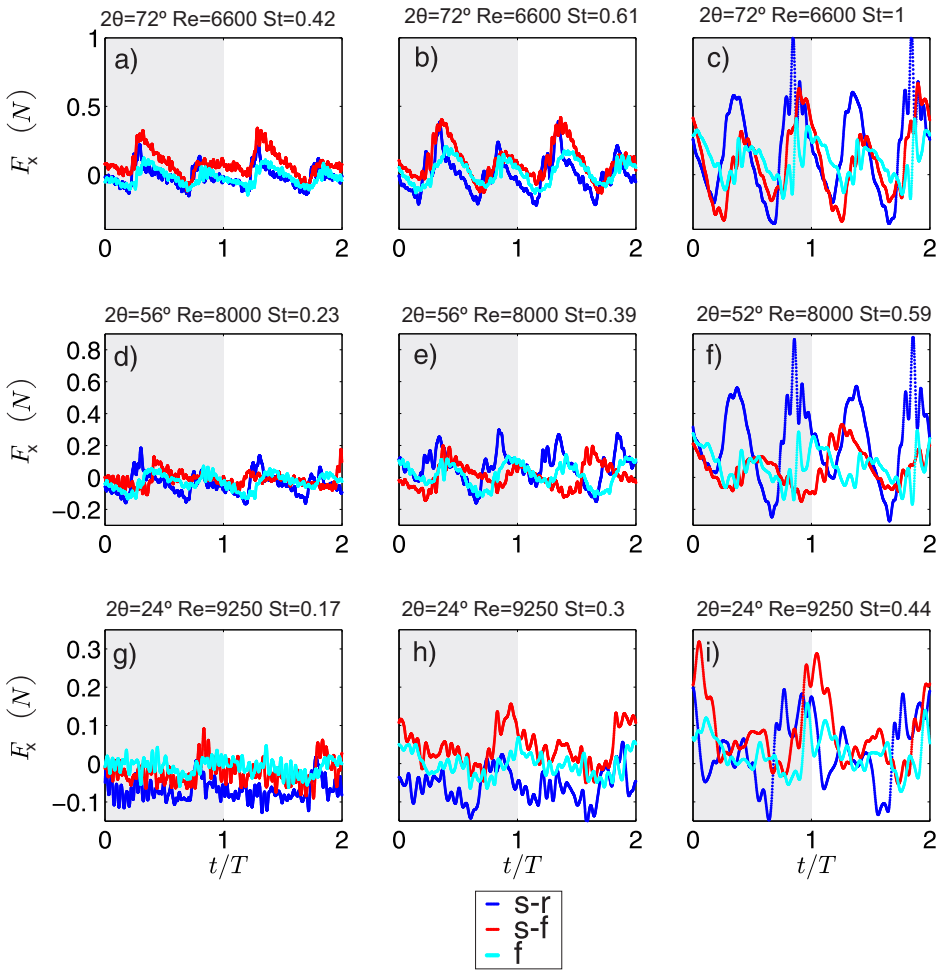

Figure 3.22: Thrust (net streamwise force) as a function of dimensionless time (t/T), for several cases with different Re, θ_0 and EI. Two cycles are shown, the first one is shadowed for clarity.

Figure 3.22 shows the time series of the thrust ,$F_x(t)$, for several experiments conducted at different Reynolds numbers, swept angles and flexural stiffness. In the figure, values of Reynolds numbers increase from top to bottom, values of swept angle increase from bottom to top and values of Strouhal numbers increase from left to right. In each plot the three flexural stiffness tested are plotted using different colours (blue, red and cyan for *semi-rigid*, *semi-flexible* and *flexible* foils, respectively). In

all plots 2 full flapping cycles (the first one is shadowed) with the time in dimensionless form (t/T). The capacity of the system to generate thrust increased for all the flexural stiffness when St was increased. In generally the $semi-rigid$ and $semi-flexible$ foils achieved higher thrusts than the $flexible$ one.

Coefficients described previously in this section are presented as a function of Reynolds numbers, swept angles, flexural stiffness and Strouhal numbers. In figures 3.23 to 3.25 the dimensionless amplitude (A^*/c), the thrust coefficient (C_T), power coefficient (C_P) and the efficiency (η) are shown as a function of Strouhal number for each flexural stiffness. A^* is the effective amplitude of the tip of the foil as measured by means of the image processing.

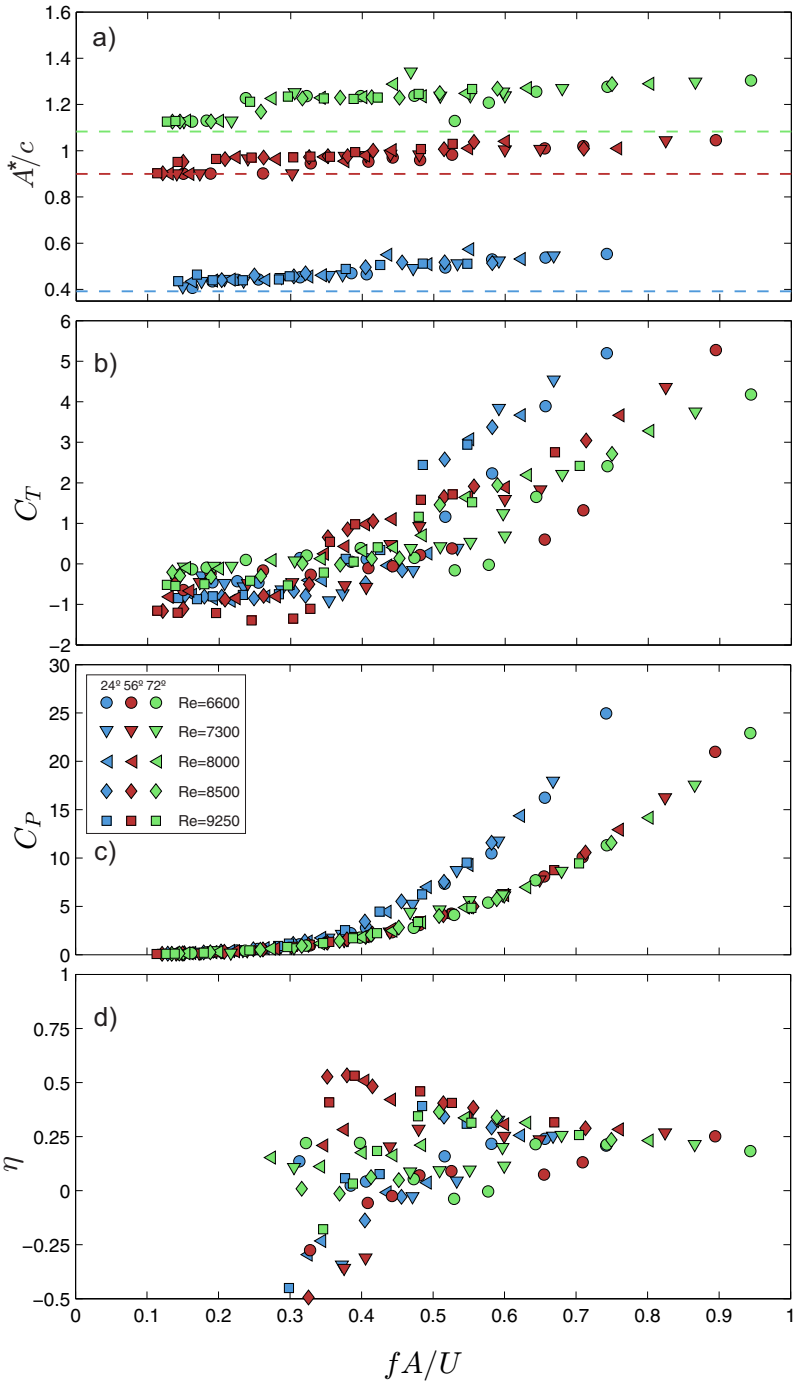

Figure 3.23: *Semi − rigid* foil. a) Dimensionless amplitude (A^*/c), b) thrust coefficient (C_T), c) power coefficient (C_P) and d) hydrodynamic efficiency (η) as a function of fA/U. Dashed lines in a) plot represent the dimensionless amplitude of a rigid foil. Symbols are used for each different *Re* and colours are used for different θ_0.

Results of the $semi - rigid$ foil in figure 3.23, C_T increased monotonically with Strouhal number, but two clear trends can be seems. For $St < 0.35$, results of C_T generated a negative net force in the streamwise direction. With $St > 0.35$, values of C_T were sorted by swept angles. The C_P plot (figure 3.23c) showed two main branches with quadratic trends respect to Strouhal number depending on swept angle. These two particular trends at the C_P are quite similar to the data of the rigid foil reported in Huera-Huarte and Fernandez-Prats (2015). The largest efficiencies appeared for $Re \geq 8000$ and two ranges of Strouhal number. One range at $0.37 < St < 0.42$ for $\theta_0 = 56^\circ$ and the second range at $0.47 < St < 0.52$ for $\theta_0 = 24^\circ, 56^\circ, 72^\circ$ (see figure 3.23d).

In plot 3.23a, the dimensionless amplitude (A^*/c) increased with the St for all the θ. Each plot of the figure 3.23 was plotted versus fA^*/U with a resulting more scattered data.

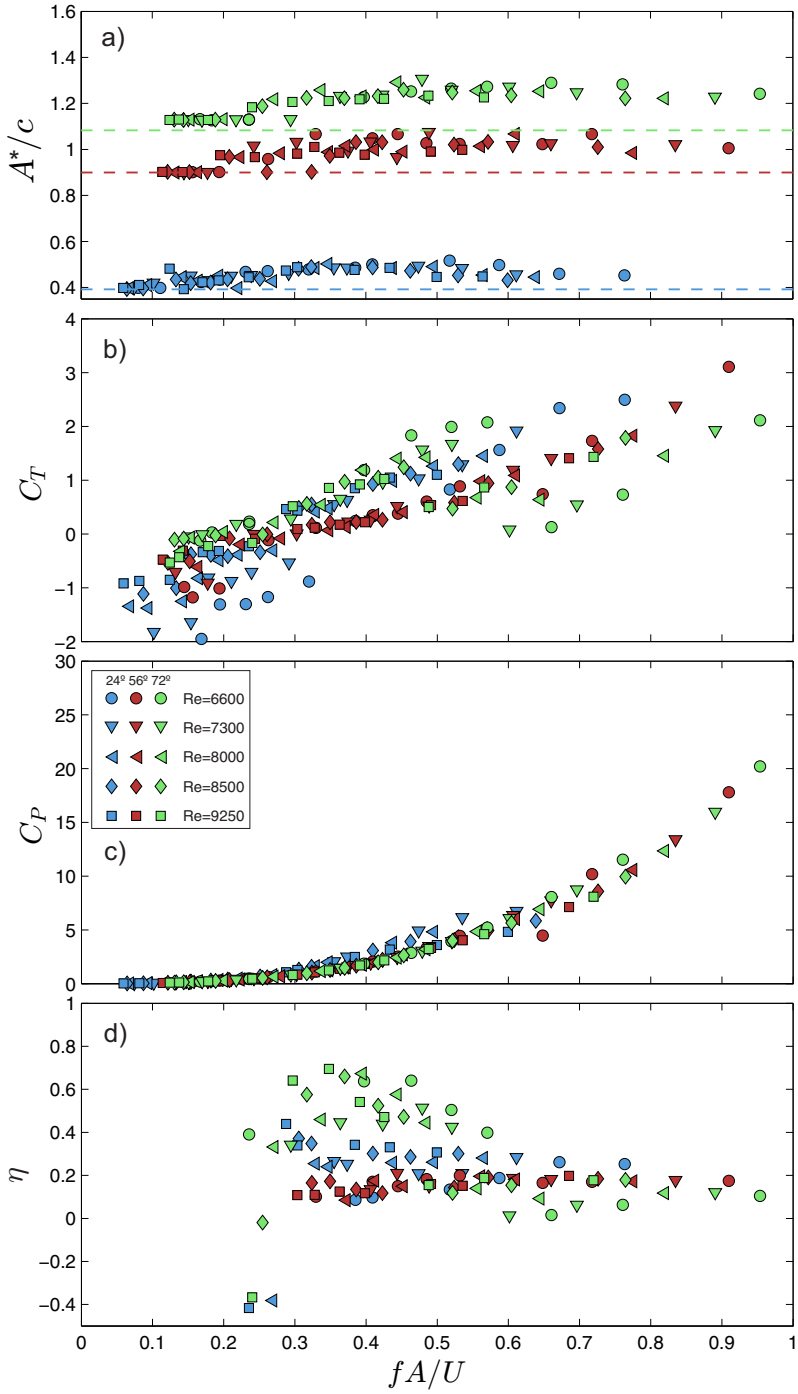

Figure 3.24: *Semi − flexible* foil. a) Dimensionless real amplitude (A^*), b) thrust coefficient (C_T), c) power coefficient (C_P) and d) hydrodynamic efficiency (η) as a function of fA/U. Dashed lines in a) plot represent the dimensionless amplitude of the rigid foil. Symbols are used for each different *Re* and colours are used for different θ_0.

Result for the $semi - flexible$ foil presented in figure 3.24a increases of effective amplitude for all swept angles when the Strouhal numbers increased up to a certain $St \simeq 0.5$ which A^* fall for $\theta_0 = 24^\circ$ and 56°. C_T of the foil presented a sorted trends with Reynolds numbers for $C_T < 0$ (figure 3.24b). To $C_T > 0$ each swept angle resulted in a liner increase with Strouhal numbers, except for the case $\theta_0 = 72^\circ$ in which C_T the thrust production capacity of the foil increases monotonically up to $St \approx 0.55$ and then drops suddenly. C_P data obtained a quadratic trends with Strouhal numbers independent of Reynolds numbers and swept angle (see figure 3.24c). The highest hydrodynamic efficiencies found were obtained for $\theta_0 = 72^\circ$ (see figure 3.24d). The higher efficiency values fall within the range of $0.24 \leq St \leq 0.58$. These efficiencies are also the largest if the different foils are compared.

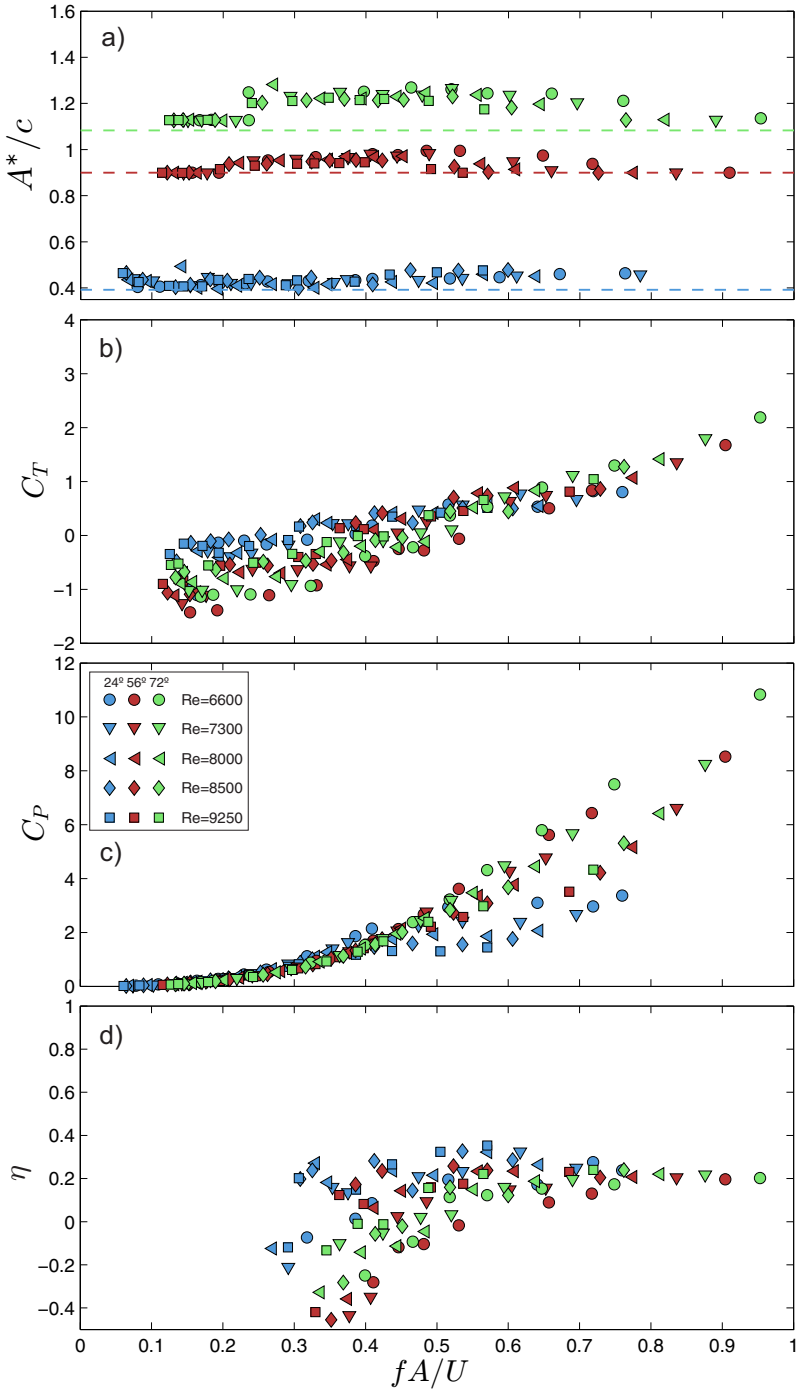

Figure 3.25: *Flexible* foil. a) Dimensionless real amplitude (A^*), b) thrust coefficient (C_T), c) power coefficient (C_P) and d) hydrodynamic efficiency (η) as a function of fA/U. Dashed lines in a) plot represent the dimensionless amplitude of the rigid foil. Symbols are used for each different *Re* and colours are used for different θ_0.

For the $flexible$ foil, effective amplitude showed increases only for θ_0= 56 ° and 72 ° until a certain $St \simeq 0.5$ which the effective amplitude fell. C_T increased with a linear trend with Strouhal numbers. For $C_T < 0$ a more pronounced dependency of Reynolds numbers was measured in the flexible foil (see figure 3.25b). This dependency reported the same features as in the previous case (figure 3.24b) as, it was obtained for $C_T < 0$, each result was highly ordered by Reynolds numbers and when Reynolds numbers increased C_T increased. Values of C_P for $St < 0.42$ collapse to the same quadratic trend as for the $semi - flexible$ foil (see figure 3.25c). $St > 0.42$ developed three branches ordered by swept angles. The largest hydrodynamics efficiencies of the $flexible$ foil were generated at $\theta_0 = 24\,^\circ$, this foil showed the lowest efficiencies among the three foils studied.

Figures 3.23 to 3.25 shown that the effective amplitude of oscillation is a function of the Strouhal numbers. For the $semi - rigid$ foil the effective amplitude increases with the Strouhal numbers; however for lower flexural stiffness the effective amplitude drops at a certain values of Strouhal numbers. This relationship, for various flexural stiffness and Strouhal numbers is shown in figure 3.26 in more details, where only a certain cases are plotted.

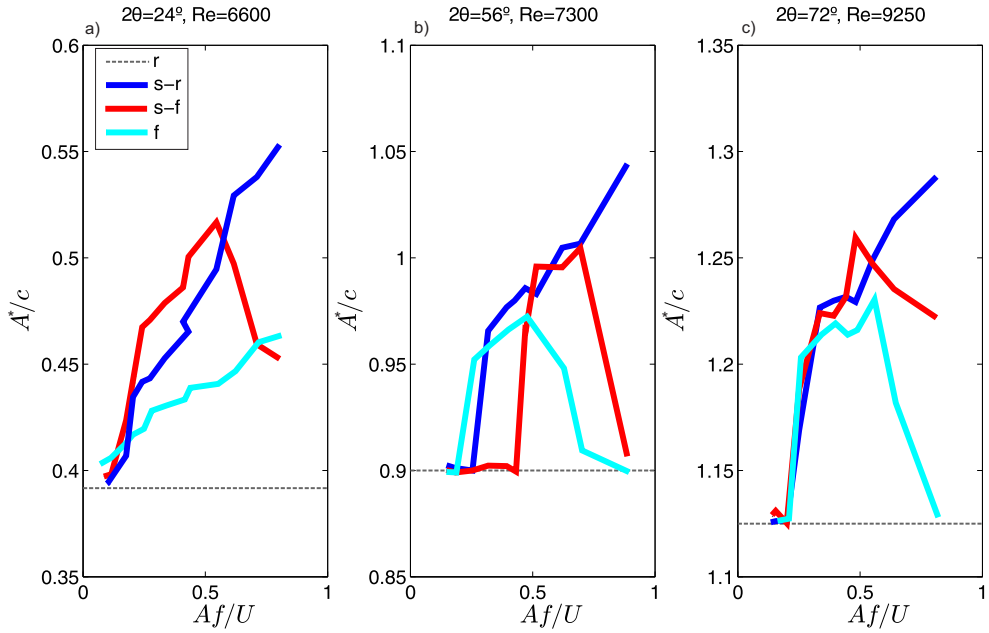

Figure 3.26: Dimensionless real amplitud (A^*) with the chord versus St.

Dashed lines in the plots represent the amplitude that a rigid foil would have for each. Dark blue lines are used for the $semi-rigid$ foil, red lines for the $semi-flexible$ foil and light blue lines for the $flexible$ foil.

$Semi-rigid$ foil increases the effective amplitude for all the cases in figure 3.26. $Semi-rigid$ foil increases the effective amplitude up to a certain Strouhal numbers where drops suddenly. The same trend have been observed with C_T in these two foil. In the case of the $flexible$ foil the effective amplitude is lower than than the rest of the foils (figure 3.26) which matches with the trends of C_T for the three foils. Therefore, the increase of C_T are related with the increases of the effective amplitude.

In the $semi-flexible$ and $flexible$ foils at low Strouhal number and $C_T < 0$ a strongly dependence of Reynolds numbers is produced (see figures 3.24 and 3.25). Results of the C_T are highly correlated with the Re confirmed the function of the C_T with the U of the carriage. This phenomenon can be explained because at low Strouhal and low flexural stiffness the deformed foil decreases the blockage area of the foil increas-

ing the C_T. This effect was more remarkable with the $semi-rigid$ foil with $\theta_0 = 24^\circ$ and at the $flexible$ foil with θ_0=56° and 72°.

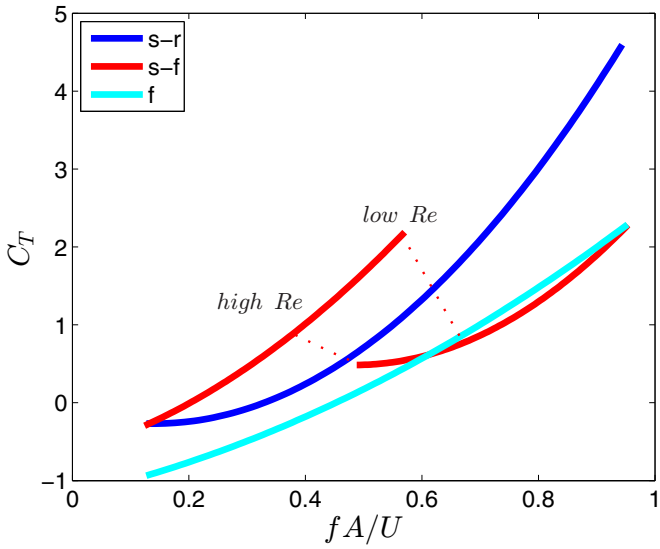

Figure 3.27: Quadratic fit of C_T to each foil versus St for θ_0= 72°. Colors are used for each flexural stiffness.

In figure 3.27 quadratic fits of C_T versus Strouhal numbers are plotted, dark blue lines for the $semi-rigid$, red lines for $semi-flexible$ and light blue lines for the $flexible$ foil. Each quadratic fit were calculated to all the data for θ_0= 72° of a single foil, but in order to differentiate the two behavior of the $semi-flexible$ foil two quadratic fits are presented, one before of the drop and the second after the drop. From figure 3.27 the capacity of thrust generation to different flexural stiffness can be analyzed. Higher thrust are observed for $semi-flexible$ and $semi-rigid$ foils. It should be noted that for a $St < 0.5$ $semi-flexible$ foil generated more C_T while for $St > 0.5$ $semi-rigid$ foil generated higher C_T. This figure proposes a transition in thrust generation as the behaviour of $semi-flexible$ foil. For $St < 0.5$ the behaviour of the $semi-flexible$ foil of thrust generation obtained similar trends as $semi-rigid$ foil however; for $St > 0.5$ after the drop, the behavior of the $semi-flexible$ foil is as the $flexible$ foil. This transition in a range of $0.4 < St < 0.65$ proposes

an interesting performance at the $semi-flexible$ foil providing high efficiency before of the drop. The dotted red lines in the figure identify that the transition is significantly stronger at low Reynolds numbers than at high Reynolds numbers.

In general the thrust and power coefficients decreased as the flexural stiffness decreased as is shown in figures 3.23, 3.24 and 3.25. We have measured that introducing a largest degree of flexibility ($flexible$ foil) decreased the efficiency of the propulsion system, in accordance with Heathcote and Gursul (2007b); Hobson et al. (2002). An important parameter is the effective amplitude of the tip (A^*) and it trajectories because they presented different features that can be linked to the improvement of C_T. We have seen a transition in the C_T results at the $semi-flexible$ between the $semi-rigid$ and $flexible$ foil. In this transition we have computed high values of C_T and consequently relatively high values of efficiency without increases of C_P. In this way to improve the propulsion varying the flexibility we have to chose an optimum flexural stiffness of the foil in order to maximize the C_T taking into account the penalization of the C_P. In the next section, data from DPIV measurements will confirm the differences of velocity fields to each flexural stiffness studied.

3.4.5.3 *Wake analysis*

DPIV analysis has focused in finding out the main role of chordwise flexibility on hydrodynamic propulsion. In the 495 experiments, within the range of Reynolds and Strouhal numbers considered we have found repeated differences in the average magnitude of the velocity fields depending on the flexural stiffness of the foils. In figure 3.28, nine dimensionless fields of the magnitude of the velocity field as $(\frac{\bar{V}(x,y)}{U})$ are plotted, in order to set the kinematic and isolate flexural stiffness for comparison each row in this figure has the same kinematic, Strouhal and Reynolds numbers but different flexural stiffness. The coefficients of C_T and C_P in each case are also plotted.

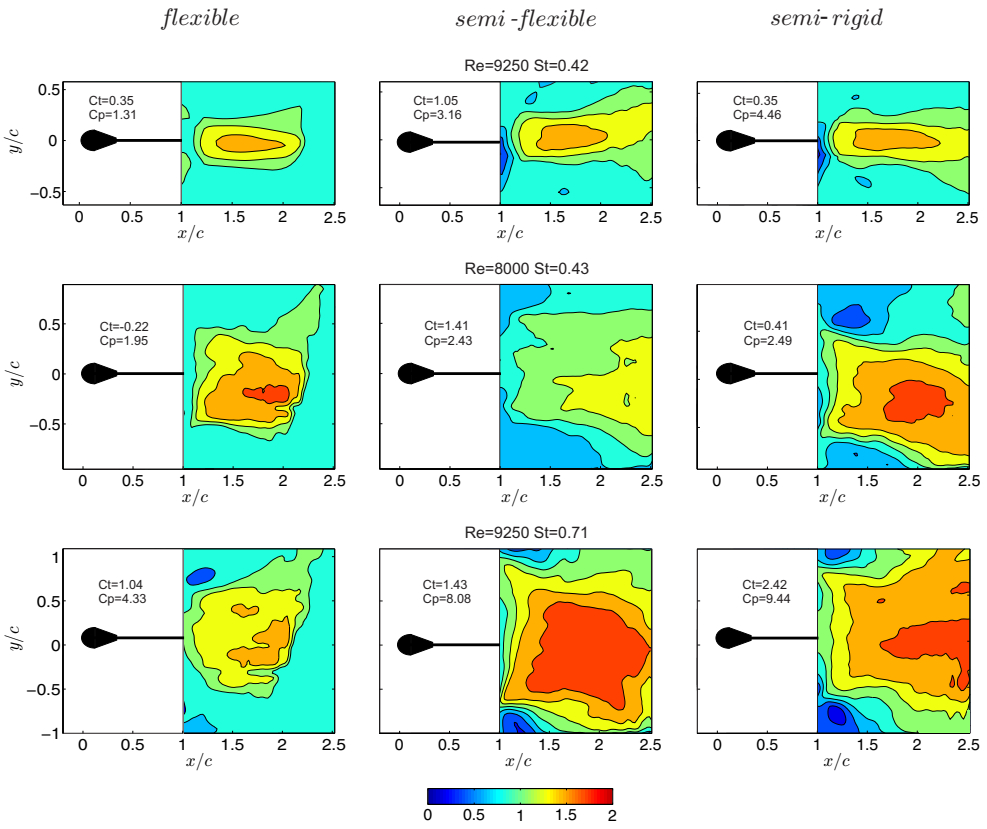

Figure 3.28: Dimensionless mean of the magnitude of the velocity field ($\frac{\bar{V}(x,y)}{U}$) for 9 cases.

As figure 3.28 shows, each row of regions of high velocities generated by the *flexible* foil is always lesser than the regions of high velocities of the $semi-flexible$ and $semi-rigid$ foils. Regions of high velocities obtained by the $semi-flexible$ and $semi-rigid$ foils summarized regions from the tip of the foils (x/c=1) until more than x/c=2.5. The *flexible* foil developed regions of high velocities close to the tip of the foil penalizing the thrust. According to the capacity of thrust generation based on C_T, in order to increase the thrust, long regions of high velocities are required (see in figure 3.28 $semi-flexible$ and $semi-rigid$ columns). If the width of the high velocity regions are compared it is possible to realize how the *flexible* foil always generated narrower regions due to the

higher flexibility of this foil. These several features of the different EI tested can reveal the transition of thrust generation already seen in the $semi-flexible$ foil, which it behavior started as the $semi-rigid$ foil but at $St \simeq 0.5$ become to as $flexible$ foil. These two behaviors can be linked to the two types of structures in the wake of the pitching foil already seen with the rigid foil in Huera-Huarte and Fernandez-Prats (2015). Where the type of wake with regions of high velocities contributed to a momentum distribution which is better aligned to the propulsion direction improving the capacity of thrust.

3.4.5.4 *Highest efficiencies cases*

The chapter finishes reporting the cases with the highest efficiency to each flexural stiffness studied and theses cases are in the followings table:

Table 3.7: Maximum performance for each foil, from low to highest range of efficiency.

Case	Foil	θ	St	Re	C_T	C_P	η
1	$flexible$	24°	0.57	9250	0.51	1.44	35%
2	$semi-rigid$	56°	0.38	8500	0.85	1.59	53%
3	$semi-flexible$	72°	0.35	9250	0.85	1.23	69%

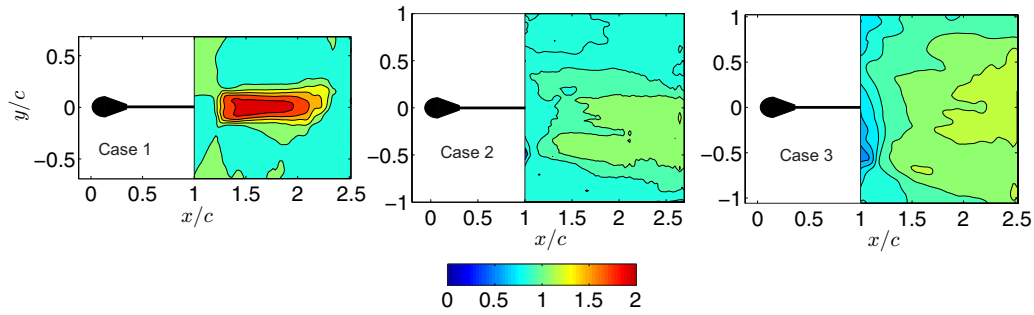

Figure 3.29: Dimensionless mean of the magnitude of the velocity field ($\frac{\bar{V}(x,y)}{U}$) for cases 1 to 3.

In figure 3.29 the averaged magnitude of the velocity field for cases 1 to 3 are plotted. As figure 3.29 shows, there are three well different fields. Case 1 showed a region with the highest velocity with values $\approx 2U$ concentrated at the tip of the trailing edge around an area with x/c between 1.2 and 2.2 and y/c between -0.25 and 0.25. Case 2 reported a much larger area with x/c from 1 to 2.5 and y/c from -0.5 to 0.5. The case with the highest efficiency (case 3) presented the biggest area with x/c between 1 and 2.5 and y/c between -1 and 1.

The colour maps in figure 3.30 shows dimensionless fields, as $w_z^* = \frac{w_z c}{U}$. Clockwise vorticity appears in red and counter-clockwise in blue. Each column in the figure is for one case of the three different studied. Each row is the result of the phase averaging the vorticity field at a different angular position of the foil, completing a full cycle.

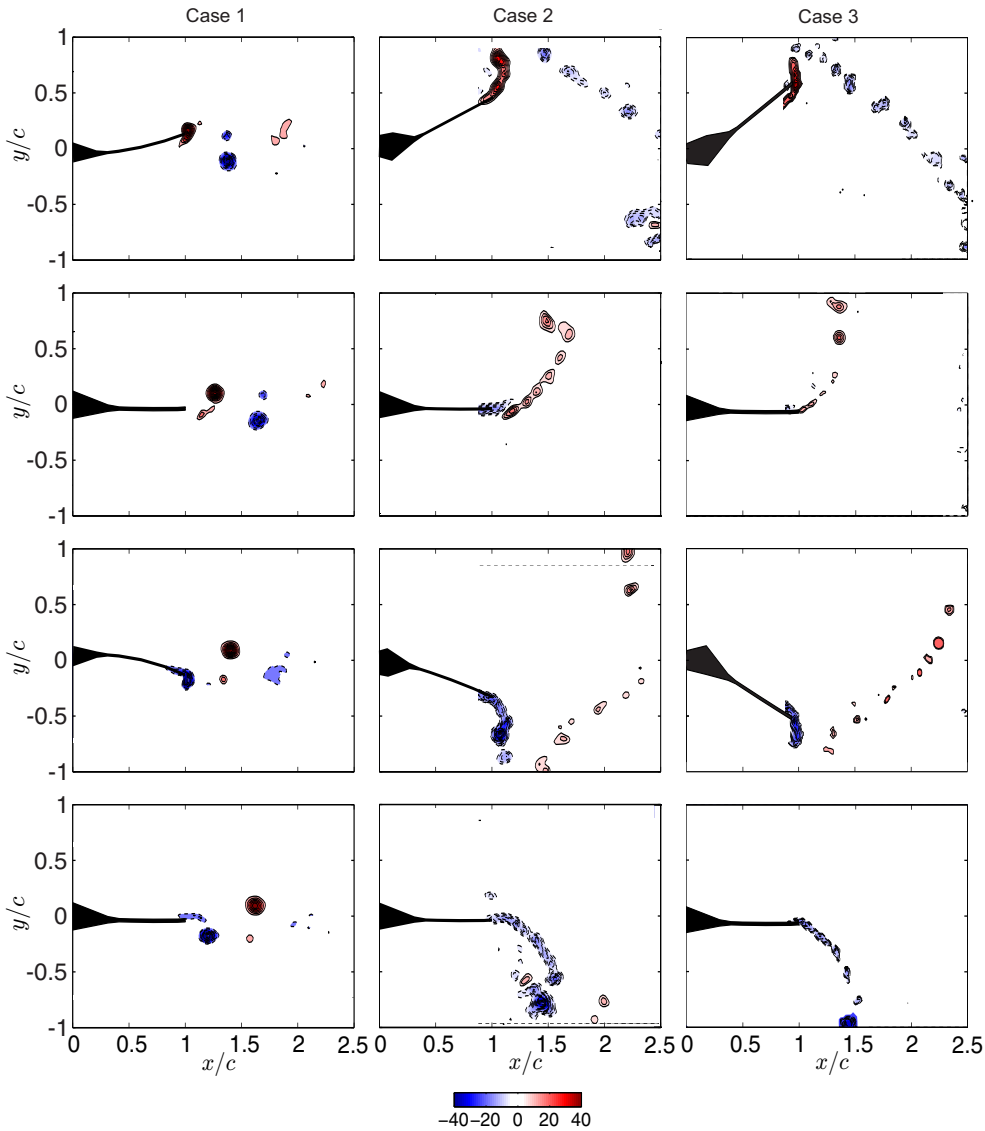

Figure 3.30: Phase average vorticity fields at four different foil angular positions, for cases 1 in the left column, for case 2 in the middle column and for case 3 in the right column.

In case 1 the left column in Figure3.30, the foil developed the classical reversed von Kármán street with two vortices of opposite sign shed per flapping cycle. In case 2 the central column in Figure3.30, the wake is

quite different as also the two main vortices of the von Kármán reverse appear with a line of small vortices in the shear layers. In case 3 the right columns in Figure 3.30, the main vortices appeared with the row of shear layer vortices, showing in a clearer way that case 2 and case 3 obtained very similar wake dynamics. These small vortices are are formed due to the Kelvin-Helmholtz instability and have been reported experimentally and numerically by Green et al. (2011), Huai-Te Yu and Morrison (2012b), and Zhang et al. (2010).

UNIVERSITAT ROVIRA I VIRGILI
HYDRODYNAMICS OF PITCHING FOILS: FLEXIBILITY AND GROUND EFFECTS
Rafael Fernandez Prats
Dipòsit Legal: T 979-2015

4

SWIMMING NEAR A WALL

The work presented in this chapter was done during an internship in the research group *Physique et Mecanique des Milieux Heterogenes* (PMMH) at the university of *ESPCI ParisTech*. The next section describes a brief introduction followed by the presentation and discussion of the results. In addition to performance measurements based on the trajectory tracking of the swimmer, time-resolved flow field measurements are presented, which permit us to relate the observed effects of swimming near a wall to changes in the wake vortex topology. At the end of the chapter we discuss the use of a proper orthogonal decomposition technique to analyse the changes in the energy distribution among the different components of the experimental velocity fields associated to the effect of swimming near the wall.

4.1 INTRODUCTION

The propulsive dynamics of a flexible undulating foil in a self-propelled swimming configuration near a wall has been studied experimentally. Measurements of the swimming speed and the propulsive force were performed, together with image acquisition of the kinematics of the foil and (DPIV) in its wake. The presence of the wall enhances the cruising velocity in some cases up to 25% and the thrust by a 45%. The physical mechanisms underlying this effect are discussed by studying the vorticity dynamics in the wake of the foil. POD is applied to the DPIV measurements in order to analyse the kinetic energy modal distribution in the flow and to relate it to the propulsion generated by the foil.

4.2 EXPERIMENTAL SYSTEM AND TECHNIQUE, FISH TANK

The experimental setup explained in this section has been performed in a fish tank in the PMMH[1] laboratory at the ESPCI[2] University.

4.2.1 *Experimental setup - fish tank*

The experiment was conducted in a water tank ($900 \times 800 \times 500$ mm^3), where a model of a self-propelled undulatory foil was allowed to move along the rectilinear direction imposed by an air bearing, installed outside the tank (see figure 4.1). The foil was made of a rectangular flexible Mylar foil of thickness 130 μm, chord $L = 110$mm and span $s = 100$mm, giving an aspect ratio $AR = s/L = 0.9$. The foil was held at one of its edges by a cylindrical shaft of diameter 5mm, acting as the head of the foil. Although three-dimensional structures are inherent to this type of flows because of end effects, the quasi-two-dimensional hypothesis can be justified here because of the aspect ratio used for the foil, as other authors have previously suggested (Buchholz and Smits (2008)).

1 Physique et Mécanique des Milieux Hétérogènes
2 École Supérieure de Physique et de Chimie Industrielles de la ville de Paris

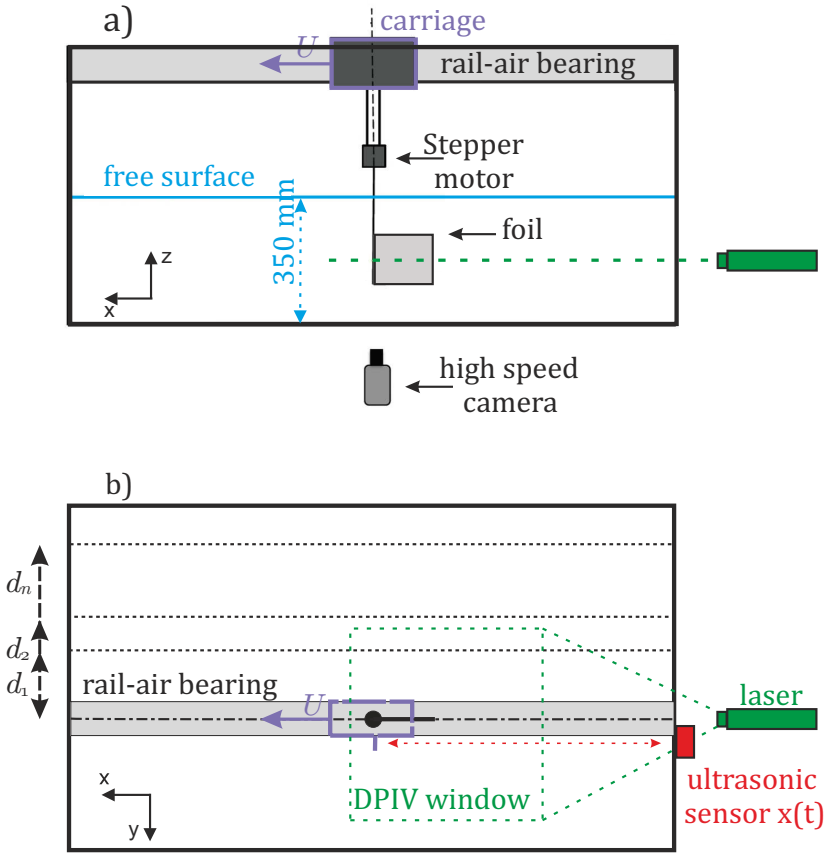

Figure 4.1: Experimental set up: (a) lateral and (b) top views.

The lowest natural frequency of the foil in water $f_0 = 0.42$ Hz was measured from the response of the foil to an impulse perturbation of the trailing edge as in Paraz et al. (2014). A pitching oscillation was imposed through this shaft by means of a stepper motor supported by the moving carriage of the air bearing (see also Raspa et al. (2013)). A motor driver card was used to control in time the angular position of the shaft, with 0.5° of accuracy. A sinusoidal pitch motion was imposed to the shaft yielding to a smooth travelling wave along the foil, providing the desired undulatory kinematics. The self-propelled foil's speed was obtained from time series of the position ($x(t)$), measured using an ultrasonic proximity sensor with an accuracy of 3 mm (see figure 4.1).

Additionally, the deformation of the foil was obtained from high-speed video recordings.

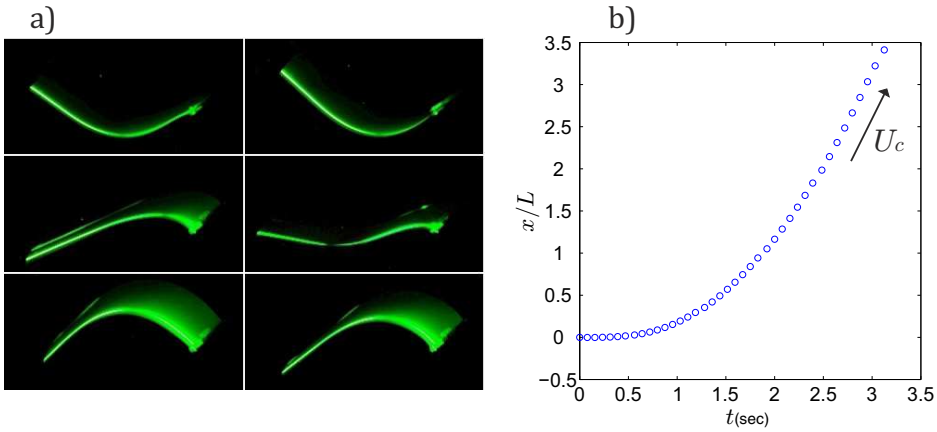

Figure 4.2: (a) Snapshots showing the kinematics of the foil using a laser sheet; (b) displacement of the foil $x(t)$, obtained from the ultrasonic sensor.

The parameters controlled in the experiments were the swept angle (θ_0), the frequency of the pitch motion (f) and the gap (d). The pitch motion imposed to the shaft or foil's head, can be described by the harmonic expression $\theta = 0.5\theta_0 \sin(2\pi f t)$. The pitch frequency was stepped with increment of 0.5Hz between each experimental case, except for the case with θ=240 degrees, in which the maximum frequency that the stepper motor could achieve was 3.3Hz instead 3.5Hz. The third important experimental parameter was the distance to the wall (D), written in dimensionless form ($d = D/L$), using the chord of the foil (L). Six distances to the wall were investigated with dimensionless gaps between 0.55-1.54. Strong interaction was observed for separations to the wall in the range 0.25-0.45. The wall effect was considerably weaker for d>0.45 with very small velocity and thrust variation. Other distances d were investigated between 0.55 and 1.54 showing practically no differences. Only the largest of those is shown, corresponding to d=1.54. The Reynolds number based on the foil length ($Re = U_c L/\nu$), ν being the kinematic viscosity of the fluid, was between 2200 and 19000. The experiment was thought from the beginning to be conducted in a still

water tank because of the available facilities and in order to keep it as fundamental as possible. With a current in the facility we would have also seen the effect of the boundary layer near the wall affecting the propulsion performance of the foil, which was not desired. Other authors Quinn et al. (2014b) have studied the effect of the boundary layer in a rigid panel with ground effect. The parameter space explored for this work ended up in more than 150 experimental cases summarised in Table 4.1.

d	0.25	0.3	0.38	0.45	0.55	1.54
θ_0	f (min : step : max)					
40°	1.5 : 0.5 : 5 (Hz)					
80°	1 : 0.5 : 4 (Hz)					
160°	0.5 : 0.5 : 4 (Hz)					
240°	0.5 : 0.5 : 3.3 (Hz)					

Table 4.1: Parameters of the experiment.

4.2.2 *Particle image velocimetry setup - fish tank*

In order to investigate the flow around the foil, Digital Particle Image Velocimetry (DPIV) was done to obtain two-dimensional velocity fields. DPIV data were acquired using a system based on a 20mJ Nd-YLF double pulse green laser that produced a planar light sheet, and a high-speed camera at full 1632×1200 pixel resolution, synchronised with the laser in order to capture the illuminated particle cloud images. The flow was seeded using 20 μm polyamide particles. A total of 2000 images were recorded for each experiment at a rate of 300, 350 or 400 images/second depending of the frequency of the foil oscillation. Before the velocity fields were calculated, the foil projection was removed from each image by applying a mask able to detect the outline of the foil at each instant in time. Two dimensional velocity fields were computed by applying a Fast Fourier Transform (FFT) based multipass window-

deformation technique (Willert and Gharib (1991)). The algorithm evaluated the images in two steps, first with an interrogation area of 64×64 pixels and after reducing the size of the window to 40×40 pixels, all with 50% overlap. Two different types of experiment were measured with DPIV. In some cases, the foil was allowed to move freely along the direction imposed by the rail of the air bearing system (free swimming configuration). In the other type of experiments, the foil was kept at a fixed position by locking the rail of the air bearing system (stationary foil configuration). All DPIV interrogations were made at an horizontal plane located at the middle of the foil's height. The laser was mounted in back part of the water tank, looking at the trailing edge of the foil (see Fig. 4.1b). The camera was placed below the tank looking upwards, covering a field of view of approximately 25 cm in the direction of motion and 12.6 cm transversely (see Fig. 4.1a).

4.3 RESULTS AND DISCUSSION

4.3.1 *Foil kinematics*

The undulation, tail amplitude and wavelength are influenced by the distance to the wall and play an important role in the type of the wake and in the swimming performance. In figure 4.3 the undulation kinematics of the foil is shown for two experiments: a case near the wall in Fig. 4.3(a), and a case with no influence of the wall in Fig. 4.3(b). It can be readily seen that the peak-to-peak lateral excursion of the tip is markedly influenced by the presence of the wall.

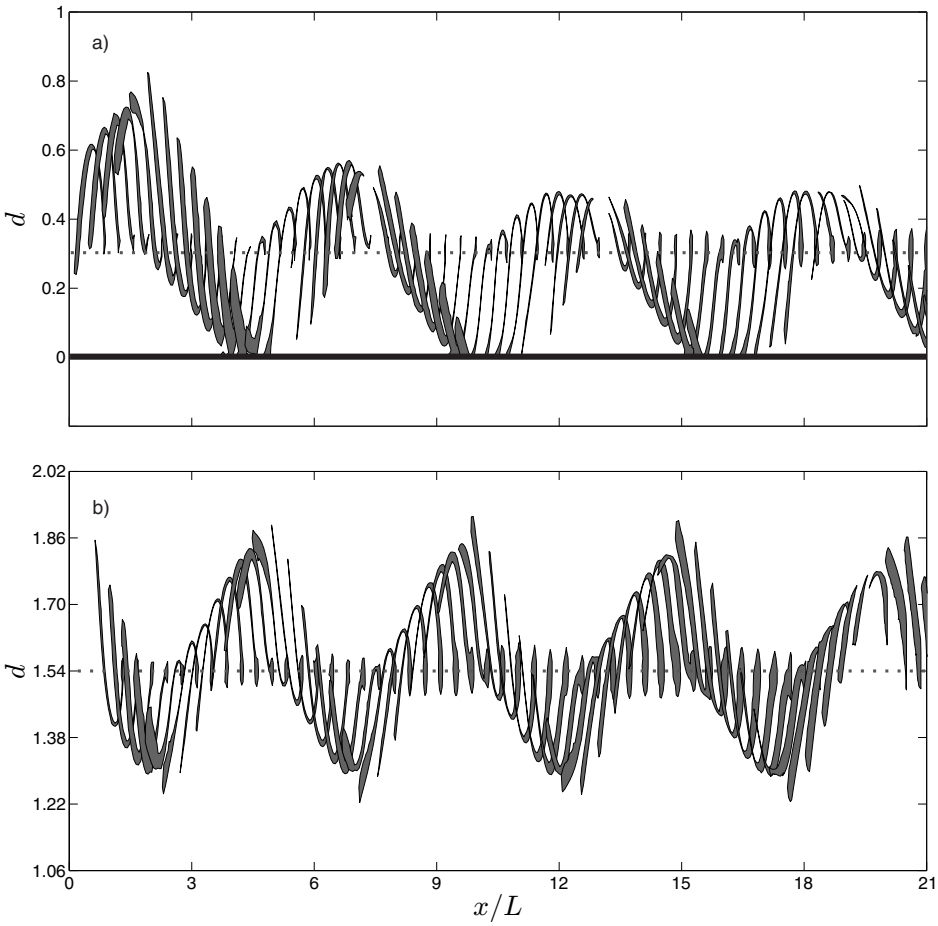

Figure 4.3: Sequence of motion of the foil for $\theta_0 = 160^\circ$ and $f = 1.5hz$ for two different distances to the wall (a) $d = 0.3$ and (b) 1.54. The foil swims from left to right. The dotted and black lines denote the swimming direction (the trace of the head of the foil) and the position of the wall, respectively.

The envelope of the trailing edge of the foil motion is obtained using the Hilbert transform of the time series of figure 4.3. This is shown in figure 4.4, where the top and bottom rows correspond to two different pitch amplitudes of 160° and 240° respectively, and each column corresponds to one of the three values of d shown previously in Fig. 4.3. The two cases with $\theta_0 = 160^\circ$ and 240° shown are the largest swept angles tested and they mimic the real motion of the backward-propagating

wave along an animal as Blevins and Lauder (2013), Blevins and Lauder (2012) and Rosenberger (2001). Each graph includes two different pitch frequencies. For both pitch amplitudes, the envelopes show larger amplitudes when the foil is far away from the wall as shown previously by Webb Webb (1993) and Webb (2002). For $\theta_0 = 240^\circ$ in figs. 4.4 (d), (e) and (f), envelopes practically do not vary with pitch frequency. On the other hand, for $\theta_0 = 160^\circ$, pitch at a higher frequency produces a smaller envelope amplitude if compared to the low frequency, see Figs. 4.4 (b) and (c). However, this is does not occur close to the wall —Figs. 4.4 (a)—, here the high frequency generates more amplitude than the low frequency. The ground effect can be noticed especially at the first peak of the envelope where the amplitude is always higher than the rest of the peaks of cycles as the following graphs a), b), d), and e).

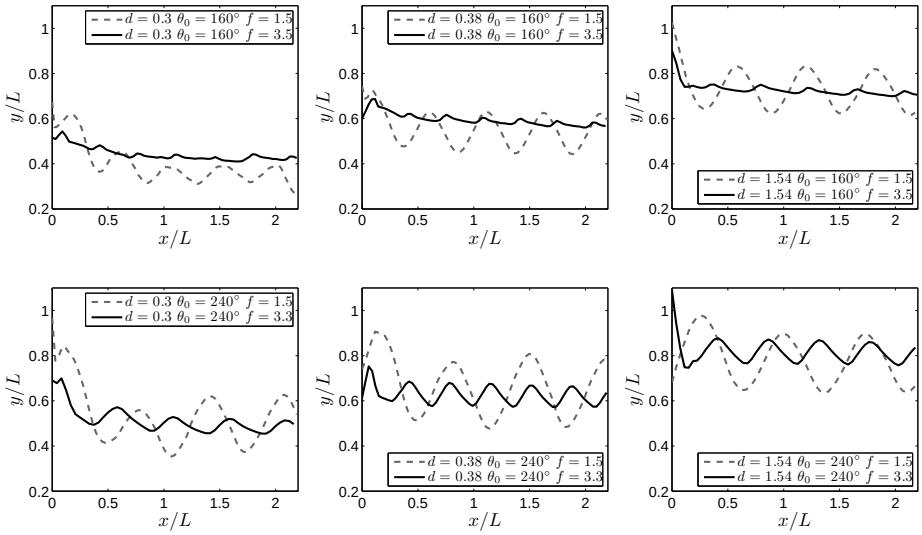

Figure 4.4: Envelopes of the trailing edge of the foil motion at difference distances to the wall: a) and d) d=0.3; b) and e) d=0.38; c) and f) d=1.54. Two different frequencies are plotted for two values of θ_0, 160° (a, b and c) and 240° (d, e and f).

4.3.2 *Propulsive force and cruise velocity*

The propulsive force F and the cruise velocity U are governed by the kinematics of the foil and the distance to the wall. The thrust force F produced by the foil was calculated from the displacement measurements $x(t)$ as in Raspa *et al.* Raspa et al. (2013, 2014). The measured displacement is fitted by the equation $x(t) = \frac{m}{\gamma} \log \left[\cosh \frac{\sqrt{\gamma F}}{m} t \right]$, which is the solution of $m\ddot{x} + \gamma \dot{x}^2 = F$. The latter equation represents a simplified dynamical model of the system in which $m\ddot{x}$ is the inertial term (with a total moving mass $m = 2.85$ kg including the body of the foil and its supporting system) and $\gamma \dot{x}^2$ is the hydrodynamic drag term. An iterative optimization process is applied to the analytical solution for $x(t)$, with γ and F as unknowns, until estimated and measured values of $x(t)$ converge.

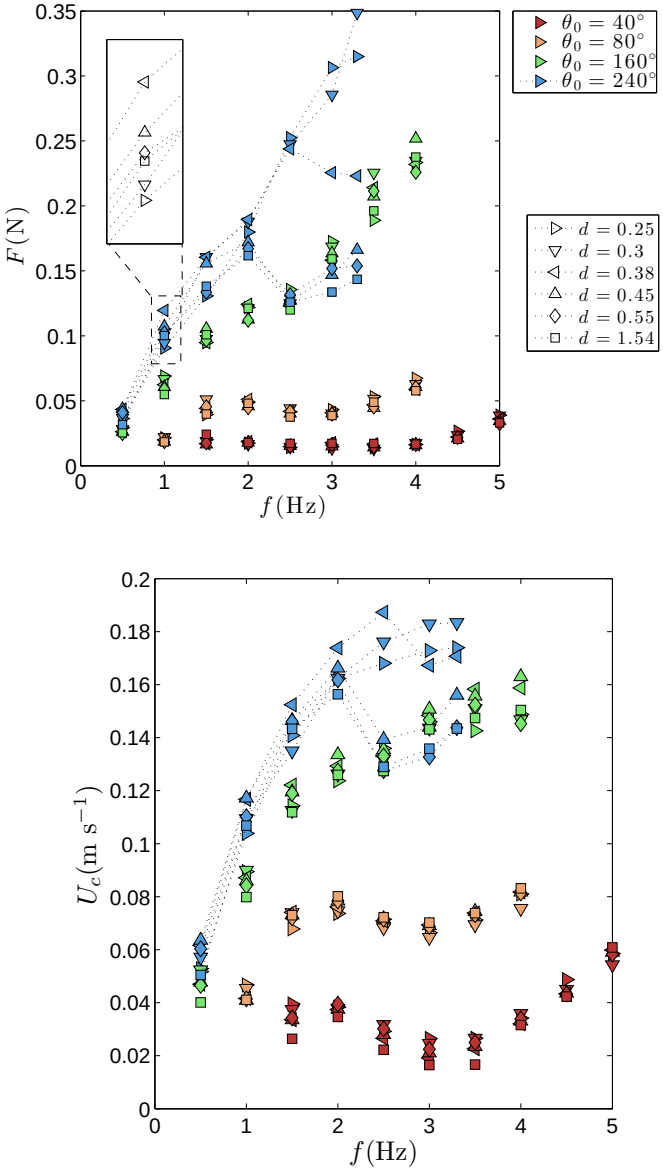

Figure 4.5: (a) Propulsive force (thrust) and (b) limit velocity (cruise velocity), versus frequency for different swept angles (40, 80, 160, 240 degrees) and distance to the wall (0.25, 0.3, 0.38, 0.45, 0.55 and 1.54). Dotted lines link the data points for each series corresponding to the 240 degrees forcing to guide the eye.

Performance is first analysed by studying how F and U_c behave as a function of the swept angle θ_0, the imposed pitch frequency f and the dimensionless distance to the wall d, see figure 4.5. In the figure, different symbols are used to identify distance to the wall, while colours denote the different amplitudes of the pitching oscillation imposed to the head of the foil. The first observation is that the four different sets of pitch amplitudes imposed to the foil, define four distinct branches of performance with respect to frequency. The higher the pitch amplitudes, the higher the swimming speed and the thrust produced. In the two branches corresponding to the smaller pitch amplitudes ($\theta_0 = 40^\circ$ and 80°), the effect of increasing pitch frequency in thrust and cruise velocity is relatively mild, and one recognises the shape of the curves reported in previous studies, with a slight peak that corresponds to a resonant behaviour with one of the deformation modes of the foil Raspa et al. (2014); Quinn et al. (2014a); Paraz et al. (2014). But when the imposed pitch is large ($\theta_0 = 160^\circ$ and especially 240°), the effect of the forcing frequency is crucial: increasing frequency not only determines more rapid increases in thrust and cruising speed, but also determines that the effect of the proximity to the wall, which was undetectable for the lower amplitudes, appears now as an important element for swimming performance.

Considering that the hydrodynamic thrust force at these large Reynolds numbers is expected to scale as the dynamic pressure acting on the propulsive element, the U_c and F data can be plotted together as $F \propto U_c^2$ – see Fig. 4.6(a)-, where the area of the foil $a = sL$ and the fluid density ρ have been used in order to obtain a dimensionless thrust coefficient

$$C_T = \frac{2F}{\rho U_c^2 a} \,. \tag{4.1}$$

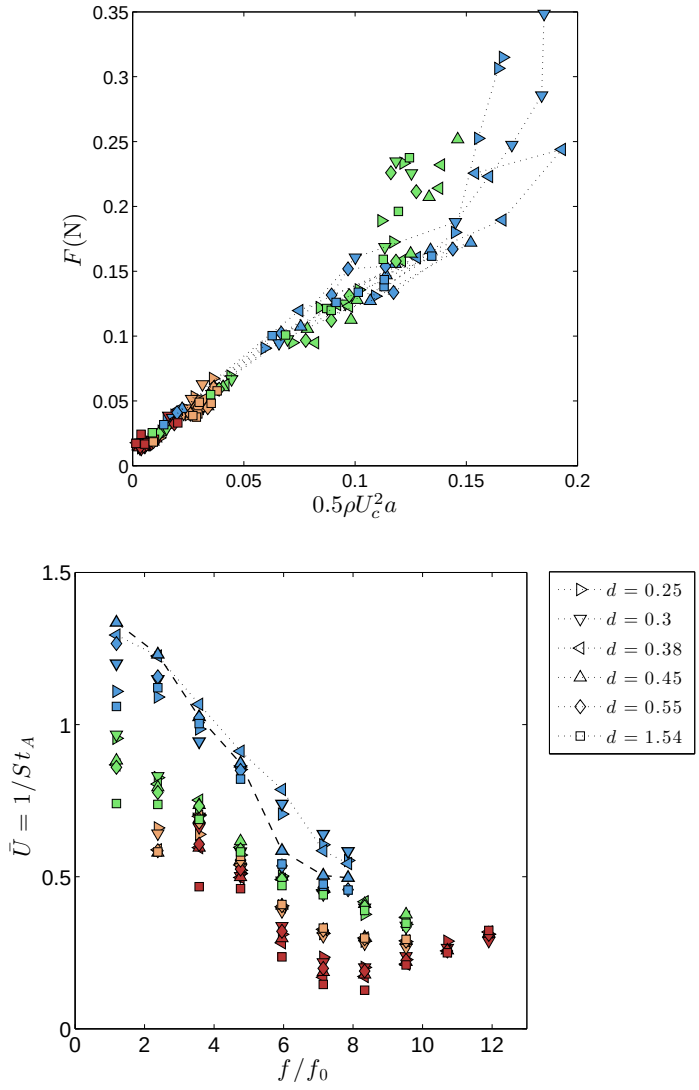

Figure 4.6: (a) F vs. U_c^2 and (b) reduced velocity $\bar{U} = U_c/fA$ as a function of the dimensionless excitation frequency f/f_0 for the same data as figure 4.5 .

The dashed line whose slope is an estimate of the average thrust coefficient was obtained as a linear fit of the data corresponding to $\theta_0 = 80°$. It can be seen that while the case of smaller pitching amplitudes ($\theta_0 = 40°$) is well described also by this fit, the series corresponding to $\theta_0 = 160°$

and $\theta_0 = 240^\circ$ deviate notably from the fit roughly for the upper half of the propulsive force range explored in the present experiments. The previous observation is not surprising, since the large amplitude pitching excitation at $\theta_0 = 160^\circ$ and 240° produces large deformations of the foil, most likely modifying significantly the coefficient of the quadratic drag model used here. Moreover, it is clear from this figure that the proximity to the wall plays thus an important role in the balance of thrust and drag, producing non-trivial behaviours at the large amplitude cases. Figure 4.6(b) presents another usual way of analysing the self-propelled swimming velocity by means of the reduced velocity $\bar{U} = U_c/fA$, a dimensionless parameter measuring the ratio of swimming speed to a flapping characteristic speed $f \times A$. Here $A = L\sin(\theta_0)$ is the amplitude of the imposed flapping motion. We note that $\bar{U}$ is the inverse of the Strouhal number St_A and is related to a "mechanical efficiency" of the flapping motion. This representation, however, brings no direct clarification to the role of the proximity to the wall in the scatter of the different data series.

4.3.3 *Wall effect on swimming velocity*

The effect of the distance to the wall can of course be examined directly comparing the different force or velocity curves in figure 4.5 as a function of d, for each pitching frequency. When the imposed pitch is small ($\theta_0 = 40^\circ$ and 80°), the ground effect is negligible, and all curves collapse over a common curve for each amplitude. But if the pitch amplitude is increased, swimming near or far away from the wall has a dramatic effect on the thrust and on the cruising velocity. The zoomed region in figure 4.5(a) permits to examine as an example the thrust for a foil forced at $\theta_0 = 240$ and $f = 1$ Hz. The maximum value is produced for a distance to the wall $d = 0.38$ followed by $d = 0.45$, indicating the ground effect is positive. If the distance is too large ($d \geq 0.55$) the wall effect starts to be of less importance, becoming negligible at a distance of $d = 1.54$, with thrust points collapsing on the same values. This behaviour is in agreement with the observations of Blevins and Lauder (2013). On the other hand, for distances to the wall $d \leq 0.3$ the ground

effect is negative for thrust. The other notable feature at the largest imposed pitch, $\theta_0 = 240^\circ$, is the sudden drop in velocity and thrust when the pitch frequency is set to values larger than 1.5 Hz and the foil is at distances to the wall larger than $d = 0.45$. The analysis of velocity fields in the next section will be useful to understand this observation.

Figure 4.7 shows an alternative way of looking at the results, by plotting the cruising speed normalised by its value $U_{c-\text{bulk}}$ away from the wall (i.e. swimming in the bulk). We focus now on the cases where the effect of the wall is significant which are those corresponding to $\theta_0 = 160^\circ$ and $\theta_0 = 240^\circ$. The values of $U_c/U_{c-\text{bulk}}$ are plotted against f/f_0 for all cases in the the top panels of Fig. 4.7, the different markers corresponding to different distances to the wall. The two bottom panels of the figure show $U_c/U_{c-\text{bulk}}$ as a function of the normalised distance to the wall d, only for a few selected frequencies for clarity. Different behaviours are observed for the two different amplitudes analysed and the main features can be summarised as follows: (1) aside from a few exceptions the wall has an overall positive effect on swimming speed; (2) the optimal position with respect to the wall evolves as a function of the frequency and the two different amplitudes tested present different behaviours. For instance, for $\theta_0 = 160^\circ$ at the lowest frequency tested, the cases swimming closest to the wall $d = 0.25 - 0.3$ were the best performers, while for $\theta_0 = 240^\circ$ the best case was at $d = 0.45$; (3) the optimal distance for $\theta_0 = 240^\circ$ case presents a sharp change for frequencies higher than $f/f_0 \approx 5$, going from $d \approx 0.45$ down to $d \approx 0.3$.

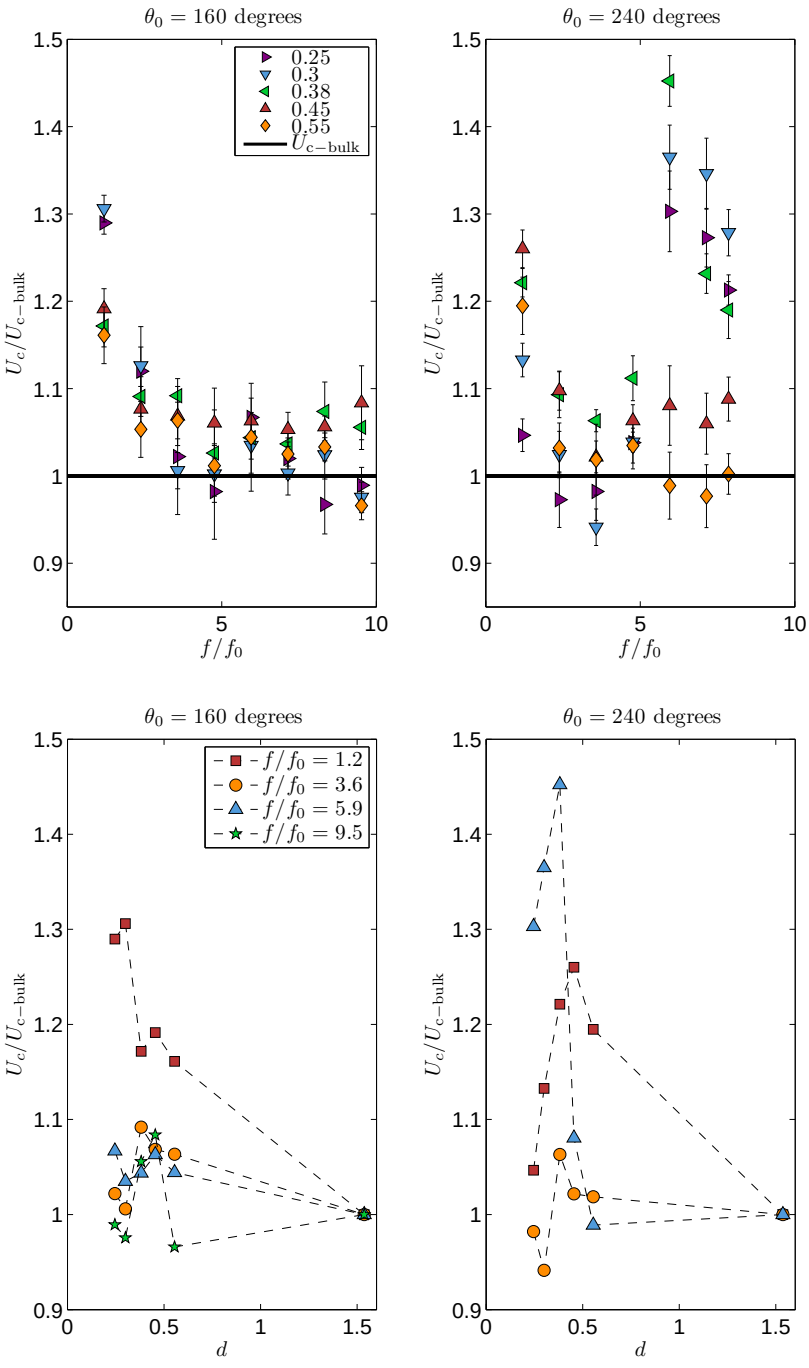

Figure 4.7: Cruising swimming velocity rendered dimensionless by normalising it with the cruising speed away from the wall U_{c-bulk} as a function of frequency and distance to the wall d (see legends).

In what follows we examine the velocity field around the swimming foils in order to pinpoint the fluid dynamical mechanisms responsible for the previous observations.

4.3.4 *DPIV analysis*

DPIV measurements were performed for two different foil configurations: Stationary swimming configuration (air bearing blocked), and self-propelled free swimming configuration (free to swim along the direction prescribed by the supporting air-bearing rail). DPIV was performed for the reference case without wall effect, and for selected cases with wall effect in which there was an enhancement of propulsion, as seen in section 4.3.2, that is for cases with large pitch motions and moderate distances to the wall. DPIV measurements of the stationary swimming configuration are used to obtain a global overview of the mean velocity fields, whilst in the free swimming configuration, the analysis is focused on the local instantaneous vorticity fields and the different wake topologies found behind the foil. DPIV data in all figures appear in dimensionless form, with velocities given by $(V_x, V_y) = (v_x, v_y)/fL$ and vorticities computed as $\omega_z L/U_c$.

4.3.4.1 *Stationary foil*

Contours of the mean velocity field are presented in figures 4.8 and 4.9, for the stationary foil. The streamwise component (V_x) appears in all these figures on the left column and the transverse velocity (V_y) on the right one. The figures are a good indication of the the momentum distribution in the wake.

Figure 4.8 is for an experiment with enhanced propulsion due to the wall effect (plots (a) and (b)) as seen in section 4.3.2 and without wall (plots (c) and (d)) for the $\theta_0 = 240^\circ$ case. The same arrangement of plots appears in figure 4.9 but for $\theta_0 = 160^\circ$. There are obvious differences introduced by the wall when comparing by rows the plots in both figures. Whilst in the cases without wall effect in the lower rows, the mean flow fields are typical of those of symmetric wakes Dewey et al. (2011),

the momentum distribution changes considerably by the effect of the wall, as seen in the upper row of both plots. Regions of high momentum directed along the propulsion direction appear near the wall in both figures, showing clearly one of the causes for propulsion enhancement.

4.3.4.2 *Self-propelled free foil*

In addition to the previous mean-flow analysis with the stationary foil, further insight on the mechanisms that govern the ground effect on swimming performance can be obtained by examining the cases with self-propulsion. In this section the foil is free to move along the rail of the air bearing and DPIV has been used to analyse the instantaneous flow patterns in the wake, depending on the main parameters governing the experiments (d, f and θ_0).

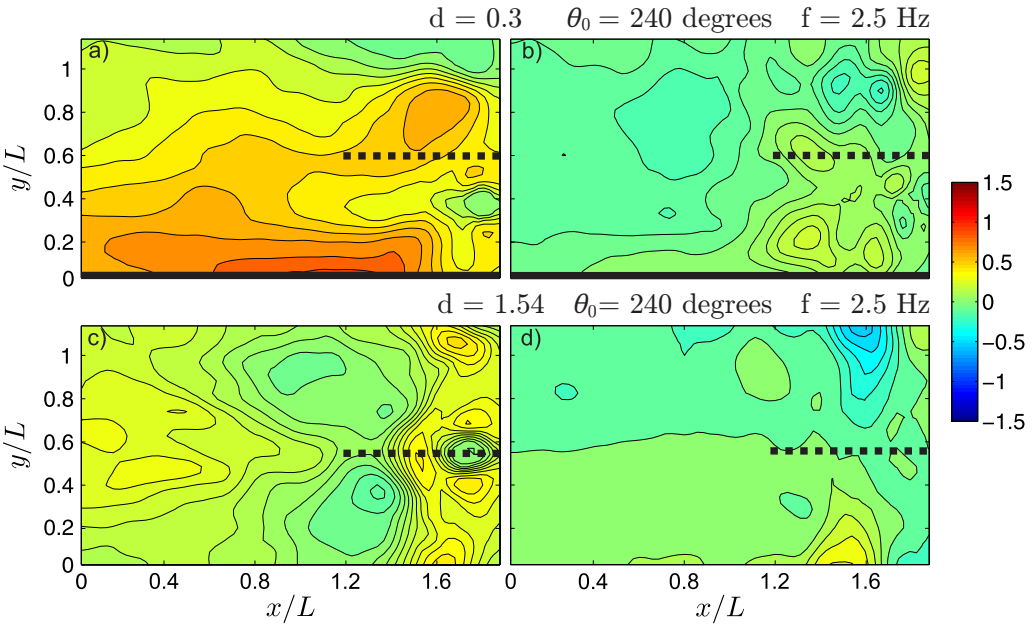

Figure 4.8: Average of the velocity fields, stream-wise $\bar{V}_x$ in the left column and cross-stream $\bar{V}_y$ on the right column for: (a) and (b) $d = 0.3$, $\theta_0 = 240°$ and $f = 2.5$ Hz; (c) and (d) $d = 1.54$, $\theta_0 = 240°$ and $f = 2.5$ Hz. Dashed black lines denote the position of the trailing edge of the foil and black thick lines represent the wall. The foil swims from left to right.

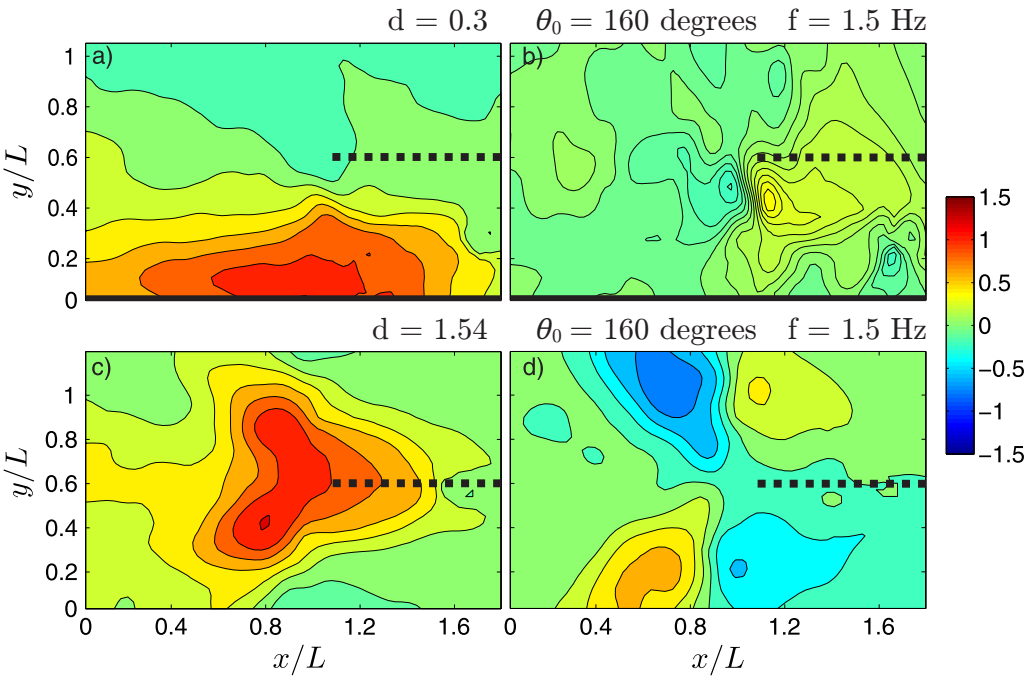

Figure 4.9: Average of the velocity fields, stream-wise $\bar{V}_x$ in the left column and cross-stream $\bar{V}_y$ on the right column for: (a) and (b) $d = 0.3$, $\theta_0 = 160^\circ$ and $f = 1.5$ Hz; (c) and (d) $d = 1.54$, $\theta_0 = 160^\circ$ and $f = 1.5$ Hz. Dashed black lines denote the position of the trailing edge of the foil and black thick lines represent the wall. The foil swims from left to right.

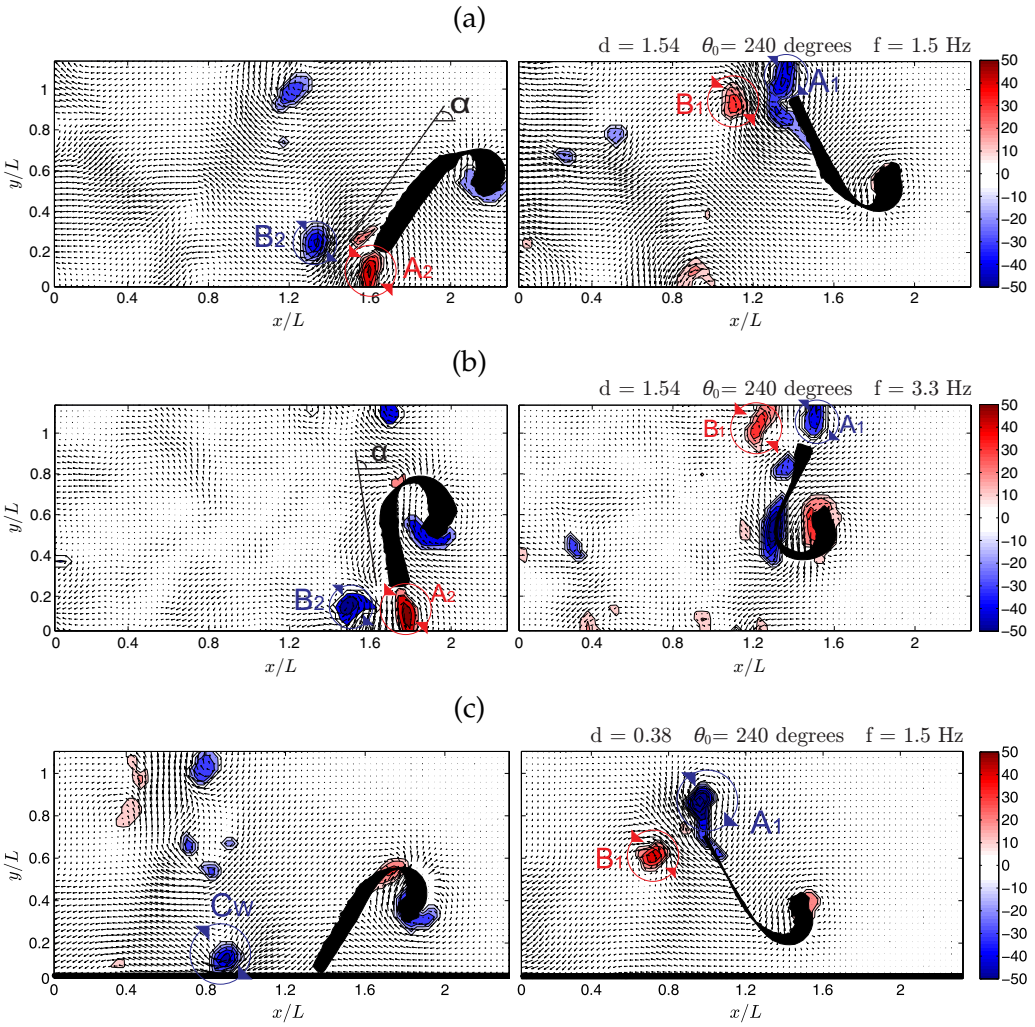

Figure 4.10: Instantaneous vorticity fields and velocity vectors for: (a) $d = 1.54$, $\theta_0 = 240$ degrees and $f = 1.5$Hz; (b) $d = 1.54$, $\theta_0 = 240$ degrees and $f = 3.3$Hz; and (c) $d = 0.38$, $\theta_0 = 240$ degrees and $f = 1.5$Hz. Snapshots at 0% and 50% of the cycle are shown on the left and right plots of each row, respectively. The foil swims from left to right. The thick black lines at the bottom in (c) denote the wall. Vorticity colour maps are overlaid on top of the vector velocity field generated by the foil. Blue is used for clockwise vorticity and red is for counter-clockwise.

A nomenclature based on that proposed by Williamson and Roshko Williamson and Roshko (1988) to describe the flow structures in the

wake of cylinders, is used here to describe the topology of the wake downstream the foil. According to this way of describing wakes, an S is used to denote a single vortex at one side of the wake per shedding cycle. If a P is used, the wake consists of a pair of counter-rotating vortices at one side per shedding cycle. If the same arrangement of vortices is observed at each side of the wake each cycle, a 2 is placed in front of the S or the P. Therefore a $2S$ wake is a wake consisting of a single vortex shed at each side of the wake and a $2P$ is a wake made of a pair of counter-rotating vortices at each side. When the observed pattern is different at both sides of the wake, a combination is needed and the symbol $+$ is used. For instance a $P+S$ wake consists of a single vortex in one side and a pair of vortices in the other. In our experiment if there is a combination, the first character before the $+$ symbol denotes the structure observed at the side of the wake without wall, and the second one, after the $+$ indicates the structure at the side of the wall. If the pair of vortices in the P structure is co-rotating, P^* is used.

The patterns observed in the wake of the foil far away from the wall ($d = 1.54$, where the wall effect is negligible), are summarised in table 4.2 for pitch motions of $\theta_0 = 160^\circ$ and 240° and 3 pitch frequencies. For the case with $\theta_0 = 240^\circ$, the dominant structure in the wake is the $2P$, a pair of counter-rotating vortices at each side of the wake, as observed in figures 4.10(a) and 4.10(b) with pitch frequencies of 1.5 and 3.3 Hz respectively. The two vortices in the $2P$ mode are denoted using capital letters and a subscript to indicate each side of the wake, hence A_1 and B_1 are the vortices at one side of the wake and A_2 and B_2 are the two vortices at the other side. The figure shows two different instants in time separated half a cycle. For $\theta_0 = 160^\circ$, when the foil is far away from the wall ($d = 1.54$), the $2P$ only appears at the lowest frequency — vorticity field not shown here but similar to figure 4.10(a)—. For higher frequencies $2S$ and $2P^*$ wakes are developed, as shown in figure 4.11: (a) $2S$ wake with vortices A_1 and A_2 at each side of the wake, and (b) $2P^*$ wake with two co-rotating vortices at each side of the wake, A_1 and B_1 at the upper half and A_2 and B_2 in the lower part.

d=1.54	$\theta_0 = 160°$	$\theta_0 = 240°$
1.5 Hz	$2P$	$2P$
2.5 Hz	$2S$	$2P$
3.5 Hz	$2P^*$	$2P$

Table 4.2: Summary of vortex modes found in the experiments in which the wall effect was not important

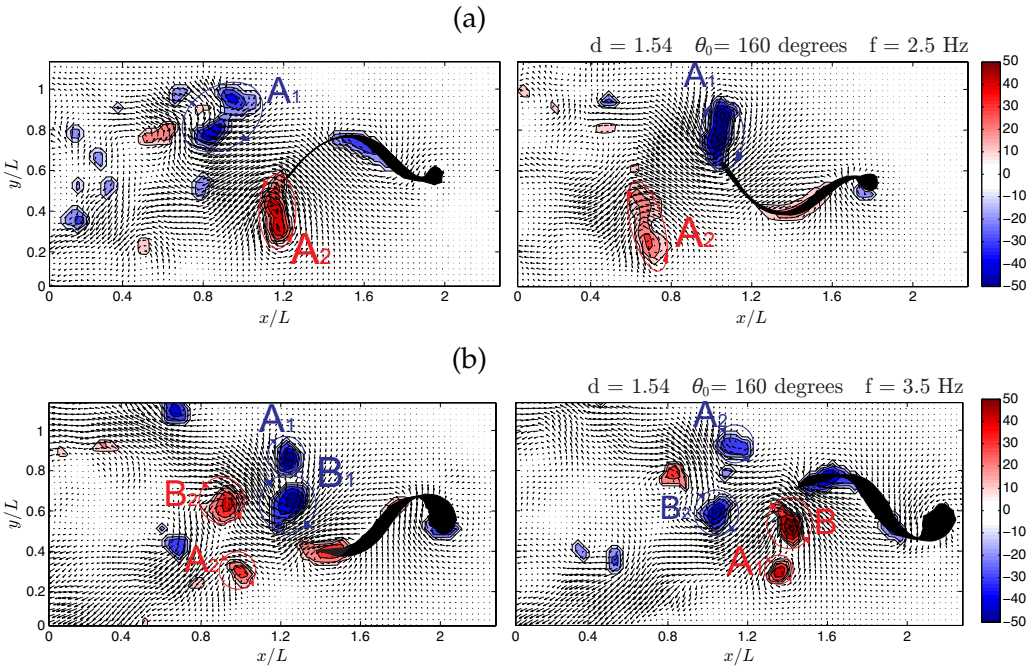

Figure 4.11: Instantaneous vorticity fields and velocity vectors for: (a) $d = 1.54$, $\theta_0 = 160$ degrees and $f = 2.5$Hz; and (b) $d = 1.54$, $\theta_0 = 160$ degrees and $f = 3.5$Hz. Snapshots at 0% and 50% of the cycle are shown on the left and right plots of each row, respectively. Other data as in Fig. 4.10.

We now describe the vortex wakes observed when the foil is closer to the wall, which are summarised in table 4.3, focusing on the cases where propulsion was improved: first the case of $\theta_0 = 240°$ and $d = 0.38$ and then $\theta_0 = 160°$ and $d = 0.3$. In both cases the same pitch frequencies

Freq	$\theta_0 = 160°$ d=0.3	$\theta_0 = 240°$ d=0.38
1.5 Hz	$P+S$	$P+S$
2.5 Hz	$S+P$	$P+S$
3.5 Hz	P^*+S	$P+S$

Table 4.3: Summary of vortex modes found in the experiments in which the wall effect was important.

are reported for comparison with the cases presented in table 4.2 without wall. The patterns are hybrid modes and show complex structures because of the effect of the wall. With the largest pitch amplitude, a $P+S$ structure was observed independently of the pitch frequency. A case showing this $P+S$ structure for $\theta_0 = 240°$, $f = 3.5$ Hz and a dimensionless distance to the wall of $d = 0.38$ appears in figure 4.10(c), with vortices A_1 and B_1 in the upper part of the plot and a single vortex C_w at the side of the wake near the wall. The $2P$ structure observed without wall has now changed to a $P+S$ structure if the wall is near the foil. That is, the counter-rotating vortex pair that was observed at the lower part of the measurement window for the case without wall changes to a single vortex C_w that is pushed vigorously downstream due to the existence of a high momentum jet-like region near the wall. This is readily seen in figure 4.10(c) by observing the distance at which C_w is located respect to the trailing edge of the foil, compared to the distance of the vortex pair A_2 and B_2 in figure 4.10(a).

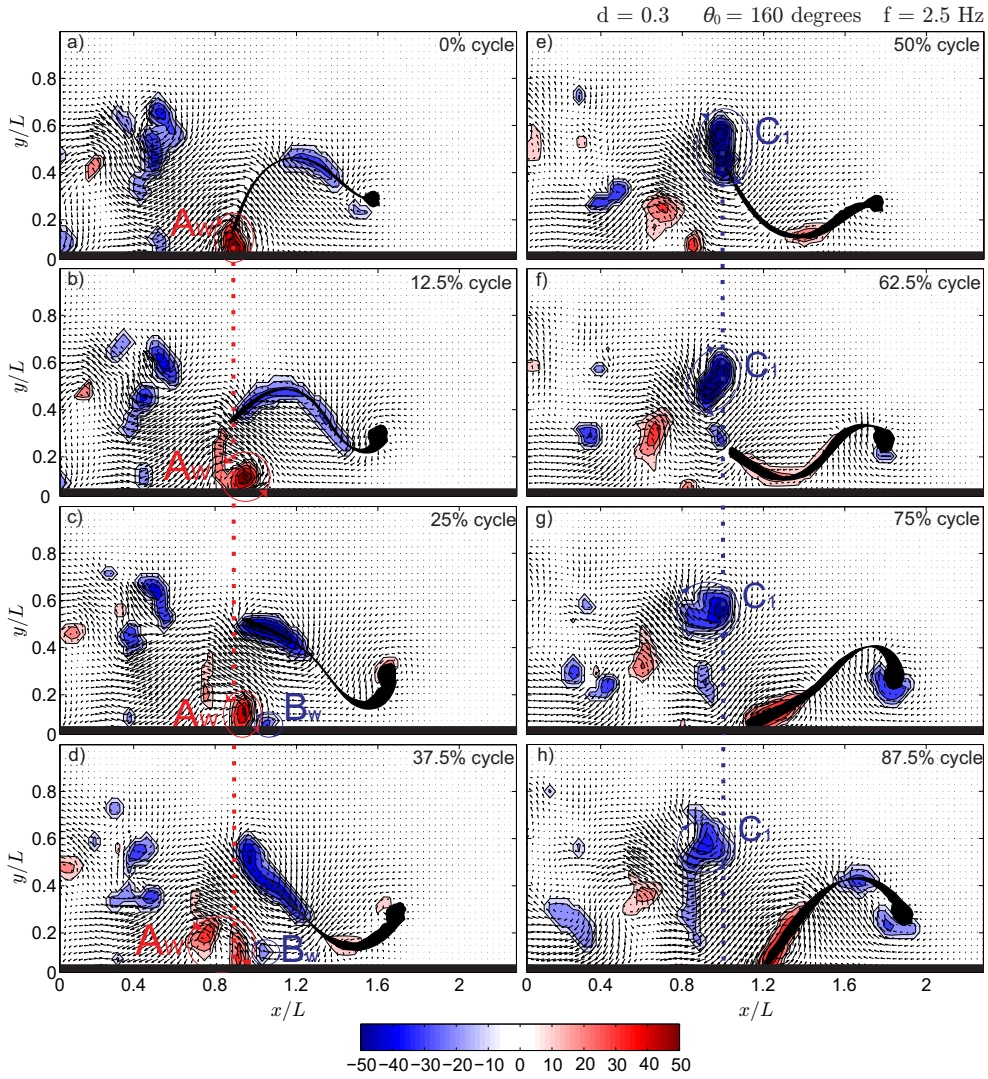

Figure 4.12: Sequence of instantaneous vorticity fields and velocity vectors. Every 20 frames is presented (Δt=50 ms) for $d = 0.3$, $\theta_0 = 160$ degrees and $f = 2.5$Hz. The foil swims from left to right and the black thick lines represent the wall at $y/L = 0$.

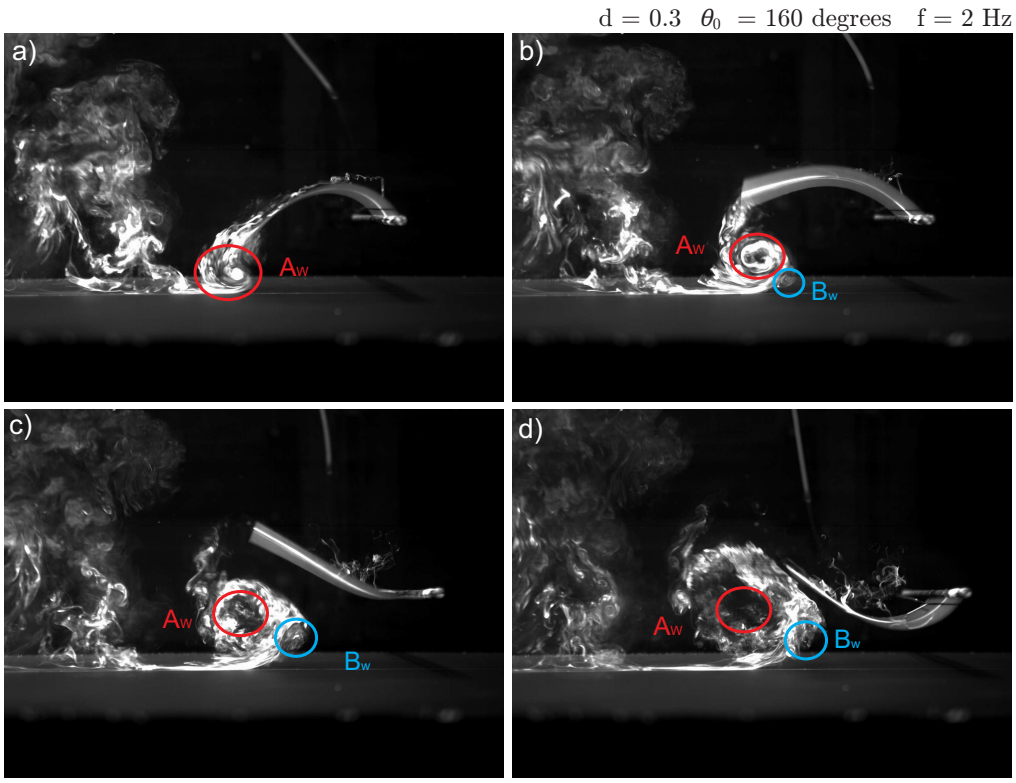

Figure 4.13: Flow visualization with fluorescein dye injection and a laser sheet of the vortex structures near the wall effects for $d = 0.3$, $\theta_0 = 160$ degrees and $f = 2$Hz. The time lapse between frames is $\Delta t = 250$ ms) and the foil moves from left to right.

With the lower amplitude $\theta_0 = 160°$, the structures are clearly dependent on the distance to the wall. At the lowest frequency the $P + S$ is the dominant structure and at a frequency of 2.5 Hz the $S + P$ structure is seen. Figure 4.12 presents a sequence of 8 DPIV snapshots covering a full pitching cycle for the latter case with the foil at a dimensionless distance to the wall of $d = 0.3$. At the wall side, a single vortex is shed from the foil (A_w) which eventually splits forming another structure B_w because of the proximity to the wall. In the other side of the wake a single vortex C_1, forms the $S + P$ mode in the wake. The flow visualisation with fluorescein-dye presented in figure 4.13 confirms this latter obser-

vation and the existence of this counter-rotating vortex pair (A_w and B_w) at the side of the wall.

The enhancement in propulsion observed in the thrust and velocity measurements presented above can thus be related to clear changes in the vortex dynamics in the wake of the foil. Whilst at the largest pitch amplitudes the main structure was a $2P$, with ground effect the dominant structure becomes a $P + S$. Now, if the pitch swept angle is 160° the structures are modified to combinations of single and a pair of vortices.

One of the important features observed in the thrust and velocity figures of section 4.3.2, is the dramatic drop in thrust and foil velocity that takes place at the largest pitch angle as the frequency of pitch is increased. The explanation for that phenomena is clear from figures 4.10(a) and 4.10(b) where it can be seen how without the wall, the increase in frequency yields a large change in the angle (α in the figures) at which the shedding of vortices occur, showing that the momentum distribution in the wake becomes less beneficial to the direction of swimming. If the foil is near a wall, the result is a change in this momentum distribution that enhances propulsion: this can be seen comparing 4.10(a) and 4.10(c), where without wall, vortices A_1 and B_1 remain unchanged, but with the wall the disappearance of A_2 and B_2 to form C_w, indicates less energy is dissipated in the wake and a higher-momentum jet-like structure is produced near the wall. This more beneficial momentum distribution was also pointed out in the analysis of the averaged flow fields presented for the stationary configuration in section 4.3.4.1.

4.3.5 *SPOD analysis*

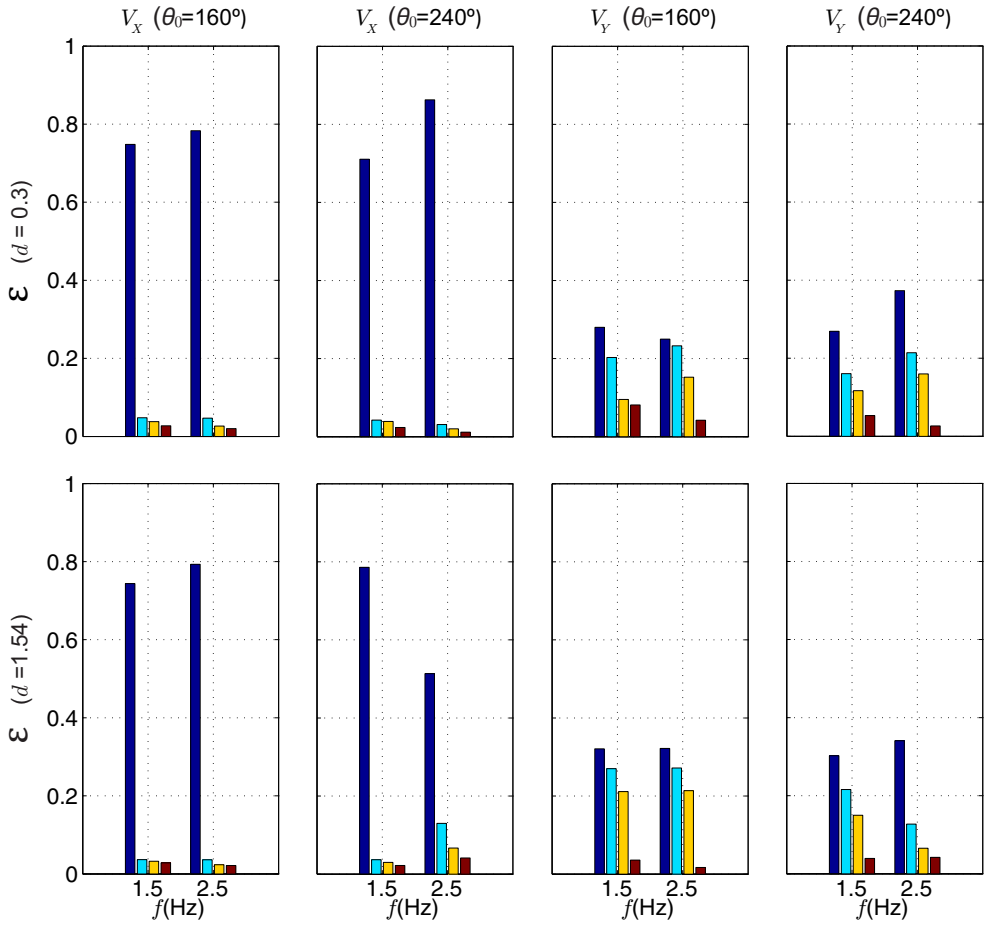

Figure 4.14: POD kinetic energy V_x and V_y of the first four modes (ordered from high to less energy from left to right on each plot) versus frequency (1.5 and 2.5 Hz). First row for $d = 0.3$ and second row for $d = 1.54$. First and second columns stream-wise velocity and the third and four columns for cross-stream velocity.

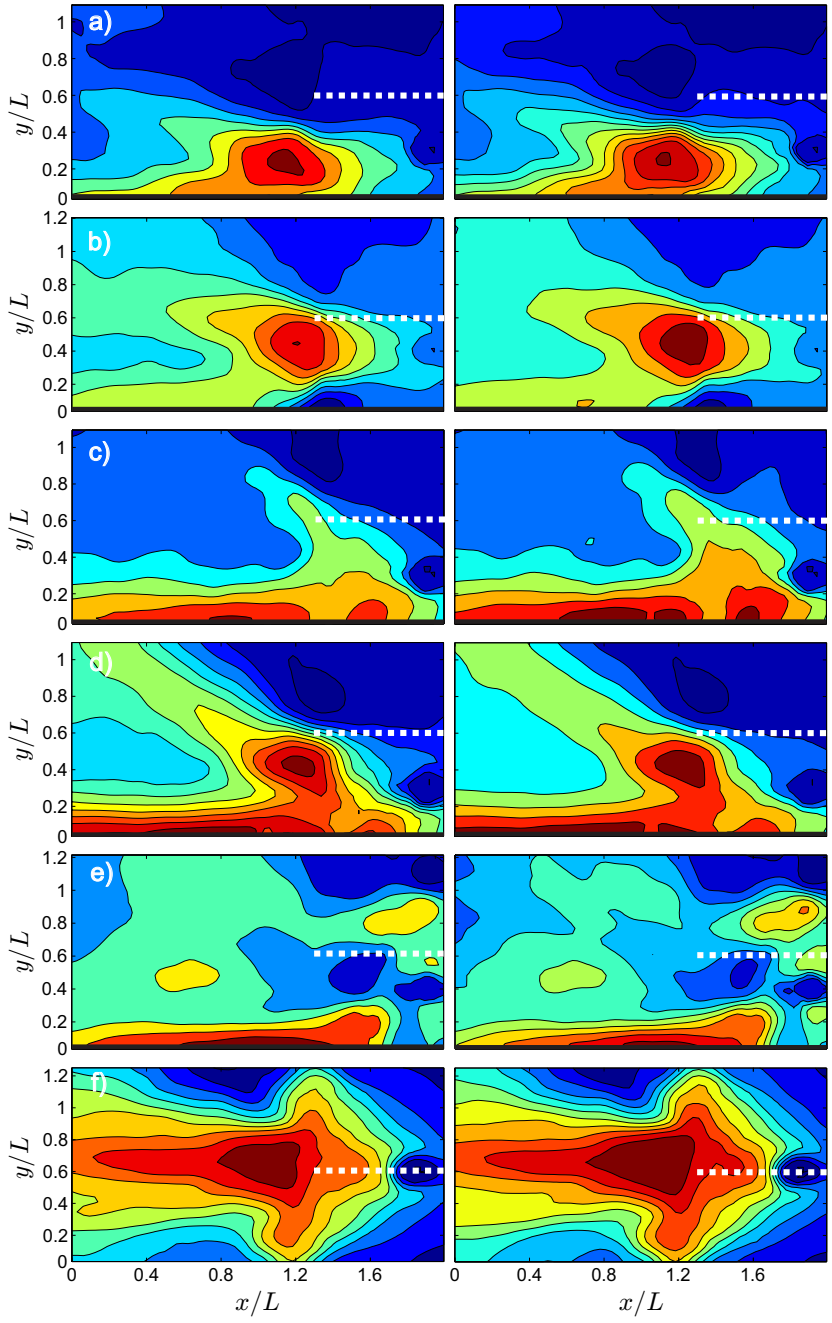

Figure 4.15: Comparison first POD mode (left column) and average of velocity fields (right column) for the stream-wise direction. a) $d = 0.3$, $\theta_0 = 160$ degrees and $f = 2$Hz b) $d = 0.38$, $\theta_0 = 160$ degrees and $f = 3$Hz c) $d = 0.3$, $\theta_0 = 240$ degrees and $f = 1.5$Hz d) $d = 0.3$, $\theta_0 = 240$ degrees and $f = 2.5$Hz e) $d = 0.38$, $\theta_0 = 240$ degrees and $f = 3$Hz f) $d = 1.54$, $\theta_0 = 240$ degrees and $f = 1.5$Hz. Dashed white lines denote the position of the trailing edge of the foil and black thick lines represent the wall. The foil swims from left to right.

Snapshot Proper Orthogonal Decomposition (SPOD) Sirovich (1987) has been applied to the velocity DPIV data, following the technique described by Huera-Huarte et al. Huera-Huarte and Vernet (2009) and recalled in Appendix I. Assuming that the fluctuating part of the flow can be represented by linear combinations of POD modes $\phi_i(x,y)$ and time varying modal coefficients $a_i(t)$,

$$V(x,y,t) = \bar{V}(x,y) + \sum_{i=1}^{M} a_i(t)\phi_i(x,y) \tag{4.2}$$

the SPOD technique permits to study the kinetic energy (ε) distribution of the flow into the most important modes. The ε associated to the first four more energetic POD modes is shown in figure 4.14, for both stream-wise and cross-flow components of the velocity. Two different dimensionless distances to the wall ($0.3W$ and $1.54W$) appear in the figure, for two pitch amplitudes (160 and 240 degrees), and two pitch frequencies (1.5 and 2.5 Hz). The figure shows how the ε is mostly concentrated in the first POD mode of the streamwise direction in all cases, with more than 70%. In the cross-flow component, the energy is shared more uniformly mainly between the first three POD modes.

The decrease in thrust and propulsive velocity observed (Fig. 4.5) for the $\theta_0 = 240^\circ$ case at frequencies higher than 2 Hz when the foil is away from the wall can also be explained through the POD analysis. Indeed, for frequencies higher than 2 Hz, since the momentum structure in the wake is then directed mostly perpendicularly to the swimming direction, the first POD mode at 2.5 Hz has dropped considerably if compared to the 1.5 Hz case (see second row and column in Fig. 4.14). Another point that can be seen is that, while for $\theta_0 = 160^\circ$ the energy of the different modes does not change noticeably when increasing the driving frequency, for $\theta_0 = 240^\circ$ on the contrary, the energy in the first POD mode does increase with frequency when the wall is present. The latter reflecting our previous observation that at these large angles the foil is diverting the momentum in a direction perpendicular to the propulsion direction and the presence of the wall reorients momentum favourably.

Figure 4.15 compares the first streamwise POD mode (left column) and the average stream-wise velocity fields (right column) of the same

cases. The trailing edge of the foil in its rest position is shown in the plots with a dashed white line for the sake of clarity. The POD and the averaged velocity fields appear normalised by the maximum value in the cases shown, for comparison. The plots certify again how the first stream-wise mode is enough to represent the momentum in the wake.

UNIVERSITAT ROVIRA I VIRGILI
HYDRODYNAMICS OF PITCHING FOILS: FLEXIBILITY AND GROUND EFFECTS
Rafael Fernandez Prats
Dipòsit Legal: T 979-2015

5 CONCLUSIONS

In this chapter the most important conclusions based on the research presented in the thesis are summarized.

5.1 CONCLUSIONS

5.1.1 *Hydrodynamics of a rigid and flexible pitching foils*

Experiments combining hydrodynamic force measurements and velocity field interrogations, have been used to describe the performance of a rigid foil pitching in a current, in terms of thrust production and efficiency.

Very clear trends have been identified and physically explained by combining the analysis of the hydrodynamic forces and the wake structures in specific representative cases. In our experiments, it appears evident that flapping with moderate swept angles and frequencies yields the largest efficiencies, associated to a specific type of wake consisting of a main bound vortex shed when the foil changes direction and a series of smaller shear layer vortices. This configuration contributed to a momentum distribution in the wake better aligned to the propulsion direction, and therefore ended up producing higher thrust.

5.1.2 *Effect of chordwise flexibility on pitching plate propulsion*

In the range of flexural stiffness tested, we have found the optimum chordwise flexibility in terms of propulsion up to 69% of the hydrodynamic efficiency with the $semi - flexible$ foil at Reynolds numbers studies in the investigation. We have seen how the chordwise flexibility has a maximum peak point, after which the C_T drops, decreasing the efficiency. We can report a transition of thrust generation in the

semi − flexible foil with θ_0= 72 ° for all Reynolds numbers tested, where before the transition the performance of the *semi − flexible* foil was as the *semi − rigid* foil; however after the transition, the performance of the foil changed from the *semi − flexible* to the *flexible* foil. This transition of thrust generation was obtained between $0.4 \leq \mathrm{St} \leq 0.65$ really close to the range previously dictated by Triantafyllou et al. (1993) to maximize the thrust of a flapping foil. This transition of thrust generation was determined in the two analysis, load measurements with improvements of thrust and DPIV measurements, where regions of high velocities were wider and longer.

These results have an interesting observation from the point of view of a simple flapping robotic setup, where if the must is the generation of thrust, a flexural stiffness close to the *semi − rigid* foil should be chosen; however if the efficiency is the most important, a flexural stiffness close the the semi-flexible foil should be chosen.

5.1.3 *Large-amplitude undulatory swimming near a wall*

The experimental data presented in this work shows that swimming with large-amplitude undulatory motions at a moderate distance to a wall can have clear advantages in terms of velocity and thrust production. Positive ground (or wall) effect has been observed for the system presented here, when swimming with pitch motions of large amplitude ($\theta_0 = 160^\circ$ and 240°) and for distances to wall between 0.25 and 0.55 times the width (W) of the foil. Maximum improvements in velocity and thrust have been observed of about 25% and 45% respectively. The results also suggest that for distances of more than 1.5 widths of the foil, the ground effect can be neglected, fact also found by Blevins et al. Blevins and Lauder (2013). The fluid dynamical mechanisms behind this enhancement have been explored by investigating the flow field in the wake of foil, showing how the wall constrains the distribution of momentum in a direction favourable to propulsion. In addition to the analysis of the mean flow, which exhibits the constrained jet structure in the wake of the foil (Figs 4.8 and 4.9), the time-resolved vorticity fields

show the changes in the wake vortex topology associated to the enhancement of propulsion —e.g. Fig. 4.10 (a) and (c)—.

As a point of perspective we can comment on the three-dimensional structure of the wake. Although the hypothesis of quasi-two-dimensionality underlying our analysis (as well as that of most of the literature on simplified model foils) can be partially justified alluding to the aspect ratio of the propulsive appendage, it is clear that the inherent 3D nature of this type of flows needs to be further analysed and included in realistic models. With respect to the present results, in addition to the vortex structures in the xy-plane analysed here, the wall will also affect the stream-wise structures in the yz-plane which have been recently established as important players in the drag-thrust balance Raspa et al. (2014); Ehrenstein et al. (2014). These issues will be the subject of future work.

The results with the present flexible foil excited by a pitching oscillation at its head are in agreement with what has been reported for a foil with heaving excitation Quinn et al. (2014b). This is an interesting observation from the point of view of bio-inspired design, where pitching motions associated to the elastic response of an appendage could sometimes be an optimal solution to actuate a robotic setup.

UNIVERSITAT ROVIRA I VIRGILI
HYDRODYNAMICS OF PITCHING FOILS: FLEXIBILITY AND GROUND EFFECTS
Rafael Fernandez Prats
Dipòsit Legal: T 979-2015

APPENDIX I

Snapshot Proper Orthogonal Decomposition

A linear eigenvalue problem can be derived using the POD method. Let an ensemble of DPIV data $\mathbf{V}$, with N being the total number of the available flow fields or snapshots, arranged in column form i a way in which the first half of the columns are the streamwise velocities and the second one the cross-flow velocities,

$$\mathbf{V} = \left[\mathbf{v}^1\mathbf{v}^2...\mathbf{v}^N\right] \tag{.1}$$

and the fluctuating part of the flow is,

$$\mathbf{V} = \tilde{\mathbf{V}} - \bar{\mathbf{v}} = \tilde{\mathbf{V}} - \frac{1}{N}\sum_{n=1}^{N}\mathbf{v}^n \qquad n = 1, 2, ...N \tag{.2}$$

the eigenvalue formulation results in,

$$\mathbf{C}\mathbf{H}^i = \lambda^i\mathbf{H}^i \tag{.3}$$

where the matrix $\mathbf{C}$ is,

$$\mathbf{C} = \mathbf{V}^T\mathbf{V} \tag{.4}$$

The solution of equation .3 consists of N eigenvalues (λ^i) and the NxN modal matrix ($\mathbf{H}$), made of column eigenvectors ($\mathbf{H}^n$). The eigenvectors provide a basis to produce the POD modes,

$$\phi^i = \frac{\sum_{n=1}^{N} H_n^i\mathbf{v}^n}{||\sum_{n=1}^{N} H_n^i\mathbf{v}^n||}, \qquad i = 1, 2, ...N \tag{.5}$$

where $||\cdot||$ denotes p2-norm, and it is calculated as the square root of the summation of the squares of each component inside the brackets. The result of equation .5 is a set of N POD modes. As introduced in equation 4.2, the flow can be expressed as a linear combination of POD modes and POD coefficients,

$$\mathbf{v}^n = \sum_{n=1}^{N} a_i^n \mathbf{\Phi}^i = \mathbf{\Phi}\mathbf{a}^n \tag{.6}$$

hence, once the POD modes are available, the POD coefficients ($\mathbf{a}^n$) can be obtained,

$$\mathbf{a}^n = \mathbf{\Phi}^T \mathbf{v}^n \tag{.7}$$

This coefficients indicate how important is each POD mode in each time snapshot. The eigenvalues (λ^i), are proportional to the ε of the fluctuating part of the flow and by sorting them in a decreasing fashion, $\lambda^i > \lambda^{i+1}$ for $i = 1, ..., N-1$ the most energetically important POD modes in the flow can be identified. The relative ε associated to each POD mode can be calculated as,

$$\varepsilon_i = \frac{\lambda^i}{\sum_{n=1}^{N} \lambda^n} \tag{.8}$$

BIBLIOGRAPHY

Ahlborn, B., Chapman, S., Stafford, R., Blake, R. W., Harper, 1997. Experimental simulation of the thrust phases of fast-start swimming of fish. The journal of experimental Biology 2312, 2301–2312.

Alben, S., Oct. 2008. Optimal flexibility of a flapping appendage in an inviscid fluid. Journal of Fluid Mechanics 614, 355.

Alben, S., Shelley, M., 2005. Coherent locomotion as an attracting state for a free flapping body. Proceedings of the National Academy of Sciences of the United States of America 102 (32), 11163–6.

Alben, S., Witt, C., Baker, T., Anderson, E., Lauder, G., 2012. Dynamics of freely swimming flexible foils. Physics of Fluids 24, 051901.

Anderson, J., 1996. Vorticity control for efficient propulsion.

Anderson, J. M., Streitlien, K., Barrett, D. S., Triantafyllou, M. S., 1998. Oscillating foils of high propulsive efficiency. Journal of Fluid Mechanics 360, 41–72.

Barannyk, O., Bradley, J. B., Oshkai, P., 2012. On performance of an oscillating plate, underwater propulsion system with variable chordwise flexibility at different depths of submergence. Journal of Fluids and Structures 28 (7), 205–224.

Bergmann, M., Iollo, A., 2010. Modelling and simulation of fish-like swimming. Journal of Computacional Physics 230, 329–348.

Betz, A., 1912. Ein beitrag zur erklarung des segelfuges. Zeitschrift fur Flugtechnik und Motorluftschiffahrt.

Blake, R. W., 1983. Mechanics of gliding in birds with special reference to the influence of the ground effect. Journal of Biomechanics 16 (8), 649–654.

Blevins, E. L., Lauder, G. V., 2012. Rajiform locomotion: three-dimensional kinematics of the pectoral fin surface during swimming in the freshwater stingray Potamotrygon orbignyi. The Journal of Experimental Biology 215 (18), 3231–3241.

Blevins, E. L., Lauder, G. V., 2013. Swimming near the substrate: a simple robotic model of stingray locomotion. Bioinspiration & Biomimetics 8 (1), 016005.

Blondeaux, P., Fornarelli, F., Guglielmini, L., Triantafyllou, M. S., Verzicco, R., 2005. Numerical experiments on flapping foils mimicking fish-like locomotion. Physics of Fluids 17 (11), 113601.

Bose, N., 1995. Performance Of Chordwise Flexible Oscillating Propulsors Using A Time-Domain Panel Method. Int. Shipbuild. Progr 42, 281–294.

Bratt, J. B., 1953. Flow patterns in the wake of an oscillating aerofoil. Aero. Res. Counc. R. M. 2773, 1–28.

Buchholz, J. H. J., Smits, A. J., 2006. On the evolution of the wake structure produced by a low-aspect ratio pitching panel. Journal of Fluid Mechanics 546, 433–443.

Buchholz, J. H. J., Smits, A. J., 2008. The wake structure and thrust performance of a rigid low-aspect-ratio pitching panel. Journal of Fluids Mechanics 603, 331–365.

Cebeci, T., Platzer, M., Chen, H., Chang, K., Shao, J., 2005. Analysis of Low-Speed Unsteady Airfoil Flows. Springer, New York, NY, USA.

Chaithanya, M. R., Venkatraman, K., 2008. Hydrodinamic Propulsion of a Flexible Foil (August), 1–4.

Chandar, D. D. J., Damodaran, M., 2008. Computational Study of Unsteady Low-Reynolds-Number Airfoil Aerodynamics Using Moving Overlapping Meshes. AIAA Journal 46, 429–438.

Chopra, M. G., 1976. Large amplitude lunate-tail theory of fish locomotion. Journal of Fluid Mechanics 74, 161–182.

Combes, S. A., Daniel, T. L., 2001. Shape, flapping and flexion: wing and fin design for forward flight. Journal of Experimental Biology 204, 2073–2085.

Combes, S. A., Daniel, T. L., 2003a. Flexural stiffness in insect wings .I. Scaling and the influence of wing venation. Journal of Experimental Biology 206, 2979–2987.

Combes, S. A., Daniel, T. L., 2003b. Flexural stiffness in insect wings. II. Spatial distribution and dynamic wing bending. Journal of Experimental Biology 206, 2989–2997.

Cui, E., Zhang, X., 2010. Ground effect aerodynamics. Encyclopedia of Aerospace Engineering,.

Dewey, P. A., Boschitsch, B. M., Moored, K. W., Stone, H. A., Smits, A. J., 2013. Scaling laws for the thrust production of flexible pitching panels. Journal of Fluid Mechanics.

Dewey, P. A., Carriou, A., Smits, A. J., 2011. On the relationship between efficiency and wake structure of a batoid-inspired oscillating fin. Journal of Fluid Mechanics 691 (1), 245–266.

Dong, H., Mittal, R., Bozhurttas, M., Najjar, F., 2005. Wake structure and performance of finite aspect-ratio flapping foils. 43rd AIAA Aerospace Sciences meetting and exhibit.

Dong, H., Mittal, R., Najjar, F. M., 2006. Wake topology and hydrodynamic performance of low-aspect-ratio flapping foils. Journal of Fluid Mechanics 566, 309343.

Drucker, E. G., Lauder, G. V., 1999. Locomotor forces on a swimming fish: three-dimensional vortex wake dynamics quantified using digital particle image velocimetry. The Journal of Experimental Biology 202, 2396–2412.

Drucker, E. G., Lauder, G. V., 2000. A hydrodynamic analysis of fish swimming speed: wake structure and locomotor force in slow and fast labriform swimmers. The Journal of Experimental Biology 203, 2379–2393.

Drucker, E. G., Lauder, G. V., 2002. Forces, fishes, and fluids: hydrodynamic mechanisms of aquatic locomotion. News Physiol. Sci. 17, 235–240.

Du, G., Sun, M., Jul. 2008. Effects of unsteady deformation of flapping wing on its aerodynamic forces. Applied Mathematics and Mechanics 29 (6), 731–743.

Du, G., Sun, M., Jul. 2010. Effects of wing deformation on aerodynamic forces in hovering hoverflies. The Journal of experimental biology 213 (Pt 13), 2273–83.

Eaton, R. C., Emberley, D. S., 1991. How stimulus direction determines the trajectory of the Mauthner-initiated escape response in a teleost fish. Journal of Experimental Biology 161 (1), 469–487.

Ehrenstein, U., Marquillie, M., , C., E., 2014. Skin friction on a flapping plate in uniform flow. Phil. Trans. R. Soc. A -, In press.

Ellenrieder, K. D. V., Parker, K., Soria, J., 2003. Flow structures behind a heaving and pitching finite-span wing. Journal of Fluids Mechanics 490, 129–138.

Ellington, C. P., 1984. The Aerodynamics of Hovering Insect Flight. Philosophical Transactions of the Royal Society of London B 305, 1–181.

Ellington, C. P., van den Berg C Willmott A P, Thomas, A. L. R., 1996. Leading-edge vortices in insect flight. Nature 384, 626–630.

Eloy, C., 2012. Optimal Strouhal number for swimming animals. Journal of Fluids and Structures 30, 205–218.

Fernandez-Prats, R., Huera-Huarte, F., 2014. Hydrodynamic forces and DPIV on a towed pitching foil. ASME 2014 4th Joint US-European Fluids Engineering Division Summer Meeting, FEDSM 2014, 1–7.

Fernández-Prats, R., Raspa, V., Thiria, B., Huera-Huarte, F., Godoy-Diana, R., Jan. 2015. Large-amplitude undulatory swimming near a wall. Bioinspiration & biomimetics 10 (1), 016003.
URL http://www.ncbi.nlm.nih.gov/pubmed/25561330

Garrick, I., 1937. Propulsion of a flapping and oscillationg airfoil. NACA Report No. 567, 419–427.

Gazzola, M., Argentina, M., Mahadevan, L., Sep. 2014. Scaling macroscopic aquatic locomotion. Nature Physics 10 (10), 758–761.

Godoy-Diana, R., Aider, J. L., Wesfreid, J. E., 2008. Transitions in the wake of a flapping foil. Physical Review E 77 (1), 016308.

Gopalkrishnan, R., Triantafyllou, M. S., Triantafyllou, G. S., Barrett, D., Apr. 1994. Active vorticity control in a shear flow using a flapping foil. Journal of Fluid Mechanics 274 (-1), 1.

Green, M. A., Rowley, C. W., Smits, A. J., 2011. The unsteady three-dimensional wake produced by a trapezoidal pitching panel. Journal of Fluids Mechanics 685, 117–145.

Green, M. A., Smits, A. J., 2008. Effects of the three-dimensionality on thrust production by a pitching panel. Journal of Fluids Mechanics 615, 211–220.

Guglielmini, L., 2004. Modelling of thrust generating foils. Phd thesis, University of Genoa.

Gulcat, U., 2009. Propulsive Force of a Flexible Flapping Thin Airfoil. Journal of Aircraft 46 (2), 465–473.

Hainsworth, F. R., 1988. Induced drag savings from ground effect and formation flight in brown pelicans. Journal of Experimental Biology 135 (1), 431–444.

Heathcote, S., Gursul, I., 2004. Flexible flapping airfoil propulsion at Zero Freestream Velocity. AIAA Journal 42, 2196–2204.

Heathcote, S., Gursul, I., 2007a. Flexible flapping airfoil propulsion at low Reynolds numbers. AIAA Journal 45, 1066–1079.

Heathcote, S., Gursul, I., 2007b. Flexible flapping airfoil propulsion at low Reynolds numbers. Journal of Fluids and Structures 45, 1066–1079.

Hobson, B., Kemp, M., , Leonessa, A., 2002. Integration of a hovering module with the Morpheus AUV: application to MCM missions. Oceans 2002 MTS/IEEE, 207–209.

Hobson, B., Kemp, M., Carolina, N., Goff, I. L., Leonessa, A., 2003. Oscillating Fin Thrusters For Multi-View Classification Maneuvering On MCM UUVS, 2167–2169.

Hover, F. S., Haugsdal, ., Triantafyllou, M. S., 2004. Effect of angle of attack profiles in flapping foil propulsion. Journal of Fluids and Structures 19, 37—47.

Hu, H., Kumar, A. G., Abate, G., Albertani, R., 2010. An experimental investigation on the aerodynamic performances of flexible membrane wings in flapping flight. Aerospace Science and Technology 14 (8), 575–586.

Huai-Te Yu, L. P. B., Morrison, C., 2012a. Experimental Investigation of Pitch Ramp-Hold-Return Motion of Flat Plates at Low Reynolds Number. 50th AIAA Aerospace Sciences Meeting including the New Horizons Forum and Aerospace Exposition 9 - 12 January 2012, Nashville, Tennessee.

Huai-Te Yu, L. P. B., Morrison, C., 2012b. Experimental Investigation of Pitch Ramp-Hold-Return Motion of Flat Plates at Low Reynolds Number. 50th AIAA Aerospace Sciences Meeting including the New Horizons Forum and Aerospace Exposition 9 - 12 January 2012, Nashville, Tennessee.

Huera-Huarte, F. J., Fernandez-Prats, R., 2015. Hydrodynamics of a rigid high aspect-ratio pitching foil in a uniform current. Submitted.

Huera-Huarte, F. J., Gharib, M., 2014. Flapping propulsion with tip pitch control. Bulletin of the American Physical Society, 59.

Huera-Huarte, F. J., Vernet, A., 2009. Vortex modes in the wake of an oscillating long flexible cylinder combining POD and fuzzy clustering. Experiments in Fluids 48 (6), 999–1013.

Ishihara, D., Horie, T., Denda, M., 2009. A two-dimensional computational study on the fluid-structure interaction cause of wing pitch changes in dipteran flapping flight. The Journal of experimental biology 212, 1–10.

Jones, K. D., Castro, B. M., Mahmoud, O., Pollard, S. J., Platzer, M. F., Neef, M. F., Gonet, K., Hummel, D., 2002. A collaborative numerical and experimental investigation of flapping-wing propulsion. AIAA Paper 2002-0706, 40th Aerospace Sciences Meeting & Exhibit.

Katz, J., 2006. Aerodynamics of race cars. Annual Review of Fluid Mechanics 38 (1), 27–63.

Katz, J., Weihs, D., 1978. Hydrodynamic propulsion by large amplitude oscillation of an airfoil with chordwise flexibility. Journal of Fluids Mechanics 88, 485–497.

Katz, J., Weihs, D., 1979. Large amplitude unsteady motion of a flexible slender propulsor. Journal of Fluids Mechanics 90, 713–723.

Katzmayr, R., 1922. Effect of Periodic Changes of Angle of Attack on Behavior of Airfoils. NACA TM-147.

Kemp, M., Hobson, B., C, P., 2003. Energetics of the Oscillating Fin Thruster. Unmanned Untethered Submersible Technology Symposium 2003.

Kim, D., Cossé, J., Huertas Cerdeira, C., Gharib, M., 2013. Flapping dynamics of an inverted flag. Journal of Fluid Mechanics 736, R1.

Kim, D., Gharib, M., 2011a. Characteristics of vortex formation and thrust performance in drag-based paddling propulsion. The Journal of experimental biology 214, 2283–91.

Kim, D., Gharib, M., 2011b. Flexibility effects on vortex formation of translating plates. Journal of Fluids Fluid Mechanic 677 (7), 255–271.

Knoller, R., 1909. Die Gesetze des Luftwiderstandes. Flug-und Motortechnik.

Kobayashi, S., Nakabayashi, M., Morikawa, H., 2006. Bioinspired Propulsion Mechanism in Fluid Using Fin with Dynamic Variable-Effective-Length Spring. Journal of Biomechanical Science and Engineering 1 (1), 280–289.

Koochesfahani, M., 1986. Wake of an oscillating airfoil. Phys. Fluids 29, 2776.

Koochesfahani, M., 1989. Vortical patterns in the wake of an oscillating foil. AIAA 27, 1200–1205.

Lai, J. C. S., Platzer, M. F., 1999. Jet Characteristics of a Plunging Airfoil. AIAA Journal, 1529–1537.

Lauder, G. V., Madden, P. G. A., Mittal, R., Dong, H., Bozkurttas, M., 2006. Locomotion with flexible propulsors: I. Experimental analysis of pectoral fin swimming in sunfish. Bioinspiration and Biomimetics 1, S25–S34.

Lewin, G. C., Haj-Hariri, H., 2003. Modelling thurst generation of a two-dimensional heaving airfoil in a viscous flow. Journal of Fluids Mechanics 492, 339–362.

Liao, J. C., Beal, D. N., Lauder, G. V., Triantafyllou, M. S., Nov. 2003. Fish exploiting vortices decrease muscle activity. Science (New York, N.Y.) 302 (5650), 1566–9.

Lighthill, J., 1975. Mathematical Biofluiddynamics. SIAM.

Lighthill, M. J., 1969. Hydromechanics of Aquatic Animal Propulsion. Annual Review of Fluid Mechanics 1, 413–446.

Lighthill, M. J., 1970. Aquatic animal propulsion of high hydromechanical efficiency. Journal of Fluid Mechanics 44, 265301.

Lindsey, C. C., 1978. Form, function, and locomotory habits in fish. Fish Physiology 7, 1–100.

Lissaman, P. B. S., 1983. Low-Reynolds-Number Airfoils. Annual Review of Fluid Mechanics 15, 223–239.

Liu, P., Bose, N., 1997. Propulsive performance from oscillating propulsors with spanwise flexibility. Journal of Fluids Mechanics 453, 1763–1770.

Maxworthy, T., 1981. The fluid dynamics of insect flight. Annual Review of Fluid Mechanics 13 (1), 329–350.

Miao, J. M., Ho, M. H., 2006. Effect of flexure on aerodynamic propulsive efficiency of flapping flexible airfoil. Journal of Fluids and Structures 22, 401–419.

Michelin, S., Llewellyn Smith, S. G., 2009. Resonance and propulsion performance of a heaving flexible wing. Physics of Fluids 21 (7), 071902.

Miller, L. a., Peskin, C. S., 2009. Flexible clap and fling in tiny insect flight. The Journal of experimental biology 212 (19), 3076–90.

Mirjany, M., Preuss, T., Faber, D. S., 2011. Role of the lateral line mechanosensory system in directionality of goldfish auditory evoked escape response. Journal of Experimental Biology 214 (20), 3358–3367.

Paraz, F., Eloy, C., Schouveiler, L., 2014. Experimental study of the response of a flexible plate to a harmonic forcing in a flow. Comptes Rendus Mécanique -, –.

Pederzani, J., H., H.-H., 2006. Numerical analysis of heaving flexible airfoils in a viscous flow. AIAA Journal 44, 2773–2782.

Prangemeier, T., Rival, D., Tropea, C., Feb. 2010. The manipulation of trailing-edge vortices for an airfoil in plunging motion. Journal of Fluids and Structures 26 (2), 193–204.

Prempraneerach, P., Hover, F. S., Triantafyllou, M. S., 2003. The effect of chordwise flexibility on the thrust and efficiency of a flapping foil. Proc. 13th Int. Symp. on Unmanned Untethered Submersible Technology: special session on bioengineering research related to autonomous underwater vehicles, New Hampshire.

Quinn, D. B., Moored, H. W., Dewey, P. A., J, S. A., 2014a. Unsteady propulsion near a solid boundary. Journal of Fluid Mechanics 742, 152–170.

Quinn, D. B., V, L. G., J, S. A., 2014b. Flexible propulsors in ground effect. Bioinspiration and Biomimetics 9, 036008.

Ramamurti, R., Lohner, R., Sandberg, W. C., 1999. Computation of the 3-D unsteady flow past deforming geometries. Int. Journal Computacional Fluids Dynamics 13, 83–99.

Ramananarivo, S., Godoy-Diana, R., Thiria, B., 2013. Passive elastic mechanism to mimic fish-muscle action in anguilliform swimming. Journal of the Royal Society Interface 10 (88), 20130667–20130667.

Raspa, V., Godoy-Diana, R., Thiria, B., 2013. Topology-induced effect in biomimetic propulsive wakes. Journal of Fluid Mechanics 729, 377–387.

Raspa, V., Ramananarivo, S., Thiria, B., Godoy-Diana, R., 2014. Vortex-induced drag and the role of aspect ratio in undulatory swimmersSubmitted to Phys. Fluids.

Rayner, J. M. V., 1991. On the Aerodynamics of Animal Flight in Ground Effect. Philosophical Transactions of the Royal Society B: Biological Sciences 334 (1269), 119–128.

Read, D. A., Hover, F. S., Triantafyllou, M. S., 2003. Forces on oscillating foils for propulsion and maneuvering. Journal of Fluids and Structures 17, 163—183.

Riggs, P., Bowyer, A., Vincent, J., Jun. 2010. Advantages of a Biomimetic Stiffness Profile in Pitching Flexible Fin Propulsion. Journal of Bionic Engineering 7 (2), 113–119.

Rosenberger, L. J., 2001. Pectoral fin locomotion in batoid fishes: undulation versus oscillation. Journal of Experimental Biology 204 (2), 379–394.

Schnipper, T., Andersen, A., Bohr, T., 2009. Vortex wakes of a flapping foil. Journal of Fluid Mechanics 633, 411.

Schouveilera, L., Hover, F. S., Triantafyllou, M. S., 2005. Performance of flapping foil propulsion. Journal of Fluids and Structures 20, 949–959.

Sfakiotakis, M., Lane, D. M., Davies, J. B. C., 1999. Review of Fish Swimming Modes for Aquatic Locomotion. IEEE Journal of Oceanic Engineering 24 (2), 237–252.

Shyy, W., Liu, H., Dec. 2007. Flapping Wings and Aerodynamic Lift: The Role of Leading-Edge Vortices. AIAA Journal 45 (12), 2817–2819.

Sirovich, L., 1987. Proper othogonal descomposition applied to turbulent flow in a square duct. Quart. Appl. Math. 45, 561–571.

Staufenbiel, R. W., Schlichting, U. J., 1988. Stability of airplanes in ground effect. Journal of Aircraft 25 (4), 289–294.

Tang, J., Viieru, D., Shyy, W., 2007. A Study of Aerodynamics of Low Reynolds Number Flexible Airfoils. 37th AIAA Fluid Dynamics Conference and Exhibit 25 - 28 June 2007, Miami, FL, 1–17.

Tanida, Y., 2001. Ground Effect in Flight. Birds, Fishes and High-Speed Vehicle. JSME International Journal Series B 44 (4), 481–486.

Taylor, G. K., Nudds, R. L., Thomas, A. L. R., 2003. Fluid and swimming animals cruise at a Strouhal number tuned for high power efficiency. Nature 425, 707–11.

Toomey, J., Eldredge, J. D., 2008. Numerical and experimental study of the fluid dynamics of a flapping wing with low order flexibility. Physics of Fluids 20 (7), 073603.

Triantafyllou, G., Triantafyllou, M., Grosenbaugh, 1993. Optimal Thrust Development in Oscillating Foils with Application to Fish Propulsion. Journal of Fluids and Structures 2 (7), 205–224.

Triantafyllou, M. S., Triantafyllou, G. S., Yue, D. K. P., 2000. Hydrodynamics of fishlike swimming. Annual Review of Fluid Mechanics 32 (1), 33–53.

Tuncer, I. H., Platzer, M. F., 1996. Thrust generation due to airfoil flapping. AIAA Journal, 324–331.

Vandenberghe, N., Zhang, J., Childress, S., May 2004. Symmetry breaking leads to forward flapping flight. Journal of Fluid Mechanics 506, 147–155.

Vanella, M., Fitzgerald, T., Preidikman, S., Balaras, E., Balachandran, B., 2009. Influence of flexibility on the aerodynamic performance of a hovering wing. The Journal of experimental biology 212, 95–105.

von Kármán, T., Burgers, J. M., 1935. Aerodynamic Theory: General Aerodynamic Theory. J. Springer.

Wang, Z. J., 2000. Vortex shedding and frequency selection in flapping flight. Journal of Fluid Mechanics 410, 323–341.

Webb, P. W., 1993. The effect of solid and porous channel walls on steady swimming of steelhead trout Oncorhynchus mykiss. Journal of Experimental Biology 178 (1), 97–108.

Webb, P. W., 2002. Kinematics of plaice, Pleuronectes platessa, and cod, Gadus morhua, swimming near the bottom. Journal of Experimental Biology 205 (1), 2125–2134.

Wen, L., Lauder, G., 2013. Understanding undulatory locomotion in fishes using an inertia-compensated flapping foil robotic device. Bioinspiration and Biomimetics 8, 046013.

Wilga, C. D., Lauder, G. V., 2004. Hydrodynamic function of the shark's tail. Nature 430, 850.

Willert, C., Gharib, M., 1991. Digital particle image velocimetry. Exp. Fluids 10, 181–193.

Williamson, C. H. K., Roshko, A., 1988. Vortex formation in the wake of an oscillating cylinder. Journal of Fluids and Structures 2, 355–381.

Withers, P. C., Timko, P. L., 1977. The significance of ground effect to the aerodynamic cost of flight and energetics of the black skimmer (Rhyncops nigra). Journal of Experimental Biology 70 (1), 13–26.

Wu, J. H., Sun, M., 2004. Unsteady aerodynamic forces of a flapping wing. Journal of Experimental Biology 207, n.7, 1137–1150.

Wu, T. Y., 1971a. Hydromechanics of swimming propulsion. Part 2. Some optimum shape problems. Journal of Fluid Mechanics 46, 521–544.

Wu, T. Y., 1971b. Hydromechanics of swimming propulsion. Part 2. Swimming of a two-dimensional flexible plate at variable forward speeds in an inviscid fluid. Journal of Fluid Mechanics 46, 337–355.

Yamamoto, I., rerada, Y., Nagamatu, T., Y, I., 1995. Propulsion System with Flexible/Rigid Oscillating Fin. IEEE Journal of Oceanic Engineering 20, 23–30.

Zhang, J., Liu, N.-S., Lu, X.-Y., 2010. Locomotion of a passively flapping flat plate. Journal of Fluids Mechanics 659, 43–68.

Zhao, L., Huang, Q., Deng, X., Sane, S. P., Zhao, L., Huang, Q., Deng, X., 2009a. Aerodynamic effects of flexibility in flapping wings Aerodynamic effects of flexibility in flapping wings. J. R. Soc. Interface (August), 1–13.

Zhao, L., Huang, Q., X, D., P, S. S., 2009b. Aerodynamic effects of flexibility in flapping wings. Journal of The Royal Society Interface 7, 485–497.